AD-783 359

ANALYSIS OF THERMAL STRESSES IN CORED CERAMIC BRICKS USED IN HYPERSONIC WIND TUNNEL HEATERS

F. C. Weiler, et al

Acurex Corporation

Prepared for:

Air Force Materials Laboratory

October 1972

DISTRIBUTED BY:

NTIS

National Technical Information Service
U. S. DEPARTMENT OF COMMERCE
5285 Port Royal Road, Springfield Va. 22151

UNCLASSIFIED
Security Classification

AD 783359

DOCUMENT CONTROL DATA - R & D

Security classification of title, body of abstract and indexing annotation must be entered when the overall report is classified)

1. ORIGINATING ACTIVITY (Corporate author)
Aerotherm Division/Acurex Corporation
485 Clyde Aveune
Mountain View, California 94040

2a. REPORT SECURITY CLASSIFICATION
UNCLASSIFIED

2b. GROUP
-

3. REPORT TITLE
ANALYSIS OF THERMAL STRESSES IN CORED CERAMIC BRICKS USED IN HYPERSONIC WIND TUNNEL HEATERS

4. DESCRIPTIVE NOTES (Type of report and inclusive dates)
Final Report (April 1971 to October 1972)

5. AUTHOR(S) (First name, middle initial, last name)
F. C. Weiler
T. C. Derbidge
C. A. Powars

6. REPORT DATE
October 1972

7a. TOTAL NO. OF PAGES
96

7b. NO. OF REFS
18

8a. CONTRACT OR GRANT NO.
F33615-71-C-1559

b. PROJECT NO.
7381

9a. ORIGINATOR'S REPORT NUMBER(S)
AFML-TR-72-248

9b. OTHER REPORT NO(S) (Any other numbers that may be assigned this report)
Aerotherm Final Report 72-61

10. DISTRIBUTION STATEMENT
Approved for public release; distribution unlimited.

11. SUPPLEMENTARY NOTES
-

12. SPONSORING MILITARY ACTIVITY
Systems Support Division
Air Force Materials Laboratory
Wright Patterson A. F. B., Ohio

13. ABSTRACT
The thermostructural response of cored ceramic bricks used in hypersonic wind tunnel heaters was analyzed. The objective was to gain an understanding of the mechanisms which can cause brick fractures. The analyses were carried out by computing (1) the gross heater thermal response which furnished boundary conditions for computation of (2) the detailed temperature distribution in a brick segment which was input to compute (3) the stresses and strains in the brick segment. State-of-the-art numerical analytical techniques were applied in each step. Yttria stabilized zirconia and alumina bricks were considered. It was found that brick "web stresses" (caused by temperature gradients normal to the hole surface during heater blowdown) alone are not severe enough to cause fractures. Nonlinear temperature gradients across the whole bricks can cause significant "body stresses", and these were analyzed in a parametric fashion. The effects of point contacts between bricks and other stress affecting phenomena were also considered. Superposition was applied to define typical combinations of thermal and mechanical loadings which could cause brick stresses equal to the estimated brick ultimate strength.

109

DD FORM 1 NOV 65 1473 REPLACES DD FORM 1473, 1 JAN 64 WHICH IS OBSOLETE FOR ARMY USE

UNCLASSIFIED
Security Classification

UNCLASSIFIED
Security Classification

14 KEY WORDS	LINK A ROLE	LINK A WT	LINK B ROLE	LINK B WT	LINK C ROLE	LINK C WT
Thermal Stress						
Ceramics						
Heaters						
Heat Exchangers						
Hypersonic Wind Tunnel						
Transient Heat Conduction						
Finite-Element Method						

UNCLASSIFIED
Security Classification

ANALYSIS OF THERMAL STRESSES IN CORED CERAMIC BRICKS USED IN HYPERSONIC WIND TUNNEL HEATERS

F. C. Weiler
Weiler Research Incorporated

T. C. Derbidge
C. A. Powars
Aerotherm Division/Acurex Corporation

Approved for public release; distribution unlimited.

FOREWORD

This report documents work performed at Acurex Corporation, Aerotherm Division, Mountain View, California for the Air Force Materials Laboratory, Air Force Systems Command, Wright Patterson Air Force Base, Ohio under Contract F33615-71-C-1559. The technical monitor was Capt J. R. Koenig AFML/MXS who was assisted by Major L. Fahrenbacher of Aeronautical Research Laboratory, both of whom gave technical assistance throughout the course of this work.

The Aerotherm project manager was C. A. Powars. The thermal evaluations were performed by T. C. Derbidge who was assisted by C. A. Powars and C. B. Moyer, all of Aerotherm Division of Acurex Corporation. The stress evaluations were performed by F. C. Weiler, of Weiler Research, Inc. who was formerly with Aerotherm.

This technical report has been reviewed and is approved.

James D Gerber

JAMES D. GERBER, CAPT USAF
Chief, Space & Missiles Branch
Systems Support Division
AF Materials Laboratory

ABSTRACT

The thermostructural response of cored ceramic bricks used in hypersonic wind tunnel heaters was analyzed. The objective was to gain an understanding of the mechanisms which can cause brick fractures. The analyses were carried out by computing (1) the gross heater thermal response which furnished boundary conditions for computation of (2) the detailed temperature distribution in a brick segment which was input to compute (3) the stresses and strains in the brick segment. State-of-the-art numerical analytical techniques were applied in each step. Yttria stabilized zirconia and alumina bricks were considered. It was found that brick "web stresses" (caused by temperature gradients normal to the hole surface during heater blowdown) alone are not severe enough to cause fractures. Nonlinear temperature gradients across the whole bricks can cause significant "body stresses", and these were analyzed in a parametric fashion. The effects of point contacts between bricks and other stress affecting phenomena were also considered. Superposition was applied to define typical combinations of thermal and mechanical loadings which could cause brick stresses equal to the estimated brick ultimate strength.

TABLE OF CONTENTS

Section		Page
1	INTRODUCTION	
2	HEATER AND BRICK THERMAL RESPONSE	5
	2.1 Analytical Techniques	5
	2.1.1 Gross Heater Thermal Response	6
	2.1.1.1 System Energy Balance	8
	2.1.1.2 TACH Check Solutions	12
	2.1.2 Brick Segment Two-Dimensional Transient Response	15
	2.2 Material Thermal Properties	16
	2.2.1 Yttria Stabilized Zirconia Thermal Properties	16
	2.2.2 Alumina Thermal Properties	16
	2.3 Typical Results of Thermal Analyses	20
3	HEATER BRICK STRUCTURAL RESPONSE	24
	3.1 Material Mechanical Properties	24
	3.2 Finite Element Thermal Stress Analysis Code	27
	3.3 Brick Stress Analyses	28
	3.3.1 Web Stress Analyses	29
	3.3.2 Nonlinear Temperature Gradients Across Bricks	40
	3.3.3 Point Contact Loading Stress Analysis	49
	3.3.4 Combined Effect of Different Loadings	53
	3.3.5 Other Stress-Affecting Phenomena	60
4	CONCLUSIONS	62
	REFERENCES	64
	APPENDIX A - Implicit One-Dimensional Finite Difference Conduction Solution	65
	APPENDIX B - Effects of Hole Misalignments in Wind Tunnel Heater Core Bricks on Pressure Drop and Heat Transfer	73
	APPENDIX C - Limitations Due to Combined Stress Effects and Fracture Criteria Uncertainties	92

Preceding page blank

LIST OF FIGURES

Figure		Page
1	Cross Section of Typical Cored Ceramic Brick Considered in Analysis W = 2.78 in.	3
2	Geometry of the Hole Spacing in Cored Heater Bricks	7
3	Schematic of Numerical Element Resulting from Lumped Parameter Approach and One-Dimensional Conduction Assumption	9
4	Comparison of TACH Wall Temperature Calculations with Exact Solution of Hausen	13
5	Comparison of TACH Gas Temperature Calculations with Exact Solution of Hausen	14
6	Basic Symmetry Element of Cored Brick Ceramic Heater	17
7	Thermal Grid for Symmetry Element Used for Web Stress Analysis	18
8	Gas Temperature History Predicted by TACH for the Nominal Heater Conditions (3,000 psi, 1150 lbm/sec, S/D = 1.475, Sinusoidal Initial Temperature Distribution)	21
9	Wall Temperature History Predicted by TACH for the Nominal Heater Conditions (3,000 psi, 1150 lbm/sec, S/D = 1.475, Sinusoidal Initial Temperature Distribution	22
10	Machine Isotherm Plot Illustrating Typical Output of the ASTHMA Detailed Response Calculations	23
11	Mechanical Properties of Fully Cubic Yttria Stabilized Zicronia (YSZ) Used in Analysis	
	A) Elastic Modulus, E and Yield Stress, Y	25
	B) Coefficient of Thermal Expansion, $\alpha = \varepsilon^{th}/(T - T_o)$	26
12	Mechanical Boundary Conditions of Typical Symmetrical Section	31
13	Results of Web Stress Analysis "Case I" Conditions (Plane Stress, σ_z =-28.9 psi) Nominal Blowdown Conditions, Time = 10 sec S/D = 1.475 A) through F)	33 - 35
14	Results of Web Stress Analysis "Case III" Conditions (Plane Strain, ε_z = 0) Nominal Blowdown Conditions, Time = 10 sec, S/D = 1.475 A) through E)	37 - 39
15	Boundary Conditions of Equivalent Cylinder Model	42
16	Hypothetical Nonlinear Temperature Gradients	43
17	Locations of Maximum Tensile Stress in Equivalent Cylinder Brick Model	46

LIST OF FIGURES (Concluded)

Figure		Page
18	Stress β-Factors Versus Length of Bricks	48
19	Illustration of Column of Bricks with Point Contact Load	50
20	Results of Brick Point Contact Stress Analysis A) through F)	51 - 52
21	Biaxial Fracture Surface Used as Failure Criteria for YSZ Bricks	56
22	Interaction Curve for Fracture Stress Condition in 4 in. YSZ Brick at T = 2872°F	59
B-1	Dimensionless Head Loss (K) for Turbulent Flow Through Sudden Expansions and Contractions	78
B-2	Comparison of Bed Thermal Response for 0% ($\dot{m}$ = .0144 lbm/sec-Hole) & 14% ($\dot{m}$ = .0122 lbm/sec-Hole) Misalignment - Neglecting Cross-Conduction	85
B-3	Comparison of Bed Thermal Response for 0% ($\dot{m}$ = .0144 lbm/sec-Hole) & 30% ($\dot{m}$ = .0086 lbm/sec-Hole) Misalignment - Neglecting Cross-Conduction	86
B-4	Estimated Maximum Temperature Difference Between 0 & 14% Misalignment and 0 & 30% Misalignment for Heater ΔP = 4.8 psi Neglecting Cross-Conduction	88
C-1	3-Dimensional Finite Element Model of Hexagonal Brick	93
C-2	Coulomb-Mohr Failure Criterion for Elastic-Brittle Materials	95

LIST OF TABLES

Table		Page
1	Thermal Properties of Yttria Stabilized Zirconia Used in Computations	19
2	Thermal Properties of Polycrystalline α - Alumina Used in Calculations	19
3	Yttria Stabilized Zirconia Material Properties	27
4	Maximum Stress Results of In-Plane Analyses	40
6	ΔT (RADIAL) β-Factors	44
5	Stresses Associated with Nonlinear Radial and Axial Temperature Gradients	45
7	ΔT (AXIAL) β-factors	
B-1	Wind Tunnel Heater Conditions Considered	74
B-2	Axial Pressure Drop Across Heater Bed, 14% Misalignment	80
B-3	Axial Pressure Drop Across Heater Bed, 30% Misalignment	81

LIST OF SYMBOLS

a	radius of equivalent cylinder for the entire hexagonal brick
A	cross-sectional area
A_{surf}	area of heat transfer surface
C	specific heat capacity of the solid
c_p	specific heat capacity of the gas
D	diameter of holes in brick
E	elastic modulus
G	shear modulus
h	convective heat transfer coefficient (Section 2)
h	cylinder height (Section 3)
H	enthalpy of gas
k	thermal conductivity of solid (Section 2)
k	shear yield stress (Section 3)
k_g	thermal conductivity of gas
$\dot{m}$	mass flow rate of gas
M	mass per unit heater core length
p	reacting pressure within the heater core material
P	wetted perimeter (Section 2)
p	gas pressure (Section 3)
Pr	Prandtl number of gas
$\dot{q}$	heat flux rate
$\dot{q}_{conv}$	convected heat flux rate
$\dot{Q}$	net heat rate
r	cylinder radial coordinate
R_{eff}	radius of equivalent cylinder for the adiabatic hexagon
Re_D	Reynolds number based on hole diameter

LIST OF SYMBOLS (Continued)

S	distance between holes
T	temperature
T_D	gas driving temperature for heat transfer calculation
T_o	reference temperature $T_o = 70°F$
T_{mean}	weighted mean temperature
ΔT	increment of temperature
u	average gas velocity
W	distance across flats of hexagonal cored brick
Y	yield stress
z or Z	axial distance measured from the bottom of the heater bed
α	constant in conduction equation (6) (Section 2)
α	coefficient linear thermal expansion (Section 3)
β	constant in conduction equation (6) (Section 2)
β	numerical stress factor (Section 3)
ε	strain
η	non-dimensional time $\eta = \frac{hP}{CM}\theta$ (Section 2)
θ	time (Section 2)
θ	cylinder circumferential coordinate (Section 3)
μ	viscosity of gas
ν	Poisson's ratio
ξ	non-dimensional length $\xi = \frac{hP}{c_p\dot{m}} z$
ρ	density of gas
σ	direct stress
τ	shear stress
Υ	temperature difference $\Upsilon = T_{wall} - T_{entering\ gas}$

LIST OF SYMBOLS (Concluded)

SUBSCRIPTS

BASE	at the base of the equivalent cylinder
B or BOTTOM	at the bottom of the equivalent cylinder
i	denotes initial conditions
in	denotes gas conditions at the inlet of the numerical element
max	maximum condition
out	denotes gas conditions at the outlet of the numerical element
r	denotes radial coordinate direction
T or TOP	at the top of the equivalent cylinder
Ult.	ultimate condition
w or wall	adjacent to the heated surface
x, y, z	denotes cartesion coordinate directions
θ	denotes circumferential coordinate direction

SUPERSCRIPTS

E	pertains to the center of the ends of the equivalent brick cylinder
S	pertains to midway along the outside of the equivalent brick cylinder
th	pertains to thermal strain data
*	maximum condition

SECTION 1

INTRODUCTION

Blowdown type hypersonic wind tunnels utilize storage heaters to increase the total energy content of the air used as the test fluid. The maximum operating total temperature capability is usually limited by the high temperature integrity of the heater matrix material. For this reason, refractory ceramics (e.g., alumina, magnesia, zirconia) are usually employed.

A performance requirement for hypersonic tunnels is minimum test stream contamination. The primary source of contamination is "dust" resulting from fractures of the heater core matrix material. Thus, the requirement to maintain heater matrix thermal stresses safely below ultimate strengths results in major performance and design constraints on the wind tunnel facility (e.g., Ref. 1).

Most existing hypersonic wind tunnel storage heater ceramic matrices are of the "pebble bed" type. The desire to eliminate the high stresses associated with the point contact of stacked spheres has led to the identification of cored bricks as the optimum matrix configuration for large capacity storage heaters (Refs. 1, 2). Cored bricks are also advantageous in that they enable a lower heater pressure drop for a given heat transfer area density.

Unfortunately, the thermostructural behavior of cored bricks in wind tunnel heaters is quite complex and hence poorly understood. However, a quantitative understanding of the thermostructual response of the heater matrix is necessary to enable rational heater design and operating envelope definition. Cored brick thermal stress calculations performed to date have been quite approximate; usually involving gross assumptions to enable the application of closed-form solutions or handbook formulas. The lack of understanding of the thermostructural response of cored bricks is evidenced by the fracture of bricks used in pilot heater applications, although it should be stated that major uncertainties are associated with factors such as zirconia destabilization (see, e.g., Ref. 3).

The objective of this study was to apply state-of-the-art numerical analytical techniques to analyze the thermostructural state of cored bricks used in hypersonic wind tunnel heaters. The analytical techniques included multidimensional numerical transient heat transfer analysis codes and finite-element

structural analysis codes previously developed primarily for application to reentry vehicle heat shields and nose tips. It was felt that understanding of the thermostructural response of cored brick heater matrices could be advanced through the application of these sophisticated analytical techniques.

A typical configuration was selected to serve as a basis for the brick response calculations. Initially, the analyses were to be performed for conditions corresponding to a pilot heater for the TTT (True Temperature Tunnel) facility once planned for installation at AEDC. However, the construction of this facility remained uncertain and so conditions corresponding to a cored brick heater planned for the AEDC APTU (Airbreathing Propulsion Test Unit) facility were selected as a basis for analysis.

The cored bricks are of hexagonal cross-section measuring about 2.78 inches across the flats as sketched in Figure 1. The bricks contain 91 holes of nominal 0.2 inch diameter. This results in a hole spacing to diameter ratio (S/D) of 1.47. Variations on this nominal hole configuration were of interest, and so S/D = 1.3 and 1.8 were also considered. The heater bed is 86 inches in diameter by 24 feet high. The matrix consists of yttria stabilized zirconia (YSZ) bricks from the top down to 12 feet (middle of the bed) and alumina bricks from the 12 foot level down to the bottom.

The nominal operating condition considered was 3000 psi, 1150 lbs/sec flow rate, with a bed initial temperature distribution of sinusoidal shape given by

$$T(z) = T_m - \frac{1}{2}\left(T_m - T_o\right)\left\{1 - \cos\left[\frac{\pi}{L}(24 - z)\right]\right\}$$

where

$$T_o = 500°R$$

$$T_m = 4500°R$$

$$L = 36 \text{ ft}$$

z = the distance from the bottom of the heater bed in feet

Since the bed is 24 feet high, the initial bed temperature is 4500°R at the top and 1500°R at the bottom. The locations in the matrix of primary interest are the top of the bed (YSZ bricks), middle of the bed (YSZ - alumina interface), and the bottom of the bed (alumina bricks).

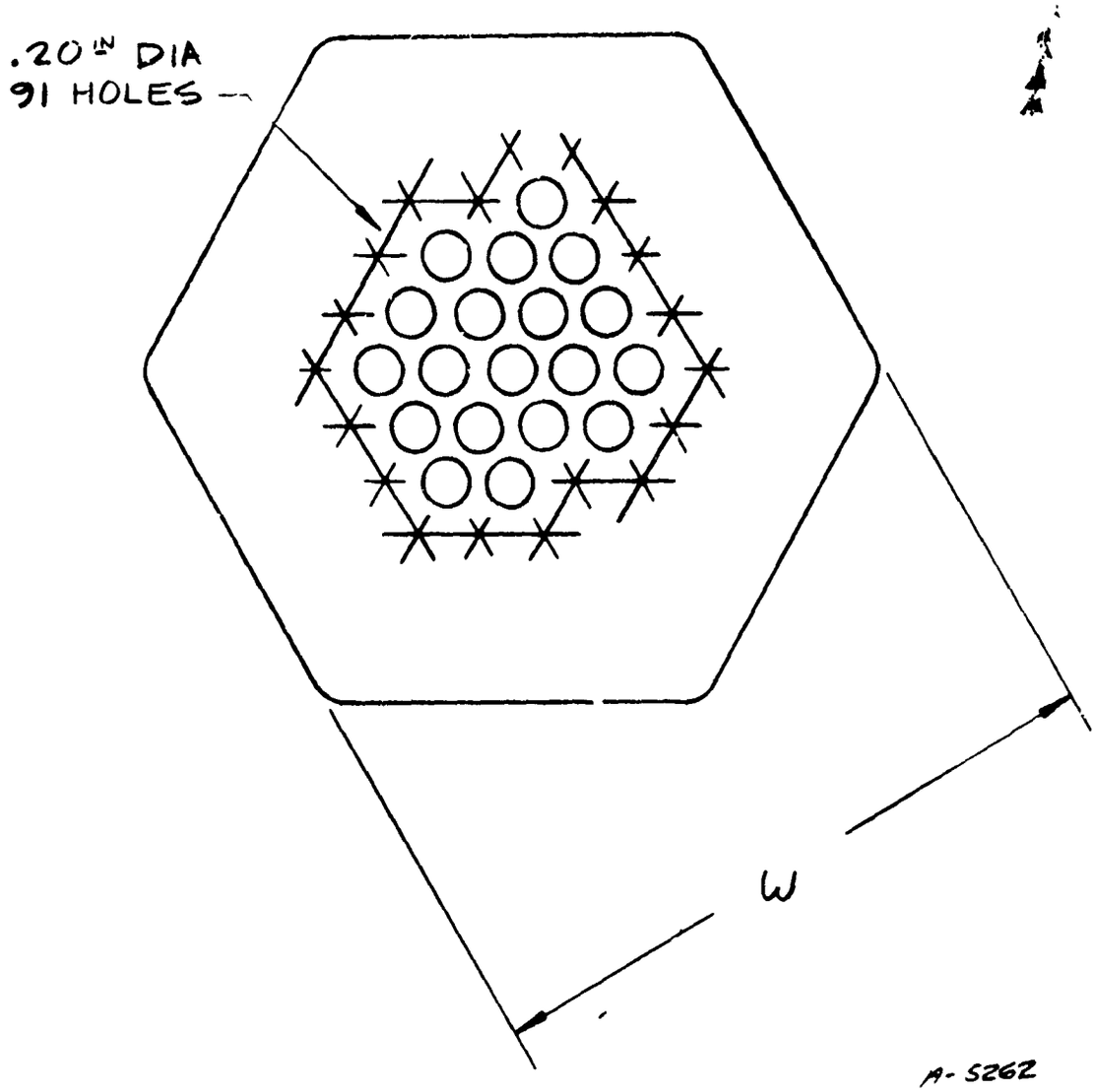

FIGURE 1 CROSS SECTION OF TYPICAL CORED CERAMIC BRICK CONSIDERED IN ANALYSIS
W = 2.78 IN

During tunnel operation ("blowdown"), high pressure air enters the heater from the bottom, is heated as it passes up through the matrix holes, and exhausts from the top and continues on to the test section. As the air passes through the brick holes, heat is transferred from the brick to the air. This gives rise to sharp temperature gradients in the brick webs between the holes, the hole surface temperature being lower than the web center temperature. These temperature gradients cause thermal stresses in the brick webs.

It was initially suspected that these "web stresses" were the most critical stresses in the brick, and so major emphasis was to be given to their characterization for a variety of conditions. However, as will be discussed in detail subsequently, initial calculations demonstrated that the web stresses alone were very much lower than what was believed to be the material strength. Also, observation of fractured bricks from a pilot heater and discussions with parties with field experience with cored ceramic bricks indicated that brick thermal stresses arise from a variety of factors in addition to web stresses. Rather than limit consideration to web stresses, it was decided to perform calculations to investigate some of these other stress effects.

The various effects which may give rise to brick stresses may be analyzed with various degrees of precision. Some effects are not particularly amenable to analysis because the associated boundary or initial conditions are not known (e.g., temperature gradients across the whole brick and residual stresses), and so these were analyzed in a parametric fashion.

The heater and brick thermal analyses are discussed, and some typical results are presented, in Section 2. These analyses provided temperature distributions which were input to the stress analyses. The brick structural analyses are discussed in Section 3. A variety of potential failure modes are discussed and quantitatively characterized. Conclusions are drawn and recommendations are made in Section 4. Certain analytical details are included as appendices. Appendix A presents some mathematical details relative to the heat conduction solution aspect of the gross heater thermal response analysis. Appendix B documents an analysis of the potential effects on the heater thermal response of misalignments of the holes between adjacent bricks. Appendix C discusses some limitations on brick stress and fracture conclusions due to combined stress effects and fracture criteria uncertainties.

SECTION 2

HEATER AND BRICK THERMAL RESPONSE

An accurate detailed thermal history of a given region within the heater core must be supplied as input to any thermostructural analysis. In order to assure the validity of this thermal analysis, the mathematics employed should model as well as possible the following conditions encountered in engineering applications:

1. Heater beds composed of multiple materials with "real" properties; i.e., materials whose conductivities are finite and whose properties are temperature dependent
2. Variation in heat transfer coefficient with air temperature and velocity
3. Initial axial temperature distributions of practical significance.

Numerical analysis techniques were chosen over closed form solutions for the following reasons:

- Closed form solutions do not adequately model practical applications because they require the assumption of a single matrix material with constant thermal properties (with infinite conductivity in the radial direction and zero conductivity in the axial direction), constant heat transfer coefficient, and uniform initial temperature distribution
- The basic computation schemes and in some cases computer codes already existed
- Numerical schemes are easy to interface with numerical stress calculations.

The basis of the numerical techniques used are covered in Section 2.1, the thermal properties of the materials analyzed are given in Section 2.2, and typical results of the thermal analyses are presented in Section 2.3.

2.1 ANALYTICAL TECHNIQUES

Structural analysis of a given heater region requires an accurate and highly detailed in-depth thermal history of that region. Numerical thermal analysis of the entire heater core on the detail scale necessary for subsequent thermostructural analysis is prohibitively expensive when considered in light of the fact that detailed thermal histories are not required for the entire bed but only at selected regions in the bed where it is desired to calculate the

thermostructural response. Furthermore, the overall thermal response of the heater may be adequately calculated without determining the detailed in-depth response of the bed.

In view of these considerations it was decided to divide the thermal analysis into two parts: the first being a gross heater thermal response analysis to determine the hole surface boundary conditions for the second detailed analysis of a given heater brick segment.

The gross thermal analysis is presented in Section 2.1.1 and the detailed two-dimensional transient response is discussed in Section 2.1.2.

2.1.1 Gross Heater Thermal Response

The objective of the gross heater thermal response calculations is to determine the transient heat transfer conditions (heat transfer coefficient and gas enthalpy) existing throughout the heater bed at various times during the blowdown. A modification of the PANDA (Ref. 4) one-dimensional conduction computer code was utilized for these calculations. The modified computer code is referred to as the TACH (Thermal Analysis of Ceramic Heaters) code and the modified in-depth conduction solution is discussed in detail in Appendix A.

To economically accomplish the objectives of the overall heater analysis the simplifying assumptions are made that there is no axial heat flow in either the bed material or the flowing air. The former assumption is justified on the basis of the relatively low thermal conductivity of almost all ceramic materials and the fact that, for heater geometries of interest, the radial temperature gradients are an order of magnitude greater than the axial gradients. The assumption that axial conduction within the air is negligibly small is quite good considering the relative energy transfer due to bulk fluid movement.

Figure 2 shows an overhead view of the holes in a typical heater brick. Also shown are the lines of symmetry between the holes; no heat flows across these lines of symmetry if heat transfer conditions are constant from one hole to the next. This latter assumption implies that flow conditions are the same in all holes at any given axial location* and that losses at the edge of the bed are negligible.

Notice that symmetry considerations effectively divide the bed into a series of nested, adiabatic, hexagonal cylinders. The conduction heat transfer

*Significant hole-to-hole flow variations can result from misalignment of the holes in adjacent bricks, and this can give rise to net temperature gradients across the bricks. An approximate analysis of this circumstance was carried out and is presented as Appendix B to this report.

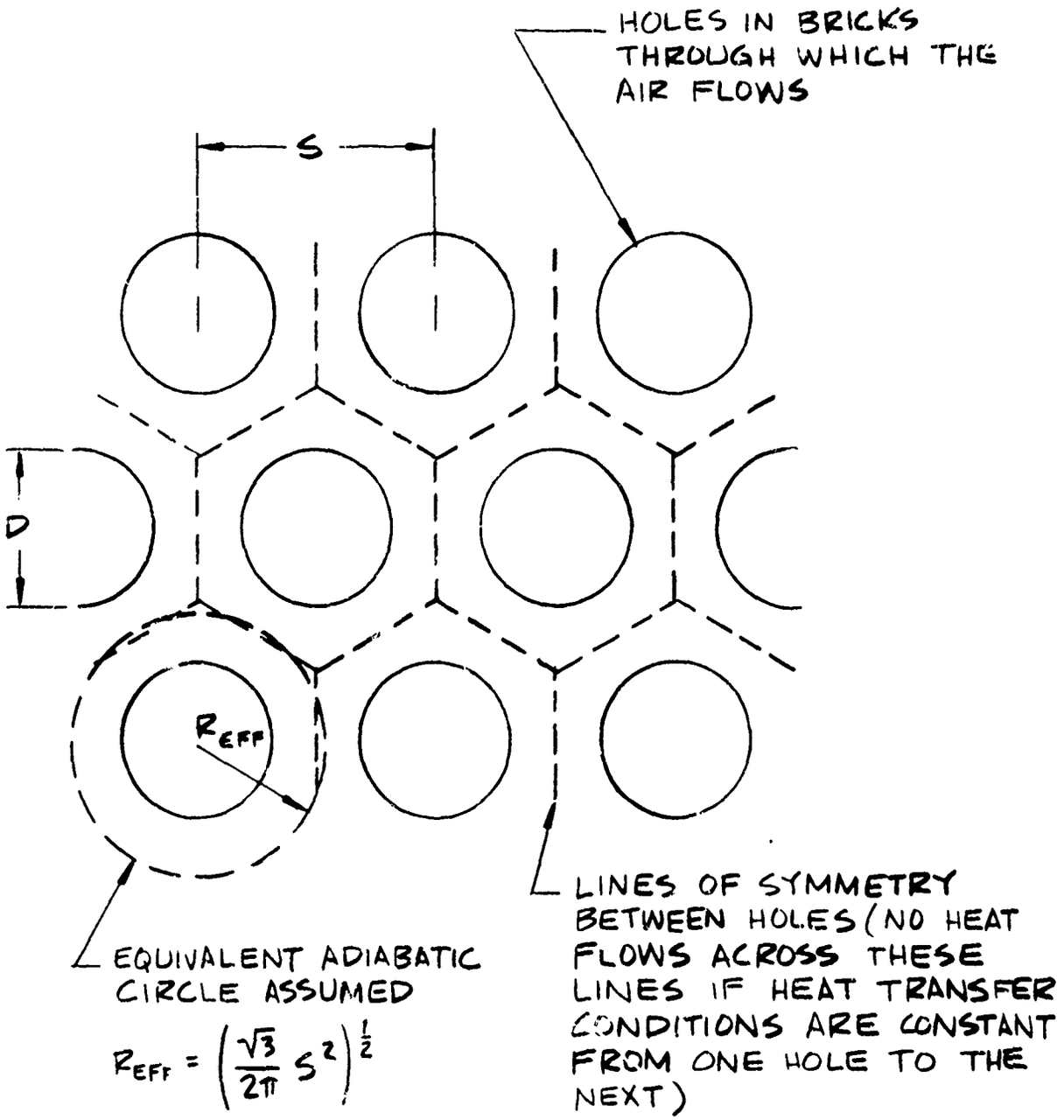

FIGURE 2 GEOMETRY OF THE HOLE SPACING IN CORED HEATER BRICKS

A-5249

within these adiabatic hexagons is two-dimensional in nature and as was previously discussed, need not be completely modeled for the gross heater thermal analysis. Therefore in order to reduce the problem to a one-dimensional conduction situation, while still conserving heat storage capacity, an effective adiabatic circle is assumed whose area is equal to that of the adiabatic hexagon (see Figure 2). The radius of this circle is given by

$$R_{eff} = \left(\frac{\sqrt{3}}{2\pi} S^2 \right)^{1/2} = .525\ S \tag{1}$$

This approach has the advantage that net energy is still conserved while reducing computation time by at least two orders of magnitude.

Utilizing the lumped parameter approach the bed is divided, for numerical analysis, into a number of isothermal axial stations of length ΔZ. Thus the temperature at any radial location is assumed constant over the length of the axial station (ΔZ). Figure 3 depicts the essentials to be considered for the defined lumped parameter numerical element.

The overall solution procedure followed in predicting the transient thermal response of a numerical element is as follows:

a. A suitably small time step is determined (as described in Appendix A), over the span of this time step all rates, material properties, and boundary conditions are assumed constant.

b. A system energy balance is performed for the assumed constant rates and boundary conditions.

c. New material properties and boundary conditions are determined and the first step is then repeated, etc.

The system energy balance is discussed in Section 2.1.1.1, and check solutions are shown in Section 2.1.1.2.

2.1.1.1 System Energy Balance

Three energy conservation equations may be written for the numerical element of Figure 3; they are

1. A net energy balance on the flowing air
2. A surface energy transfer rate balance on the shell/air interface
3. An in-depth energy balance on the cylindrical shell.

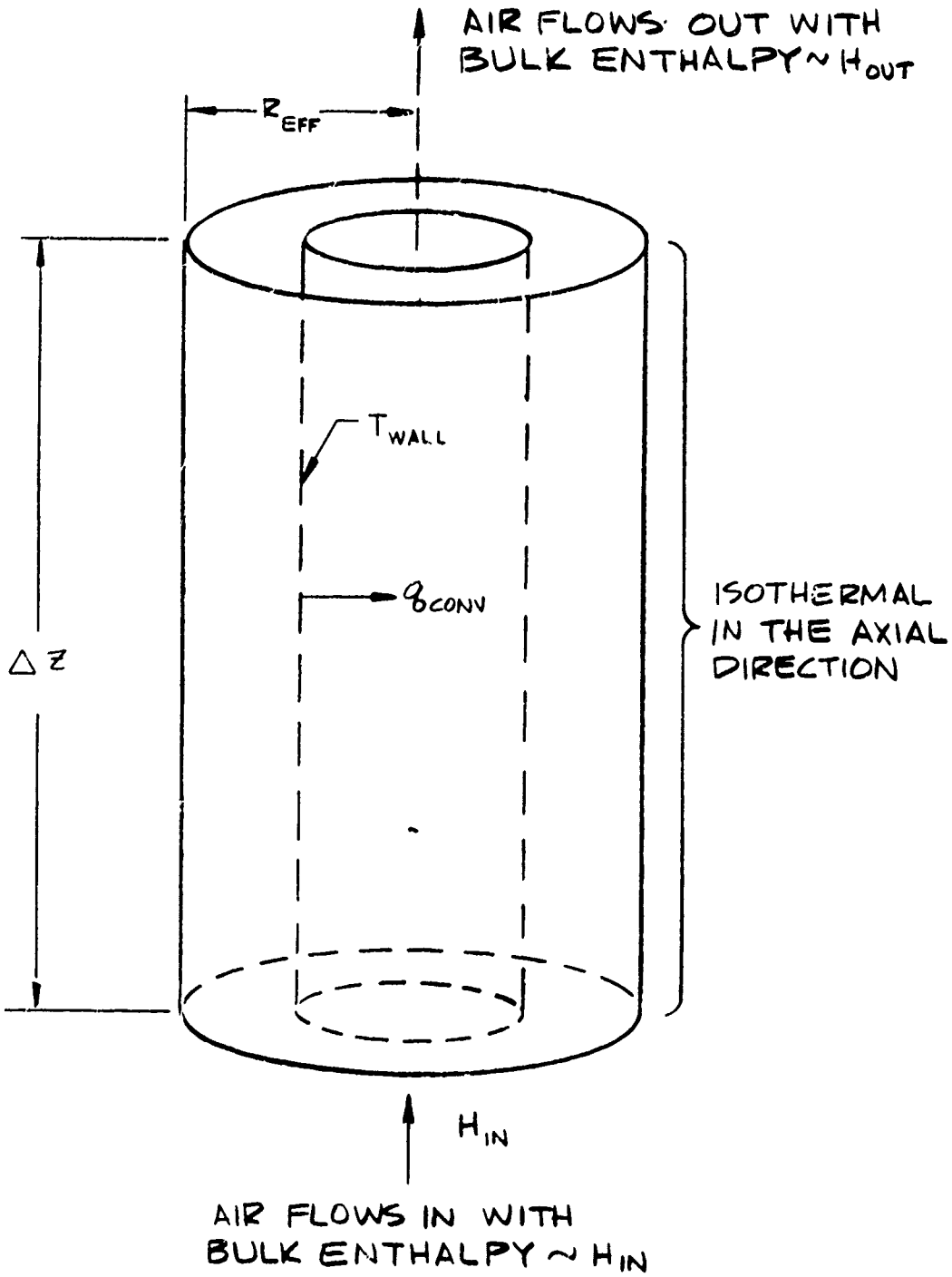

FIGURE 3 SCHEMATIC OF NUMERICAL ELEMENT RESULTING FROM LUMPED PARAMETER APPROACH AND ONE-DIMENSIONAL CONDUCTION ASSUMPTION

A-5250

The net rate at which energy is entering the air flowing over the axial station is

$$\dot{Q} = \dot{m}(H_{out} - H_{in}) \tag{2}$$

where

$\dot{m}$ = air mass flow rate

H_{in} = bulk enthalpy of incoming air

H_{out} = bulk enthalpy of outgoing air

For the first axial station the enthalpy of the incoming air (H_{in}) is a constant equal to the supply air enthalpy and for all subsequent down stream stations H_{in}, as a function of time, is known from the transient solution at the previous station.

The enthalpy of air as a function of temperature is input tabularly to account for temperature variations in specific heat capacity.

The flux of energy between the flowing air and the solid heater is given by

$$\dot{q} = h(T_w - T_D) \tag{3}$$

where

h = the local heat transfer coefficient

T_w = the solid wall temperature

T_D = the gas "driving" temperature

For purposes of calculation the gas driving temperature (T_D) is set equal to the average of the incoming and outgoing bulk gas temperature

$$T_D = \frac{T_{in} + T_{out}}{2} \tag{4}$$

The local heat transfer coefficient (h) is calculated by the method recommended by Colburn as presented in Reference 5:

$$h = .0231 \left(\frac{k_g}{D}\right) Re_D^{.8} \; Pr^{1/3} \tag{5}$$

where

k_g = thermal conductivity of the fluid

D = hole diameter

$Re_D = \frac{\rho u D}{\mu}$ = Reynolds number based on hole diameter

Pr = Prandtl number of the fluid

Equation 5 represents a correlation for fully turbulent (i.e. $Re_D > 10{,}000$) and fully developed (i.e. $Z > 50\ D$) pipe flow. The Reynolds numbers of interest here are typically greater than 25,000 and $Z = 50\ D$ occurs at approximately 10 inches from the bed inlet, and thus both conditions are well satisfied. During the course of calculation the heat transfer coefficient is constantly re-calculated (at the conditions existing during the previous time step) to account for fluid property variation with temperature. This latter variation can amount to over a 50% change in heat transfer coefficient over the length of the bed.

The in-depth energy balance on the cylindrical shell of heater brick material is accomplished by a fully implicit finite difference approach which is described in detail in Appendix A. Using this fully implicit method the energy flux conducted <u>from</u> the surface is given by

$$-\dot{q} = \alpha + \beta T_w \tag{6}$$

where α and β are defined in Appendix A. The constants α and β result from a first pass Gauss reduction of the implicit finite difference tri-diagonal conduction matrix, and are functions of the material properties and the in-depth temperature profile of the previous time step.

Combining the surface energy balance with the results of the in-depth energy balance (Equations (3) and (6)) the following is obtained:

$$\dot{q} = h\left(\frac{-\alpha - \beta T_D}{h + \beta}\right) = \text{function } (T_D) \tag{7}$$

Note that the net heat rate to the flowing air must be equal to the surface heat flux times the surface area or

$$\dot{Q} = \dot{q}\ A_{surf} \tag{8}$$

The system energy balance is accomplished iteratively as follows:

1. Guess T_D
2. Calculate $\dot{q}$ from the combined in-depth and surface energy balances, Equation (7)
3. Calculate the net heat rate from $\dot{Q} = \dot{q}\ A_{surf}$
4. Calculate H_{out} from the net energy balance, Equation (2), knowing H_{in}
5. Look up T_{in} and T_{out} from H_{in} and H_{out} in the enthalpy temperature table.
6. Calculate a new T_D from

$$T_D = \frac{T_{in} + T_{out}}{2}$$

7. If the new T_D is within an allowable error of the old T_D (say $\pm$ 5 deg Rankin) go to the next time step; if not return to step 1. with the new T_D as a new guess.

Using this method the transient thermal response of each axial station in the heater bed is calculated.

2.1.1.2 TACH Check Solutions

Following its development phase TACH was run on a battery of test cases to determine:

1. Reliability of its one-dimensional conduction solution
2. Agreement of numerical solution with a closed-form solution for simple conditions
3. Optimal nodal spacing and time step size.

The one-dimensional conduction solution of TACH was checked by inputting constant material properties and running for one axial station only. The output was then compared with an analytical solution from the Schneider charts (Ref. 6). Good agreement was obtained (less than 1% error).

TACH performance on the total bed was compared with Hausen's analytical solution (Ref. 7) which assumes infinite conduction normal to the flow, constant material and gas properties, and uniform initial axial temperature distribution. The results of this comparison are shown in Figures 4 and 5. Figure 4 presents comparisons of non-dimensional wall temperature ratios (T_w/T_{wi}) versus non-dimensional distance (ξ) at various normalized times (η) where

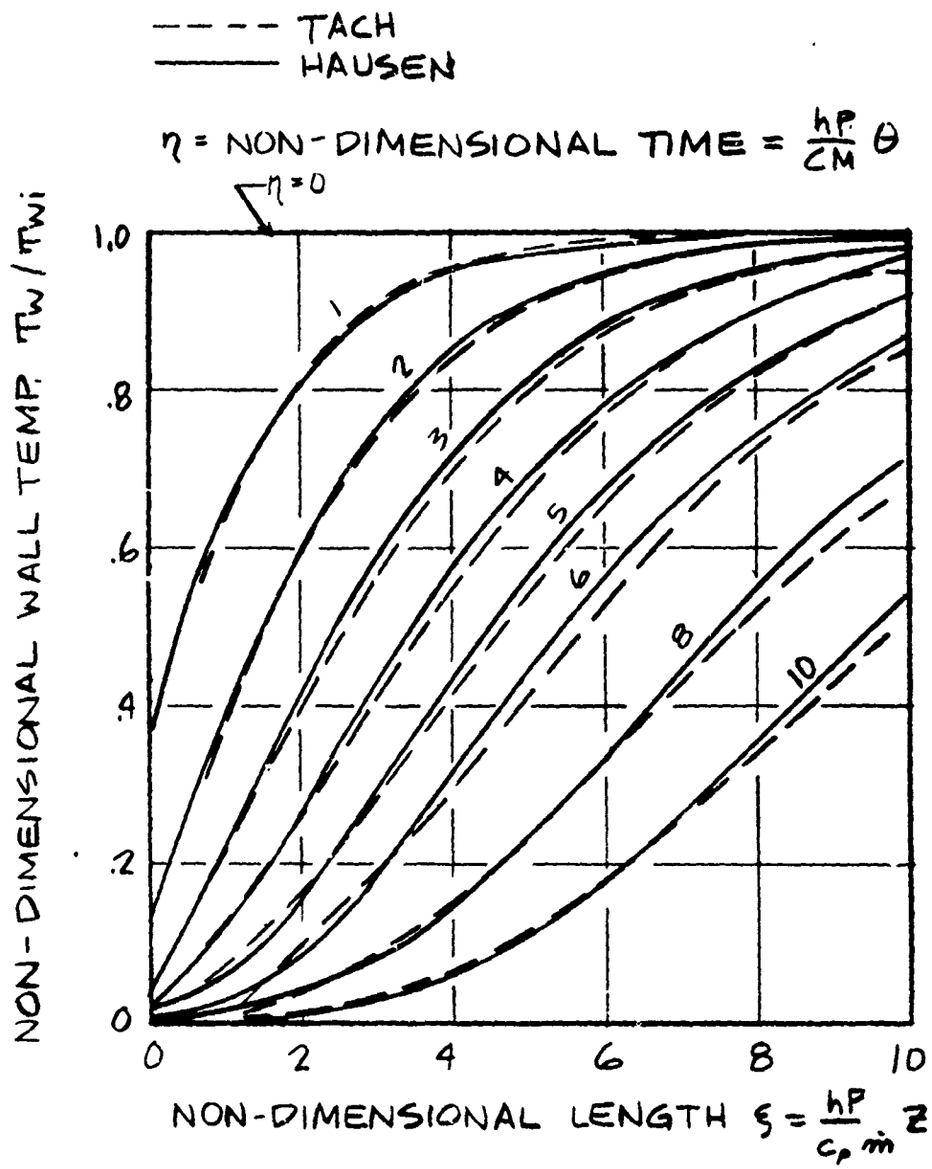

FIGURE 4 COMPARISON OF TACH WALL TEMPERATURE CALCULATIONS WITH EXACT SOLUTION OF HAUSEN

A-5251

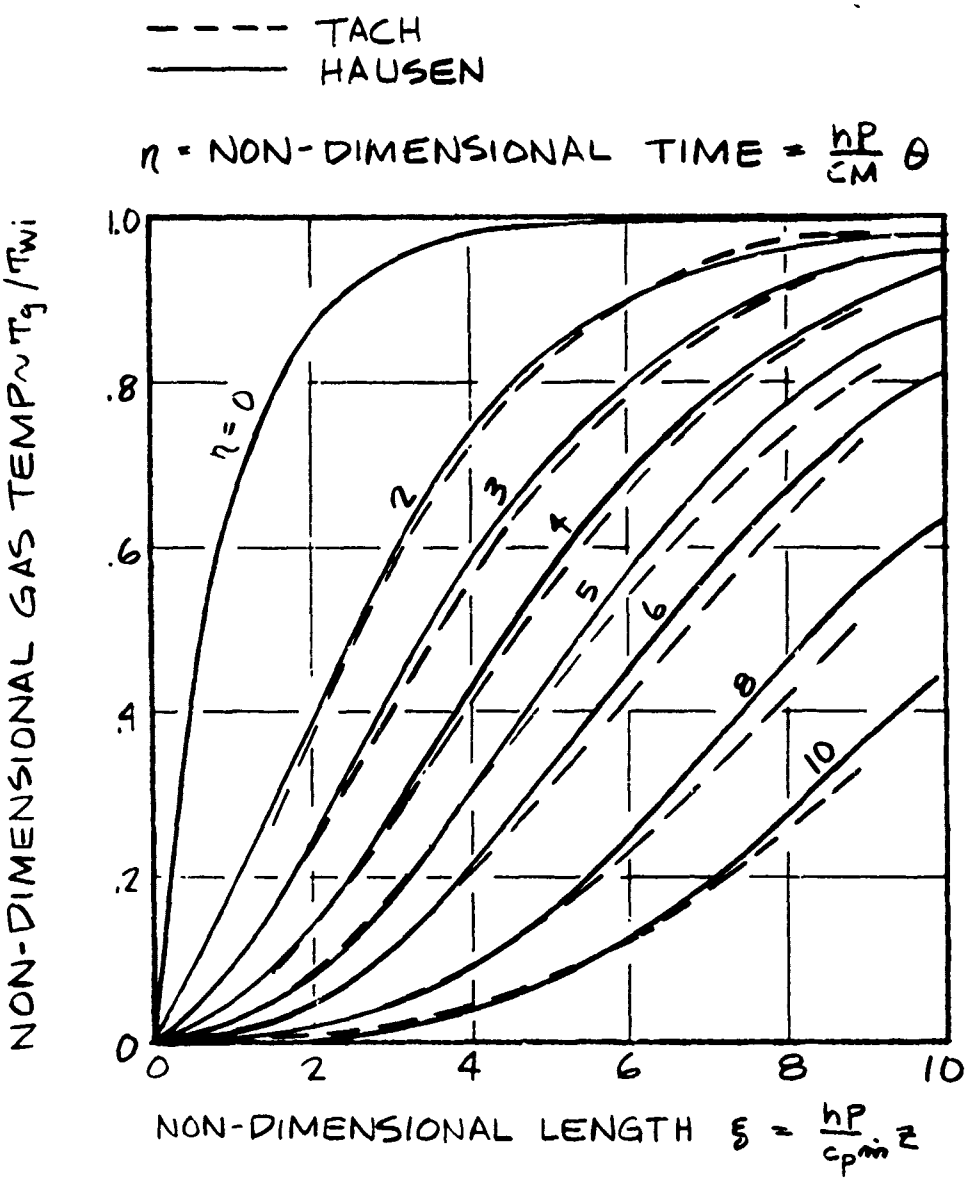

FIGURE 5 COMPARISON OF TACH GAS TEMPERATURE CALCULATIONS WITH EXACT SOLUTION OF HAUSEN

A-5235

$$T_w = T_{wall} - T_{entering\ gas}$$

$$T_{wi} = T_{wall\ initial} - T_{entering\ gas}$$

$$\xi = \frac{hP}{c_p m} Z$$

$$\eta = \frac{hP}{CM} \theta$$

Figure 5 shows similar comparisons for gas temperatures where

$$T_g = T_{gas} - T_{entering\ gas}$$

Again, good agreement was obtained.

The optimization of nodal spacing and time step size was accomplished by varying either one by a factor of two and then comparing with previous results. This optimization resulted in the selection of twelve axial nodes over the length of the 24 foot bed, five radial nodes and a minimum time step of 0.2 seconds.

The check solutions and optimizations lend confidence to the conclusion that the TACH code adequately models the gross transient thermal response of ceramic heater beds composed of multiple materials with variable properties subjected to arbitrary initial temperature distributions and accounting for variations in heat transfer coefficient.

2.1.2 Brick Segment Two-Dimensional Transient Response

The detailed two-dimensional transient thermal response analysis of individual brick segments was performed using a modified version of the ASTHMA (Ref. 8) (Axi-symmetric Transient Heating and Material Ablation Program) program. The computation method used is an alternating direction implicit-explicit method with an internally computed time step. The heated wall boundary condition is specified by a tabular list of the time dependent heat transfer coefficient and gas enthalpy at the bed location of interest. Both of these quantities were calculated by the TACH code.

The necessary ASTHMA modifications involved deletion of the material ablation portion of the code as well as conversion from axisymmetric to plane two-dimensional. The conversion from axisymmetric to plane two-dimensional was accomplished by noting that, for a constant thickness body, the axisymmetric conduction solution approaches the planar solution as the radial dimension becomes large with respect to the body thickness. Therefore a two-dimensional planar conduction

solution may be accomplished with an axisymmetric code by simply treating it as a pseudo axisymmetric problem with a sufficiently large radius of curvature. The necessary radius of curvature was determined from conduction theory such that computed heat fluxes were well within 0.1% of their planar values.

Figure 6 shows the adiabatic hexagon, previously determined from symmetry considerations (see for example Figure 2) together with additional lines of symmetry that exist within the hexagon. The shaded area indicates the basic symmetry element of the core heater brick; it was on this basic symmetry element that all detailed two-dimensional conduction solutions for web stress analyses were performed.

The thermal grid developed to model the symmetry element for the nominal cored brick geometry is shown in Figure 7. The ASTHMA code, supplied with a thermal grid of the region of interest, material properties, and time dependent boundary conditions, was employed to compute the brick segment temperature distributions for any desired bed locations or flow conditions. The ASTHMA code provides punched card output of temperature distribution data for input to thermal stress analyses.

2.2 MATERIAL THERMAL PROPERTIES

As discussed in Section 1, the two materials of interest were yttria stabalized zirconia and polycrystalline alumina. The thermal properties of these materials are required over the operating temperature range of the heater bed (i.e., 1500°R to 4500°R).

The thermal properties used and the sources from which they were obtained are covered in Sections 2.2.1 and 2.2.2 for YSZ and alumina respectively.

2.2.1 Yttria Stabilized Zirconia Thermal Properties

Zirconia is a highly refractory material with an operating temperature in excess of 4500°R. The major drawback of zirconia is that it experiences a destructive crystalline structure change in the temperature range of from 2000 to 2400°R. To counter this structure change, zirconia is stabilized by addition of oxides such as calcia, magnesia, or yttria (see, e.g., Refs. 1, 3).

The thermal properties of yttria stabilized zirconia (YSZ) were measured by Southern Research Institute and obtained by Aerotherm through References 9 and 10. The YSZ thermal properties used in analysis are summarized in Table 1.

2.2.2 Alumina Thermal Properties

Alumina is a commonly used refractory material with a maximum service temperature of about 3600°R. The properties used were for the more stable alpha

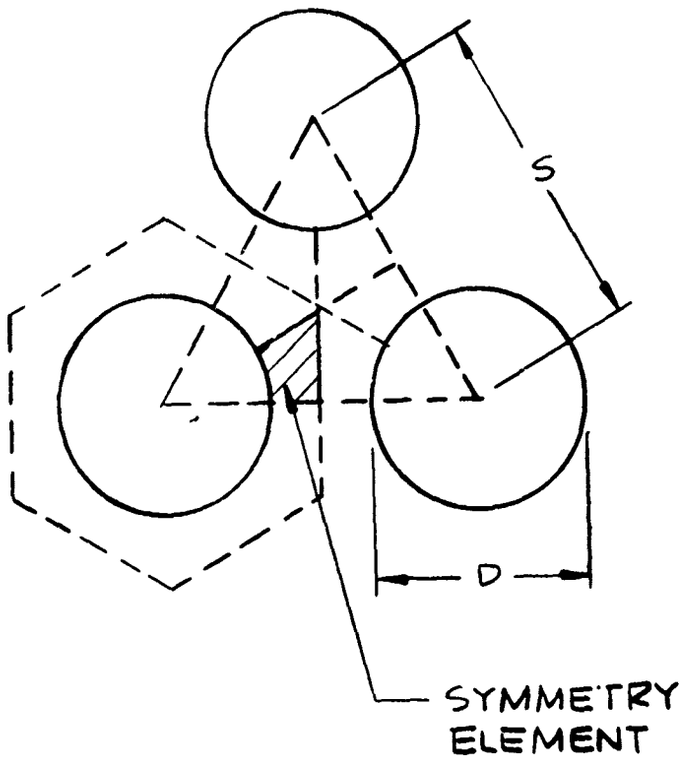

FIGURE 6 BASIC SYMMETRY ELEMENT OF CORED BRICK CERAMIC HEATER

A-5252

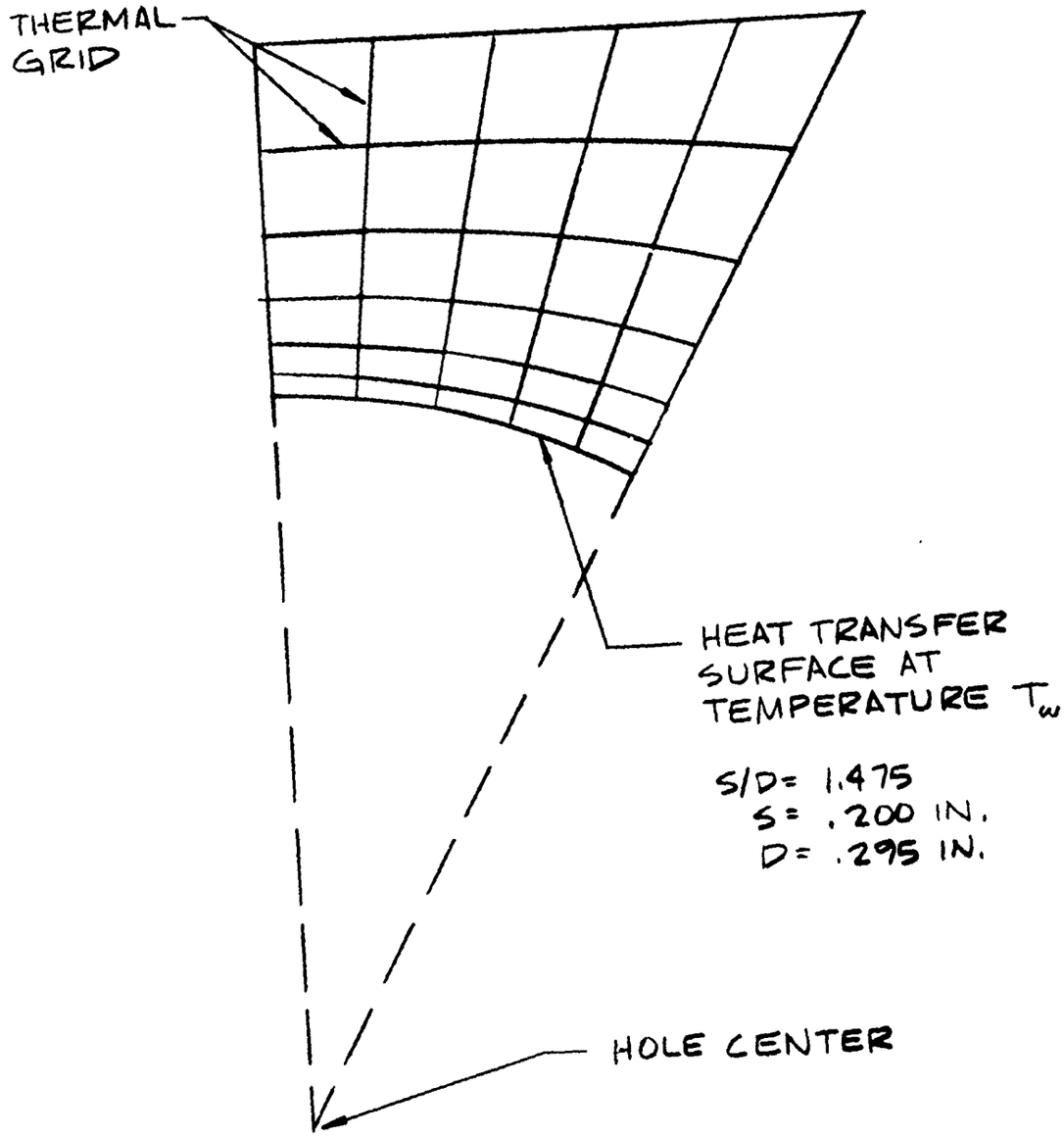

FIGURE 7 THERMAL GRID FOR SYMMETRY ELEMENT USED FOR WEB STRESS ANALYSIS

A-5253

TABLE 1

THERMAL PROPERTIES OF YTTRIA STABILIZED ZIRCONIA USED IN COMPUTATIONS

Temperature (°R)	Conductivity k (Btu/ft-sec°R) x 10^4	Specific Heat Capacity C (Btu/lb°R)
500	3.26	.111
1210	3.26	.130
1960	3.26	.150
2460	3.31	.161
2960	3.37	.171
3460	3.47	.178
3960	3.58	.186
4460	3.94	.195
4700	4.11	.199
Density = 345 lb/ft^3		

TABLE 2

THERMAL PROPERTIES OF POLYCRYSTALLINE α - ALUMINA USED IN CALCULATIONS

Temperature (°R)	Conductivity k (Btu/ft-sec°R) x 10^4	Specific Heat Capacity C (Btu/lb°R)
500	5.83	.170
1000	2.86	.255
1500	1.81	.280
2000	1.22	.310
2500	.92	.320
3000	.83	.330
Density = 248 lb/ft^3		

alumina in a polycrystalline, 100% theoretically dense form. Thermal properties were obtained from Reference 11 and are summarized in Table 2.

2.3 TYPICAL RESULTS OF THERMAL ANALYSES

Results of the TACH calculations of gross heater thermal response are presented as plots of wall or gas temperature versus axial length at various times during blowdown. Figures 8 and 9 present such plots for the nominal bed operating conditions (i.e., mass flow rate = 1150 lb/sec and sinusoidal initial temperature distribution and S/D = 1.47). Notice the effect of the sinusoidal initial temperature distribution on reducing strong temperature gradients in both axial length and time.

Typical output of the detailed transient response analysis (ASTHMA) is shown as an isotherm plot for the basic brick web symmetry element. Figure 10 presents such an isotherm plot for an element near the mid-bed location in the zirconia material (Z = 13 ft) at 10 seconds after beginning of blowdown for the nominal operating conditions.

Brick wall temperature distributions, such as shown in Figure 10, were input to the thermal stress analysis which is described in the next section.

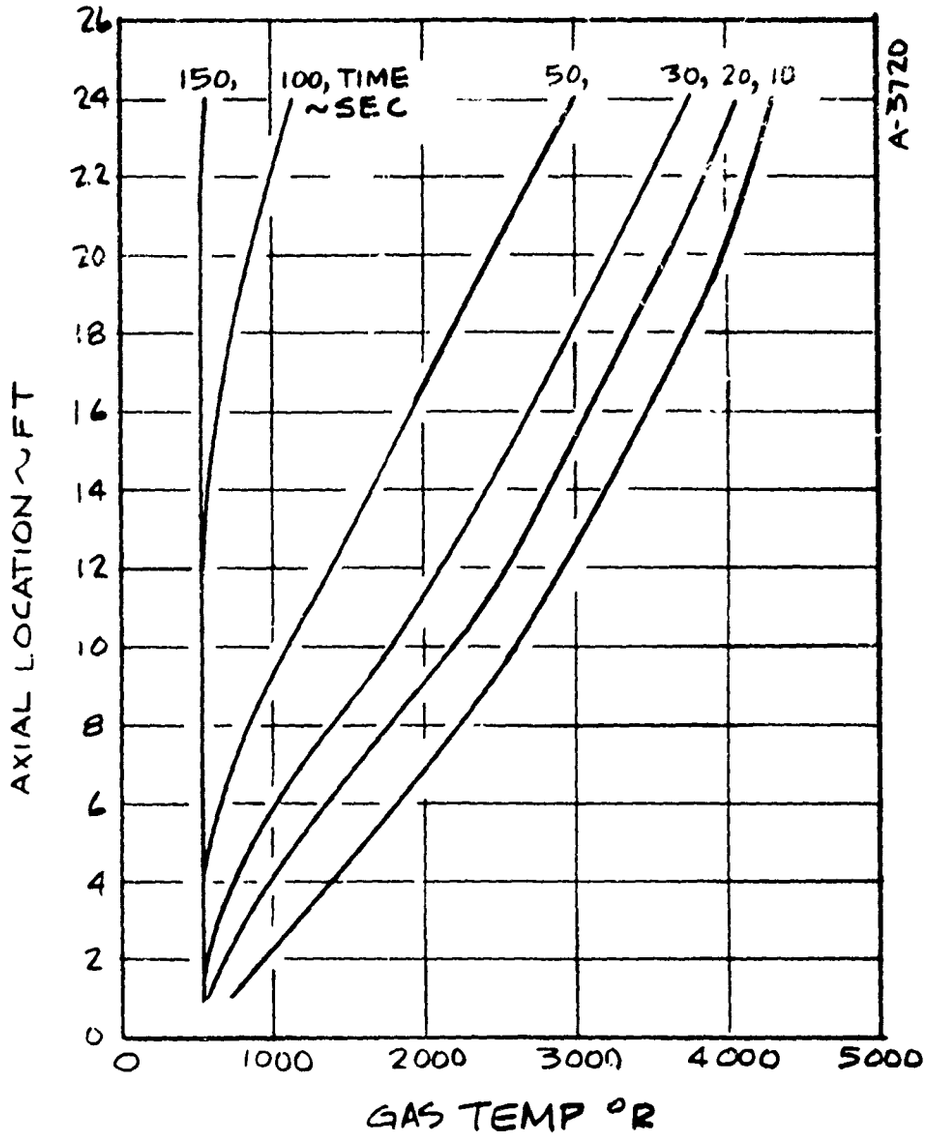

FIGURE 8 GAS TEMPERATURE HISTORY PREDICTED BY TACH FOR THE NOMINAL HEATER CONDITIONS (3,000 PSI, 1150 LBM/SEC, S/D = 1.475, SINUSOIDAL INITIAL TEMPERATURE DISTRIBUTION)

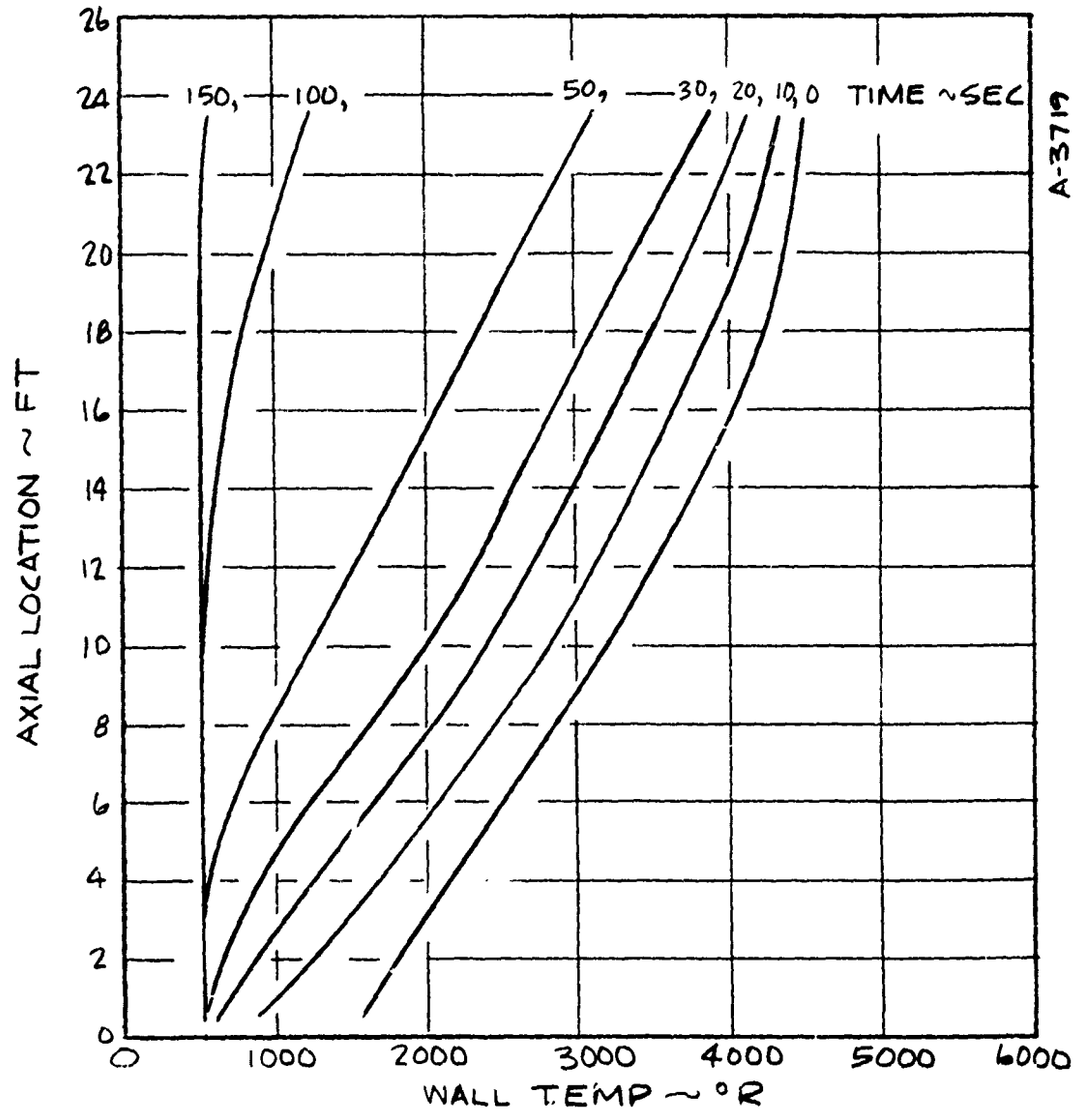

FIGURE 9 WALL TEMPERATURE HISTORY PREDICTED BY TACH FOR THE NOMINAL HEATER CONDITIONS (3,000 PSI, 1150 LBM/SEC, S/D= 1.475, SINUSOIDAL INITIAL TEMPERATURE DISTRIBUTION

NOMINAL CASE
MASS FLOW RATE = 1150 LB/SEC
SINUSOIDAL INITIAL TEMPERATURE DISTRIBUTION
MID-BED LOCATION IN ZIRCONIA MATERIAL (Z = 13 FT)
TIME = 10 SEC FROM START OF BLOWDOWN

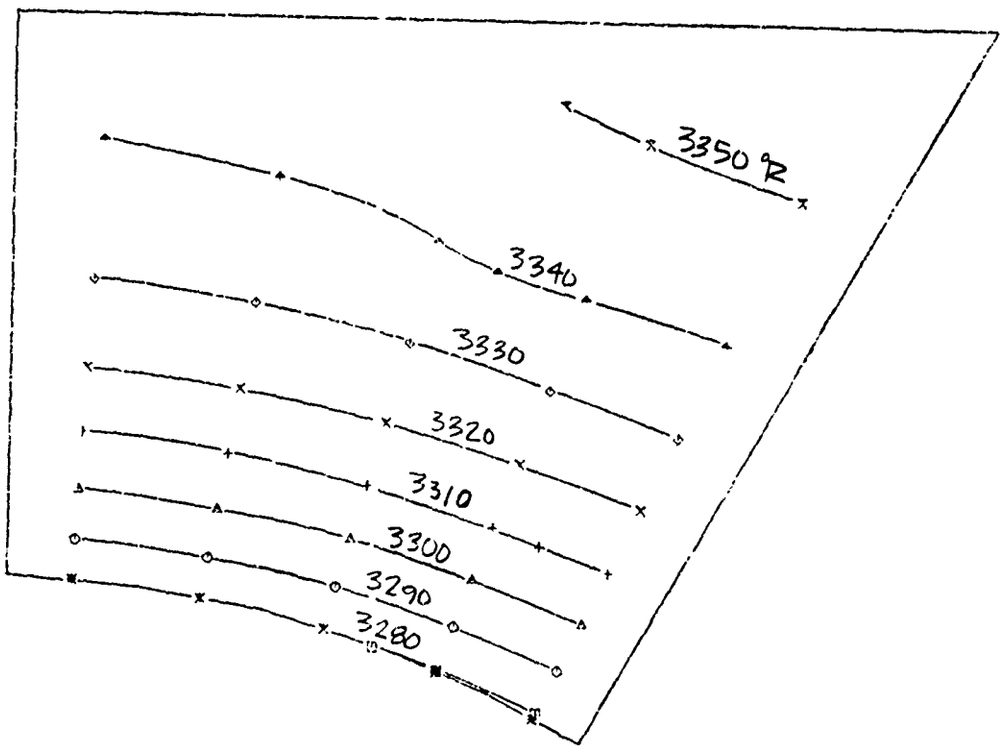

FIGURE 10 MACHINE ISOTHERM PLOT ILLUSTRATING TYPICAL OUTPUT OF THE ASTHMA DETAILED RESPONSE CALCULATIONS

A-5254

SECTION 3

HEATER BRICK STRUCTURAL RESPONSE

A variety of phenomena can potentially give rise to stresses in cored ceramic bricks in hypersonic wind tunnel heaters. Some can be analyzed quantitatively with high confidence, some can be analyzed parametrically, while others can only be considered qualitatively. These stress-affecting phenomena are discussed and analysed here in Section 3.3. However, prior to detailed discussion of the analyses, the material mechanical properties used are presented (in Section 3.1) and the numerical stress analysis computer code used is discussed (in Section 3.2). Conclusions and recommendations based on these analyses are presented in Section 4.

3.1 MATERIAL MECHANICAL PROPERTIES

The thermal-mechanical properties of Yttria Stabilized Zirconia (YSZ) were determined experimentally by Southern Research Institute (Reference 12). Since the material is isotropic (mechanically), the relevant properties needed for a thermal stress analysis are (a) E, the elastic modulus, (b) ν, Poisson's ratio, (c) α, the coefficient of linear thermal expansion and (d) Y, the yield stress which in this case is the ultimate stress. All of these properties are required for the temperature range 0 - 4000°F. The shear modulus (G) and shear yield stresses (k) were determined from the isotropic formulas

$$G = \frac{E}{2(1 + \nu)} \text{ and } k = \frac{Y}{\sqrt{3}}$$

The material behaves in an elastic-brittle manner, and consequently the yield stress is the ultimate stress. The experimental results were interpreted by both AFML and ARL in conjunction with Aerotherm and Weiler Research to determine the most probable valves to use in the thermal stress analyses. The results of this interpretation are shown in Figures 11a and 11b. Poisson's ratio (ν) was assumed constant over the temperature range. Experimental data points are shown by encircled points in these figures. The data shown above 3400°F are extrapolations since they are needed for the analysis. It is understood that the melting temperacure of YSZ is approximately 4500°F and so the valves shown above this temperature are fictitious and only used for the purposes of the thermal stress analysis. Additionally, the coefficient of linear thermal

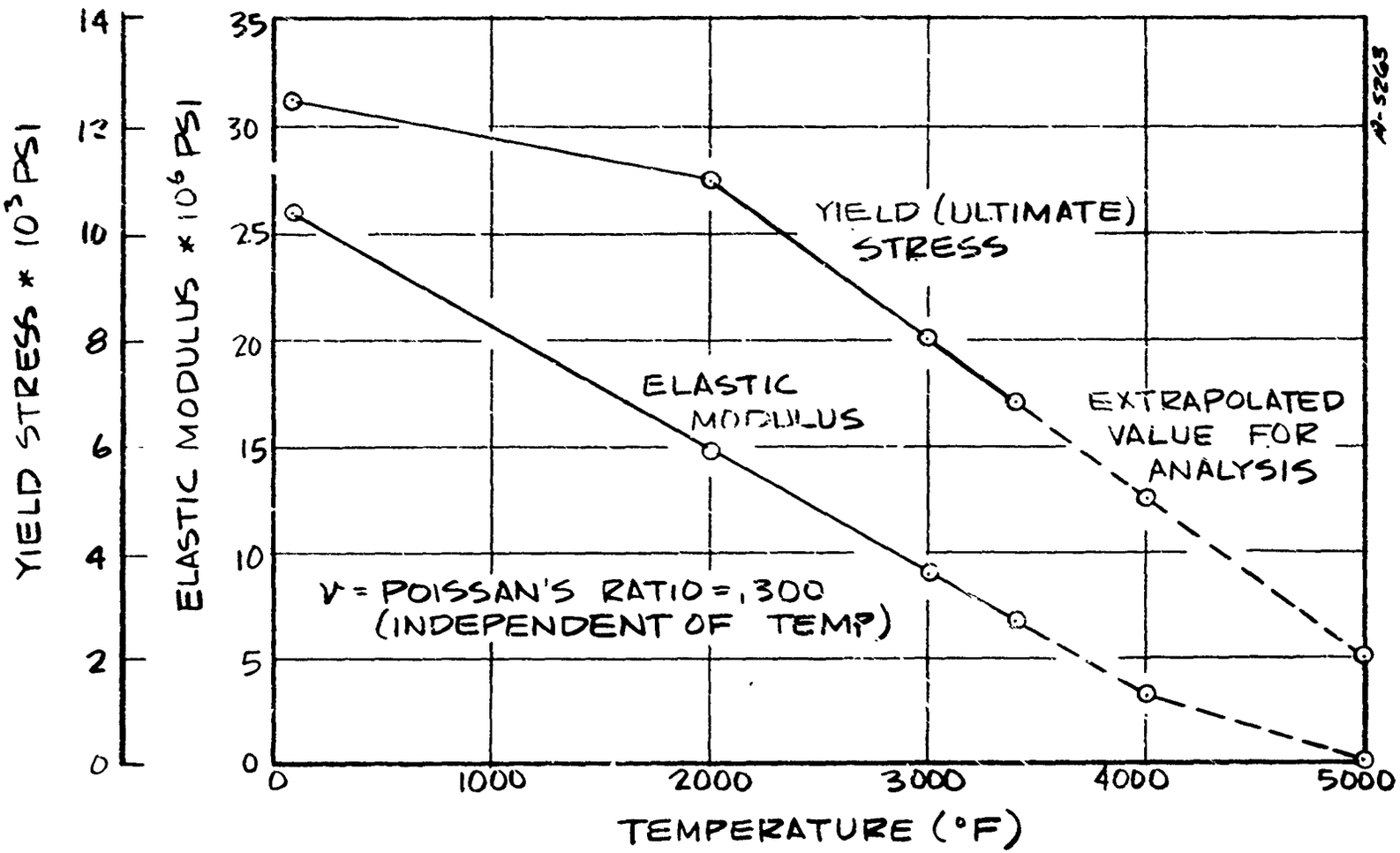

A) ELASTIC MODULUS, E AND YIELD STRESS, Y

FIGURE 11 MECHANICAL PROPERTIES OF FULLY CUBIC YTTRIA STABALIZED ZICRONIA (YSZ) USED IN ANALYSIS

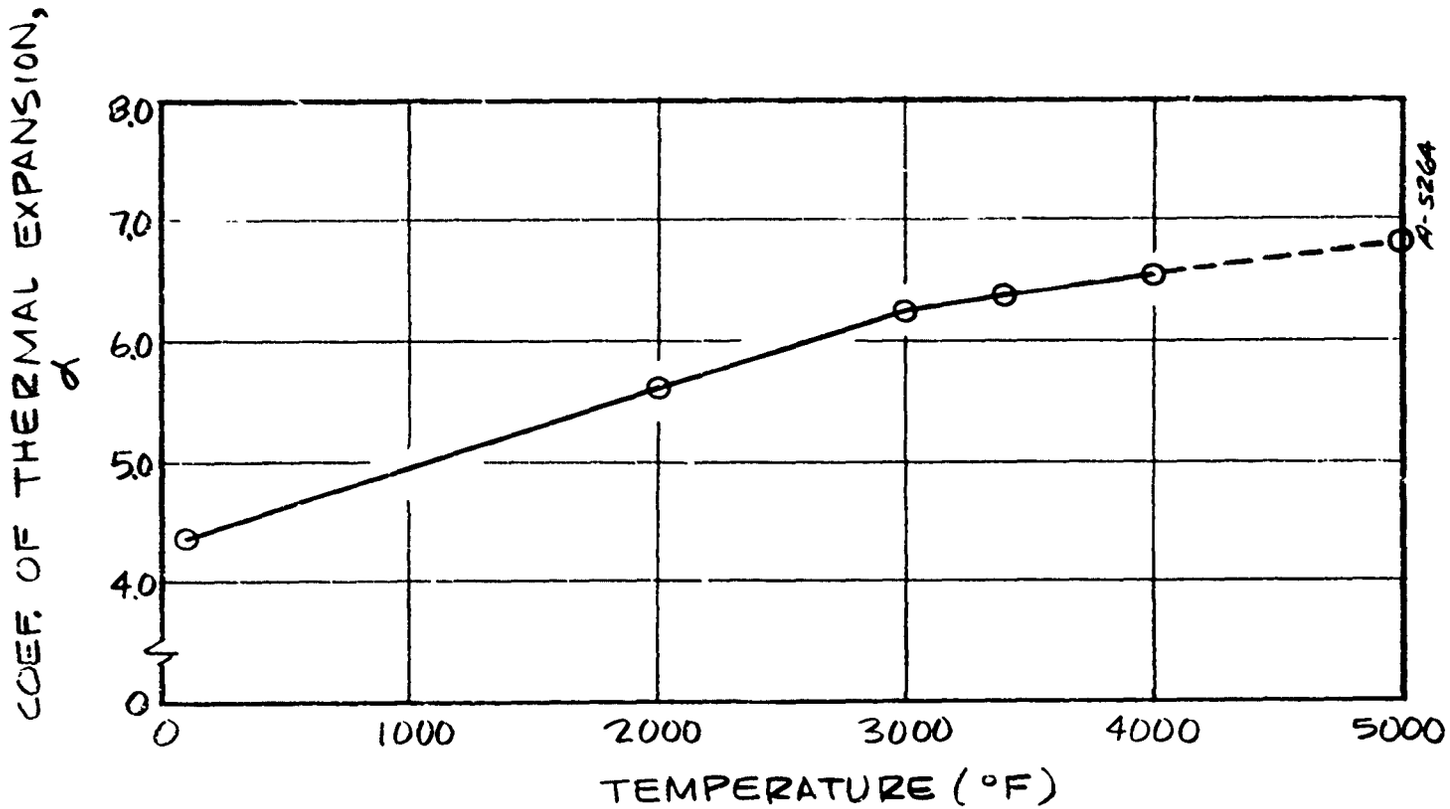

B) COEFFICIENT OF THERMAL EXPANSION, $\alpha = \epsilon^{th}/(T-T_0)$

FIGURE 11 (CONCLUDED)

expansion, α, was determined from the thermal strain ε^{th} data by $\alpha = \varepsilon^{th}/(T - T_o)$ where T_o was the reference temperature (70°F). All of these properties are listed in Table 3 as functions of temperature.

TABLE 3

YTTRIA STABILIZED ZIRCONIA MATERIAL PROPERTIES

Temp °F	E psi x 10^{-6}	ν	α in/in x 10^{+5}	Yield Stress psi x 10^{-3}
70.	26.0	.30	.4390	12.5
2000.	14.8	.30	.5606	11.0
3000.	9.0	.30	.6229	8.0
3400.	6.8	.30	.6360	6.8
4000.	3.3	.30	.6514	5.0
5000.	.01	.30	.6800	2.0

3.2 FINITE ELEMENT THERMAL STRESS ANALYSIS CODE

The different models to be discussed in subsequent sections were analysed using the DOASIS thermal-stress analysis computer code (Ref. 13). This is a general 2-dimensional (plane and/or axisymmetric) code which can analyse solid structures composed of temperature dependent materials and loaded by thermal gradients, boundary pressures and body forces. For the present cases, only linear thermal elastic stress analyses were performed.

To use this code, the body is first subdivided into a large number of small, discrete pieces, called finite elements. Relationships are written describing the state of displacement within these elements based upon the element's temperature, material properties, etc. These relationships (linear algebraic equations) are then connected mathematically such that displacement continuity exists between the elements. The resulting set of equations are solved and yield the displacements of the corners (nodes) of the elements, from which the strain and thus stress within each element may be calculated. Once the resulting stresses are known for the body in question, iso-stress contour plots can be made which show lines of constant stress existing within the body. For each of the different models analysed, a finite element mesh was generated and the appropriate boundary conditions for these models were applied. A stress analysis was performed and the results were plotted. The finite element discretation (mesh) used will be shown along with the resulting iso-stress contour plots for each of these models, where appropriate. For further details concerning structural finite element analysis techniques, see References 13, 14, or 15.

3.3 BRICK STRESS ANALYSES

The objective of the thermal stress analyses performed is to lend insight into the question, "what type of thermal stresses developed in the cored bricks could give rise to thermal stress failures, i.e., cracks induced by thermal stress?" To accomplish this objective, it was originally planned to examine primarily the web stresses existing at the hole surfaces due to the rapid brick cooling around the holes during blowdown. Subsequently, additional types of thermal stress analyses were performed to help lend insight into possible stress producing conditions which could lead eventually to fracture.

Consider the cross section of a hexagonal cored YSZ brick as shown in Figure 1. The brick measures approximately 2.78 in. across the flats. This hexagonal brick contains 91 holes in a hexagonal pattern. The section between the holes is called the web. During a blowdown condition, air passes through the holes, heat is rapidly transferred from the web material and thereby creates thermal gradients throughout the bricks. If the geometry of the bricks was perfect, the connections between bricks resting on top of one another perfect, flow conditions were uniform, and no heat was transferred from the edge of the bricks or bed, then the thermal gradients induced in the bricks due to this rapid cooling would be uniform and regular. However, since these conditions are not true in practice, irregularities do occur and therefore ideal conditions are not realized. Consequently, concern arises for other stress producing conditions which will occur due to these irregularities, such as concentrated loads due to two irregular surfaces resting on top of one another.

The major effect of irregularly shaped bricks is that nonlinear thermal gradients are induced across the bricks, and these give rise to thermal stresses. The reason for this is as follows: If a body (with constant material properties) is heated uniformly, the whole body expands uniformly and no stresses are induced, assuming that the body is not constrained in any manner. It is also true that if a linear temperature gradient is imposed on a body, the body will deform linearly and again no stresses are induced. This follows from thermal elasticity theory (e.g., Ref. 17). Thus, that portion of a temperature gradient which induces thermal stresses into a body is the nonlinear part. In this case, potential effects of nonlinear temperature distributions across the heater bricks were investigated, in addition to the previously discussed simple web stresses.

To summarize, after reviewing the cored brick heater matrix construction and operation, three different stress conditions were analyzed quantitatively relative to their potential for causing stresses large enough to cause brick fracture. First, the thermal gradients induced into the web sections of the bricks during blowdown create thermal stresses, as previously discussed, since

these thermal gradients are not linear through the brick web. Secondly, non-linear thermal gradients can be induced across a whole brick due to one side being cooled faster than the other. This would arise if some of the holes in one side of the brick didn't match up correctly and thus constrict the air flowing through these holes (see Appendix B). Consequently, both radial (across the bricks) and axial (along the bricks) nonlinear temperature gradients could be induced creating thermal stresses. Thirdly, if the end surfaces of the bricks are not perfectly flat, then when the bed is assembled by stacking bricks on top of one another, these non-flat surfaces will transmit the weight of the bricks at points (small areas of contact) rather than uniformly across the whole cross section. This will give rise to what is called contact stresses. Obviously, the compressive components of these contact stresses will be high, but there will also be tensile stresses induced, which are the ones of importance here.

The next three subsections will present the analyses of these three different stress conditions. Following these discussion, the combined effects of these three will be discussed, and fracture conditions will be illustrated. Since these three conditions are not the only situations which can cause stresses to occur in the bricks, other effects, which do not easily lend themselves to analytical investigation, will be discussed qualitatively in subsequent subsections.

3.3.1 Web Stress Analyses

In general, an accurate, detailed stress analysis of any one cored brick would result from a three-dimensional model, accounting for all irregularities in geometry, etc. However, for the present case, the thermal stress response of the cored bricks will behave fairly uniformly at each axial station along the length of the brick, where deviations from this uniformity will occur only on the ends of the brick. It was therefore decided that a generalized two-dimensional plane strain or plane stress analysis of a typical cross-section would yield results fairly typical of what any detailed three-dimensional stress analysis would produce for stresses in the web section of the brick.

The term generalized plane stress (or strain) means that the stress (or strain) normal to the two-dimensional plane of analysis is known and given for purposes of analysis. For the analyses in question, three different types of generalized plane analyses were performed. First, if the brick is sufficiently long, a cross-section in the middle of the brick will not displace axially due to the material above and below it preventing such movement. This constitutes a state of plane strain in which the axial component of strain is zero. Second,

if the brick is sufficiently thin, the axial components of stress on the top and bottom surfaces are zero and therefore axial stress developed through the thickness of this section cannot be too different from zero. Therefore, a state of plane stress exists in which the axial component of stress is zero. Third, if one considers a typical section existing midway in the whole bed, then 12 feet of bricks above the cross-section of interest will exert a dead weight loading on the cross-section of interest. This dead weight may be considered as a specified axial stress equal to the reacting pressure given by

$$p = \text{density} \times \text{height} = 345 \frac{\text{lb}}{\text{ft}^3} \times 12 \text{ ft} \div 144 \frac{\text{in}^2}{\text{ft}^2} = 28.9 \text{ psi}$$

i.e., the axial component of stress = 28.9 psi and is constant across the cross-section of the bed. Therefore, a state of generalized plane stress exists in which the normal (axial) component of stress is known.

Now, when examining the geometry of the cross-section shown in Figure 1, an additional simplifying assumption may be made, namely, symmetry. Due to the large number of uniformly placed holes (in a hexagonal pattern) one would expect a symmetrical temperature response to exist in the webs as discussed in Section 2.1.2. Similarly, a symmetrical thermal stress response will exist except near the sides of the cross-section where the symmetry conditions do not hold. However, in the center of the brick, symmetry conditions do hold and may be used. Therefore, a typical symmetry web section was chosen for the above mentioned three types of plane analyses. This typical section was shown in Figure 6. The actual geometry of the symmetrical section is determined by the spacing (S) and diameter (D) of the hole pattern. The boundary conditions used in these plane thermal stress analyses are shown in Figure 12, where the symbolic rollers indicate that points along the three cut boundaries may move along these cut edges but not normal to them. The fourth side which is the hole surface is considered free.

The predicted temperature distributions were translated from the thermal analysis grids to the stress analysis grids following the extension technique described in Reference 16, Appendix E. This extension involves an extrapolation of the temperature field from interior points to the three interior boundaries formed by the lines of symmetry. Since these three boundaries were all assumed insulated in the thermal analysis, this extension technique was simplified and proved to be highly accurate when performed.

Due to the three boundary conditions shown in Figure 12, any uniform rise in temperature applied to the symmetrical section will cause a uniform

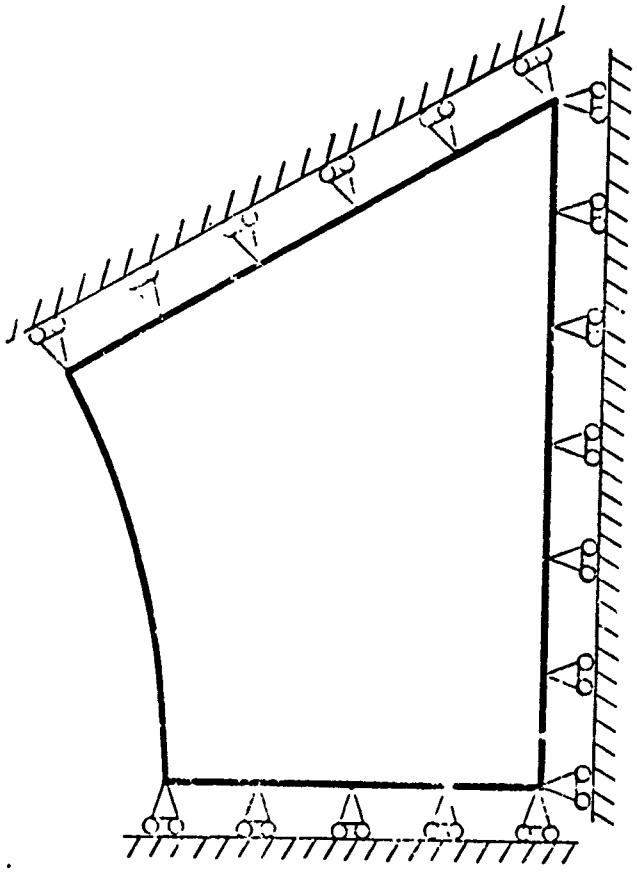

A-5265

FIGURE 12 MECHANICAL BOUNDARY CONDITIONS OF TYPICAL SYMMETRICAL SECTION

expansion of this material, and thereby induce compressive stresses which in reality would not be present. It is well known in the theory of thermal stress analysis, that a free body will contain zero stresses due to a constant or linear varying thermal gradient as explained earlier. Considering the brick as a whole, being free, then a uniform rise in temperature will create zero stresses throughout the brick. To duplicate this condition in the symmetrical section web stress analysis, the weighted mean temperature was found via

$$T_{mean} = \frac{\int T \, dA}{\int dA}$$

and used as the stress free reference temperature in the analysis.

The nominal S/D ratio chosen for the web stress analyses was S/D = 1.475 with a hole diameter of D = 0.20 inch. These were the values used for determining the geometry of the symmetrical section shown in Figures 6 and 12.

The in-plane stress analysis for the symmetrical section described here was calculated for three cases. They are: Case I, $\sigma_z = -28.9$ psi which corresponds to the dead weight of 12 feet of YSZ bricks, Case II, $\sigma_z = 0$ which is the plane stress case and Case III, $\varepsilon_z = 0$ which is the plane strain case. The time at which stresses were to be analyzed for these cases was selected with the objective of considering the maximum thermal stresses. The temperature distribution predictions were interrogated to determine the time at which maximum $(T_{web\ center} - T_{hole\ surface})$ occurs. This corresponds closely to the time of maximum thermal stresses and it occurred at about 10 seconds for the S/D = 1.47 nominal blowdown condition.

The stress results for Case I are shown as iso-stress contour plots (i.e., lines of constant stress) in Figures 13a through 13f. The finite element discretation and temperature distribution for this nominal blowdown case at time = 10.0 seconds are also shown. The nominal blowdown case is for P = 3000 psi, mass flow rate = 1150 lbs/sec and a sinusoidal initial temperature distribution T = 4500°R to 1520°R with a brick geometry of S/D = 1.47, as described earlier in this report. The axial location of these in-plane stress analyses is at the YSZ - Al_2O_2 interface which is at the middle of a 24-foot column of bricks.

When examining Figures 13 a through 13f, one notices that the maximum tensile stresses occur at the hole surface and are almost in the hoop tension direction around this hole, with a value of $\sigma_{hoop} = 3000$ psi (c.f., Figure 13f, σ_{max}). This was as expected. The other interesting stress plot is of the shear stress τ_{xy} shown in Figure 13e. Here we see that a large amount of shear distortion occurs near the hole surface and along the longer of the two cut symmetrical

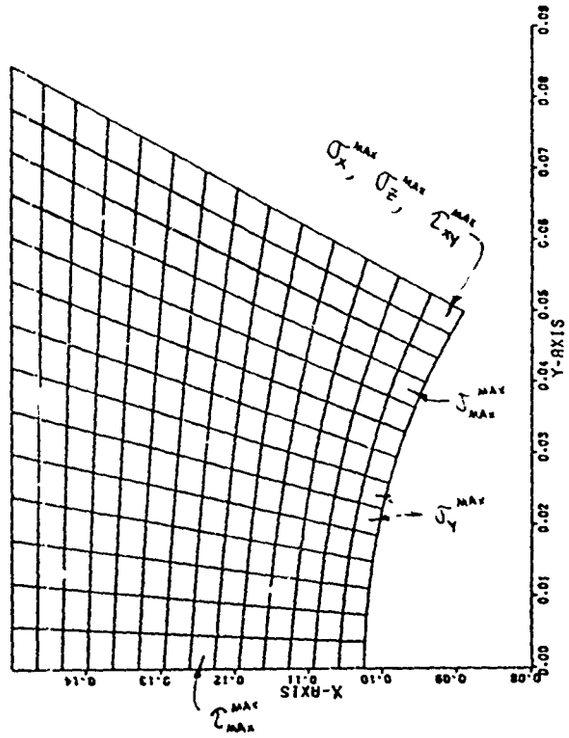

A) FINITE ELEMENT MESH

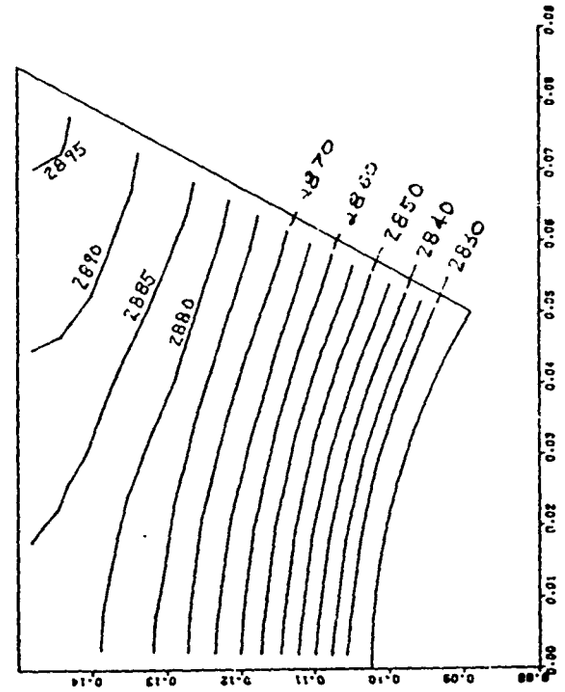

B) TEMPERATURE FIELD (°F)

A-5266

FIGURE 13 RESULTS OF WEB STRESS ANALYSIS "CASE I" CONDITIONS (PLANE STRESS, $\sigma_z = -28.9$ PSI) NOMINAL BLOWDOWN CONDITIONS, TIME = 10 SEC, S/D = 1.47

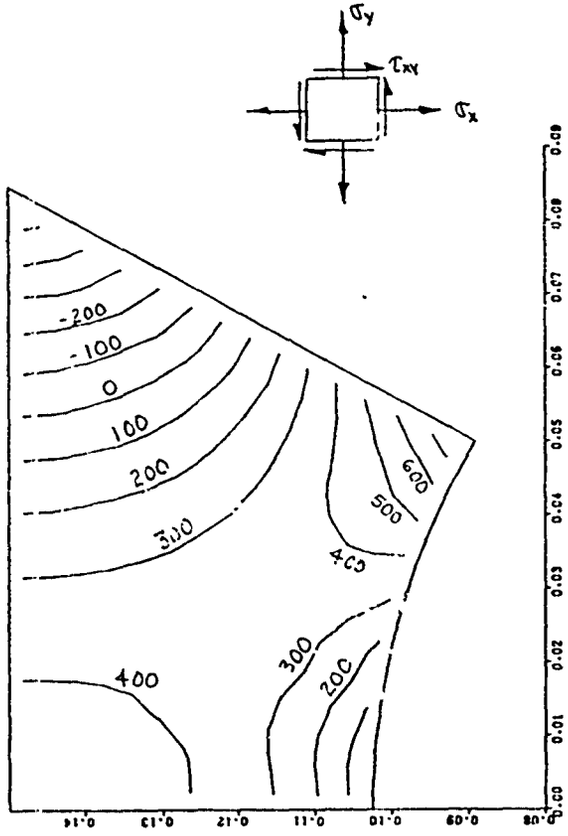

C) STRESS, σ_X

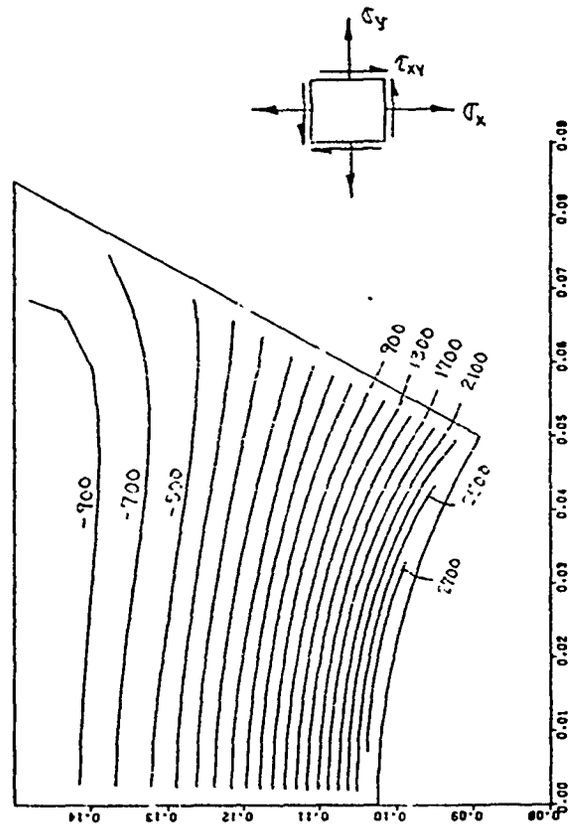

D) STRESS, σ_Y

A-5267

FIGURE 13 (CONTINUED)

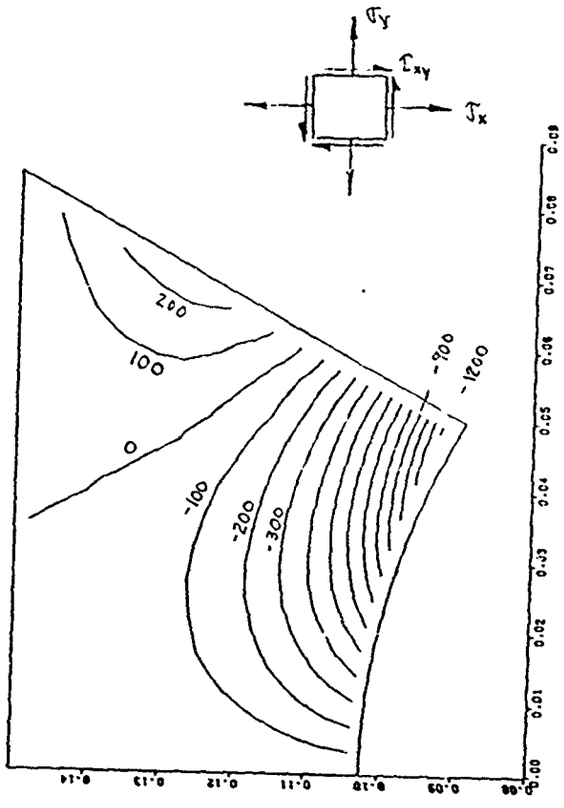

E) STRESS, τ_{XY}

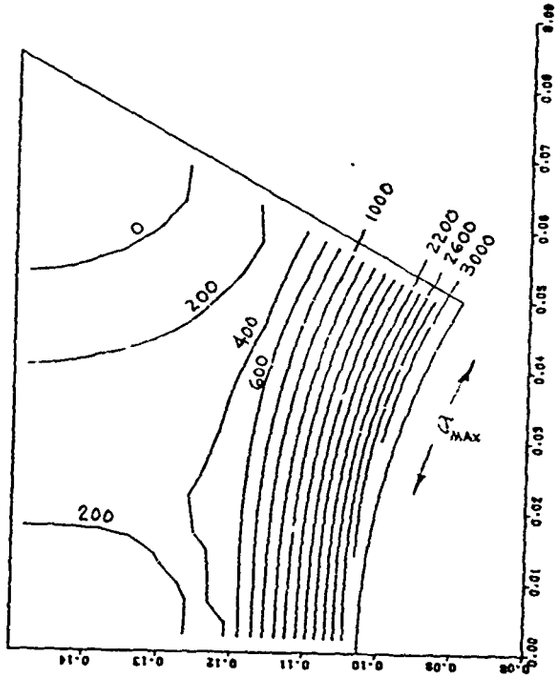

F) STRESS, σ_{MAX}

M-5268

FIGURE 13 (CONCLUDED)

sides which are perpendicular to the hole surface (along the top side of the symmetrical section shown in Figure 13e). This shearing is caused by the fact that the hexagonal web section, when subdivided into symmetrical sections as shown, does not have the same shape as sectors of an equivalent cylinder. In an equivalent cylinder sector model, the shear stresses would be zero. In the analysis presented here, they are not zero but rather 40 percent of the magnitude of the maximum stresses. This is significant when considering the overall effects of the stresses produced within this symmetrical section.

The plane stress ($\sigma_z = 0$) case (Case II) produced results which were almost identical to this generalized plane stress ($\sigma_z = 28.9$ psi) case (Case I) and so were not plotted. The reason for the similarity is that an axial stress of $\sigma_z = -28.9$ will interact through the coupling expressed by Poisson's ratio ($\nu = 0.30$) and only produce stresses in the plane of approximately 8.5 psi which is negligible as compared to 3000 psi.

The plane strain ($\varepsilon_z = 0$) case, denoted Case III, produced significant tensile stresses in the axial direction of the bricks. The iso-stress contour plots (i.e., lines of constant stress) are shown for this case in Figures 14a through 14e. The finite element discretation and temperature distribution are the same as for the other cases and are shown in Figures 13a and 13b.

Figures 14a through 14e show that the maximum tensile stress of 4250 and 4000 psi occur for the hoop tension direction (Figure 14e)and the axial direction of the bed, i.e., the component σ_z (Figure 14c), respectively. The total state of stress along the hole surface is triaxial since the component σ_x (approximately normal to the hole surface) is also tensile, varying between 100 psi to 1000 psi as shown in Figure 14a. Therefore, this triaxial state of stress $\sigma_x:\sigma_y:\sigma_z$ varies from 0.25 : 1.0 : 1.0 to 0.025 : 1.0 : 1.0 along this hole surface, the peak being centered near the longer of the two sides which are perpendicular to this hole surface (the top side shown in these figures).

The axial stress (σ_z) developed for this plane strain case is caused by the fact that the colder material at the hole surface location wants to contract in the axial direction. However, the hotter material in the center of the web resists this contraction, thereby causing this hole surface region to go into tension. If the brick is long enough in this axial direction, then the center section of the brick will be in a state of plane strain ($\varepsilon_z = 0$). Shorter length bricks will deviate from this pure plane strain case and as the length of the brick goes to zero, and a plane stress case develops. The exact magnitude of plane strain (or plane stress) conditions for short length bricks (approximately 2" in axial length) would have to be determined by a three-dimensional analysis.

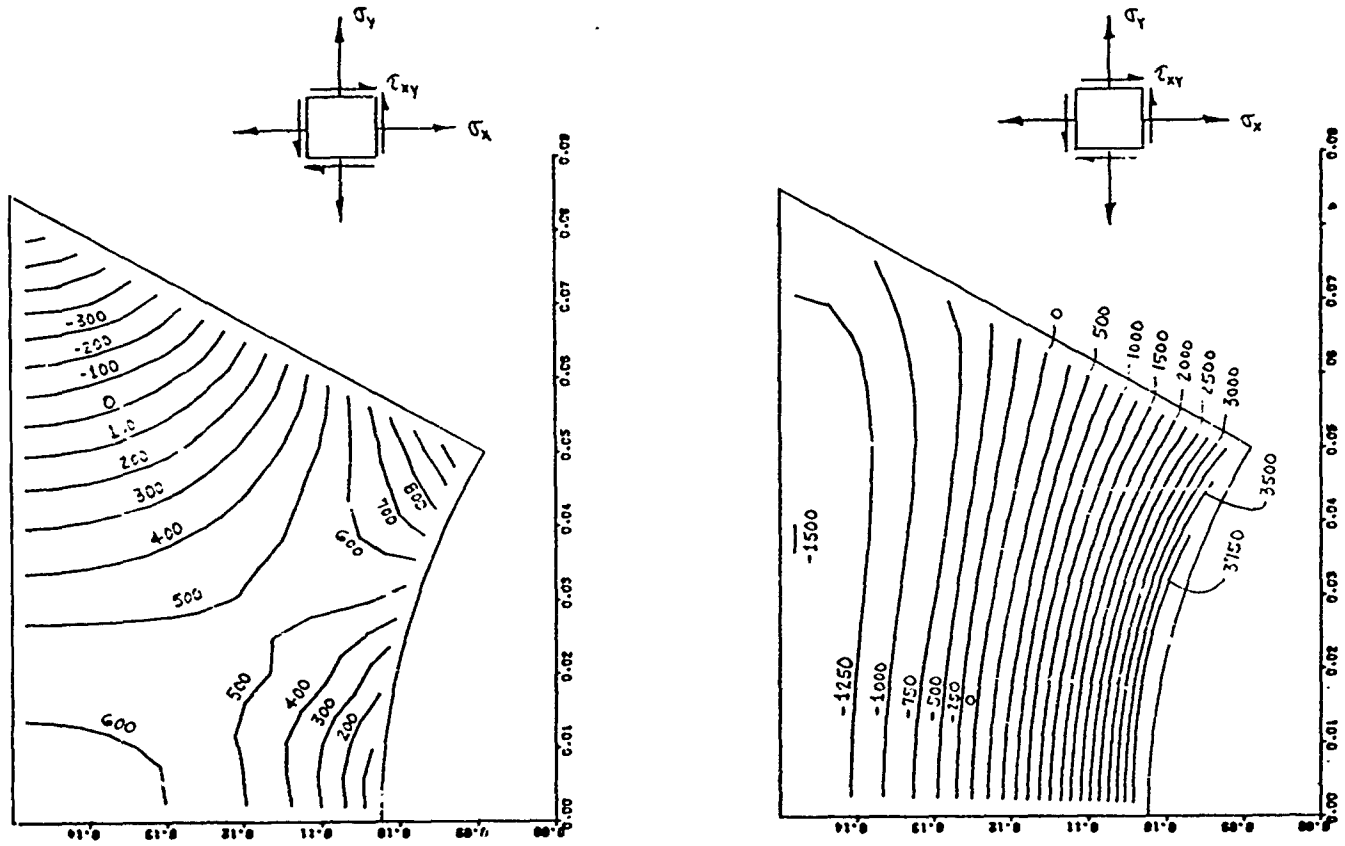

A) STRESS, σ_X

B) STRESS, σ_Y

FIGURE 14 RESULTS OF WEB STRESS ANAYSIS "CASE III" CONDITIONS (PLANE STRAIN, $\epsilon_z = 0$) NOMINAL BLOW-DOWN CONDITIONS, TIME = 10 SEC, S/D = 1.47

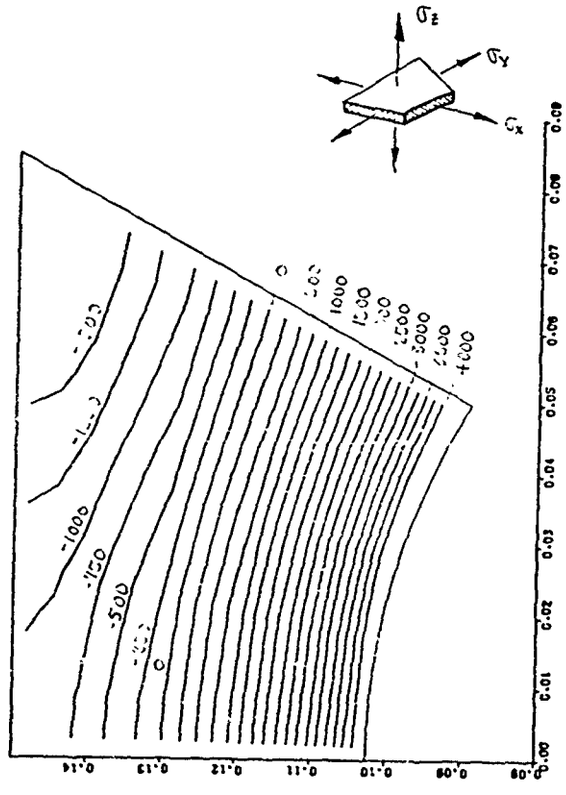

C) STRESS, σ_z

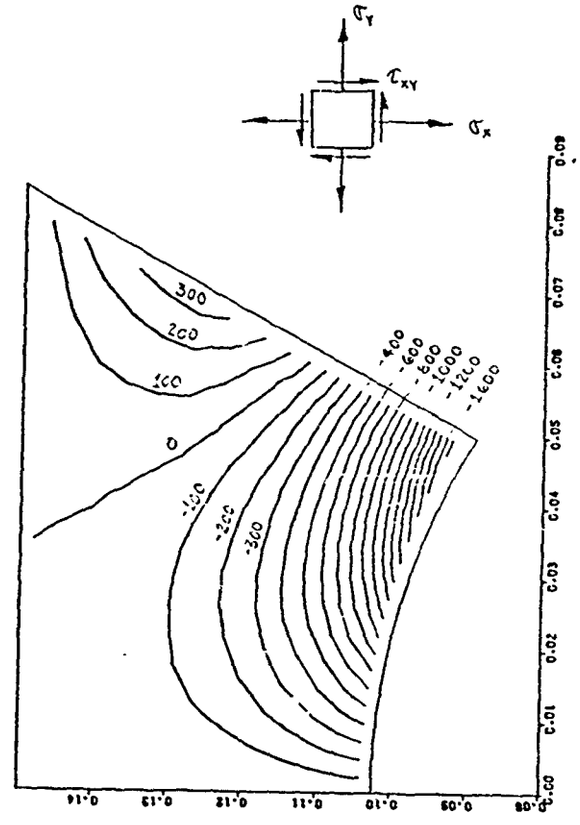

D) STRESS, τ_{XY}

A-5270

FIGURE 14 (CONTINUED)

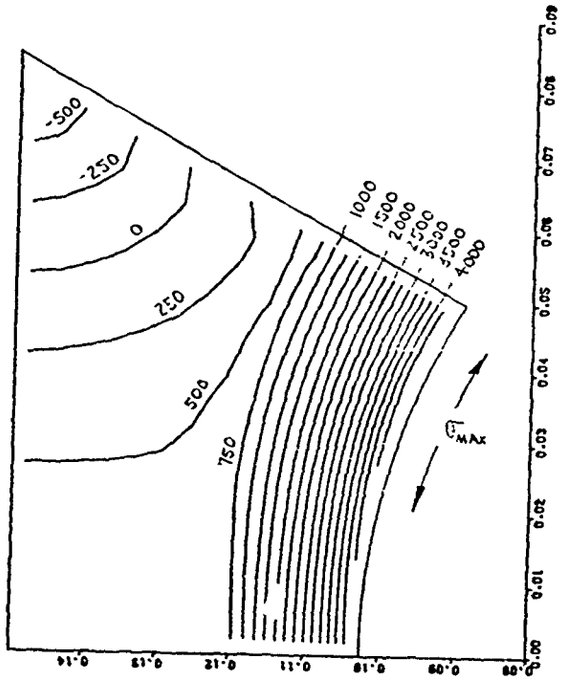

A-5271

E) STRESS, σ_{MAX}

FIGURE 14 (CONCLUDED)

The results of the maximum stresses for all three cases are presented in Table 4. The location where these maximums occur are indicated in Figure 13a. The interesting thing about the results presented in Table 4 is that the plane strain case (Case III) produced the maximum tensile stresses, not only in the plane but also normal to the plane (axial direction in the bed). Both the plane stress (Case II) and the generalized plane stress (Case I) solutions produced a biaxial state of stress (in the plane) which had a magnitude of only approximately 75 percent of the plane strain case.

TABLE 4

MAXIMUM STRESS RESULTS OF IN-PLANE ANALYSES

Case	σ_x^{max}	σ_y^{max}	τ_{xy}^{max}	σ_{normal}^{max}	σ_{max}^{max}	τ_{max}^{max}
I (σ_z = -28.192)	750	2764	-1210	-28.192	3041	1492
II (σ_z = 0.0)	747	2751	-1205	0	3028	1486
III (ε_z = 0.0)	1071	3952	-1730	4229	4346	2134

The web stresses analyzed in this section will be considered with respect to other stresses and the material strength in Section 3.3.4.

3.3.2 Nonlinear Temperature Gradients Across Bricks

Another source of thermal stresses which could exist in the cored bricks is due to non-uniform heating conditions which give rise to non-uniform temperature gradients within the brick as discussed in Section 3.3. Again, to represent this behavior, a three-dimensional model would be the most accurate course to follow, but the degree and type of nonlinear temperature gradients is not known. To keep the thermal stress analyses within economical bounds, and in view of the fact that the actual nonlinear temperature gradients are unknown, an equivalent cylinder two-dimensional model was used with various hypothetical nonlinear temperature gradients. The limitations of this equivalent cylinder approximation are further described in Appendix C.

This equivalent cylinder model was developed based upon the hypothesis that the total volume of the equivalent cylinder equaled the total volume of the hexagonal brick. Since the height of the hexagonal brick and cylinder are the same, this reduces to finding the radius of the equivalent cylinder which will make the total cross-sectional areas the same. This same type of geometry problem (i.e., find an equivalent cylinder for a given hexagon) was solved in Section 2.1.1 and is illustrated in Figure 2 where the equivalent cylinder

cross-section is indicated. This equivalent cylinder for the entire brick has a radius given by $a = (\sqrt{3}/2\pi)^{1/2}$ W.

The boundary conditions of the two-dimensional model representing the equivalent cylinder are shown in Figure 15. Notice points along the centerline are free to move axially but are prevented from moving radially as indicated by the rollers. The free brick is fixed against rigid body motion by pinning the point on the centerline at the bottom surface. The remaining three sides are free. Two basic types of hypothetical nonlinear temperature profiles were considered in the equivalent cylinder analyses. These were axial gradients and radial gradients as shown in Figure 16. The radial gradients are specified by two parameters, T_{Base} which is the base temperature and ΔT which is the degree of nonlinearity. Assuming a quadratic form for this radial temperature profile, and a cylinder radius "a", then the radial temperature (for all axial locations) is given by

$$T(r) = T_{Base} + \left(1 - \frac{r^2}{a^2}\right)\Delta T \qquad \text{(all z)}$$

The axial gradients are specified by three parameters, T_{Bottom} and T_{TOP} which are the temperatures at the bottom and top of the equivalent cylinder respectively and ΔT which is the degree of nonlinearity. Assuming an axial height of "h", then the quadratic form for axial gradients becomes

$$T(z) = T_B + \frac{z}{h}(T_T - T_B) + 4\left(\frac{z}{h} - \frac{z^2}{h^2}\right)\Delta T \qquad \text{(all r)}$$

When the temperature of the bottom and top are the same, the second term in the above formula disappears.

The complete array of cases considered in the equivalent cylinder analyses for both radial and axial gradients are listed in Table 5.

The reason that quadratic nonlinear temperature gradients are considered is that for a free body, as previously discussed, a uniform or linear temperature gradient produces zero stresses within the context of linear thermal stress analysis (i.e., when the mechanical properties are constant and not functions of temperature). Since the whole temperature range considered for each case was at maximum only at 3.3 percent change, the temperature dependent properties could be considered effectively constant in this range. In the actual analyses, they were considered temperature dependent, but still the degree of thermal stresses produced by this dependence was small as compared to the thermal stresses produced by the nonlinear portion of the temperature gradients.

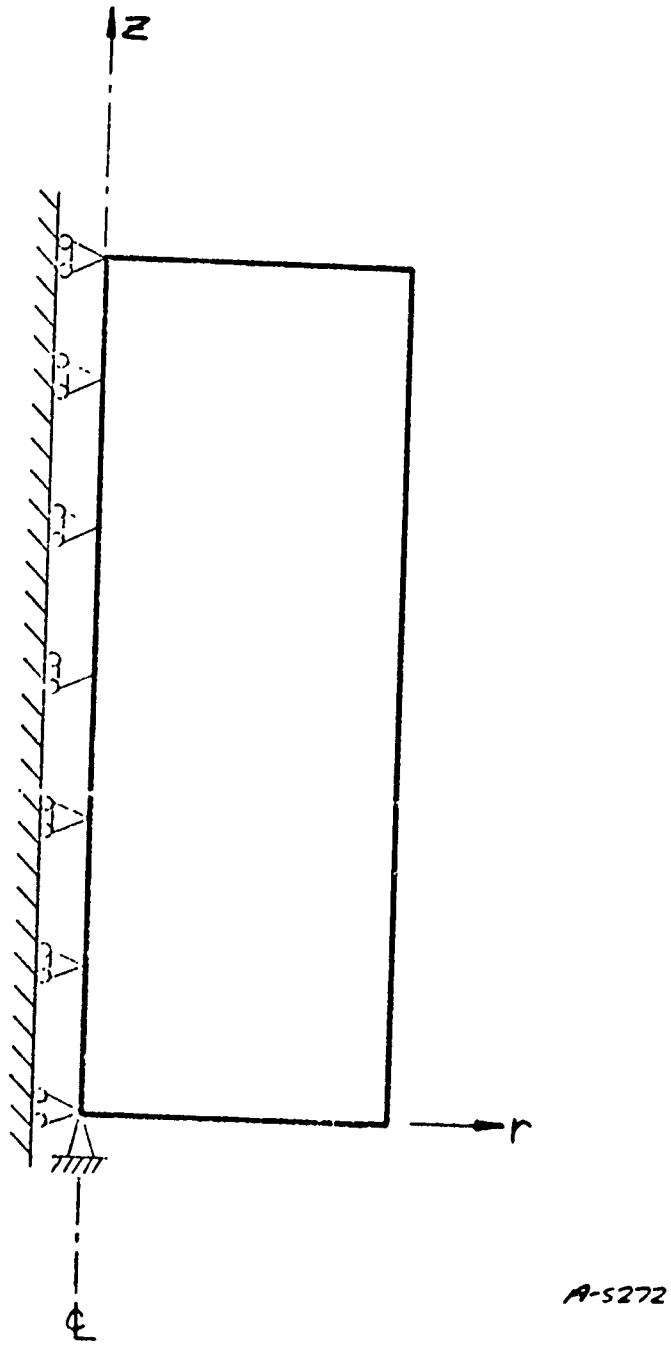

FIGURE 15 BOUNDARY CONDITIONS OF EQUIVALENT CYLINDER MODEL

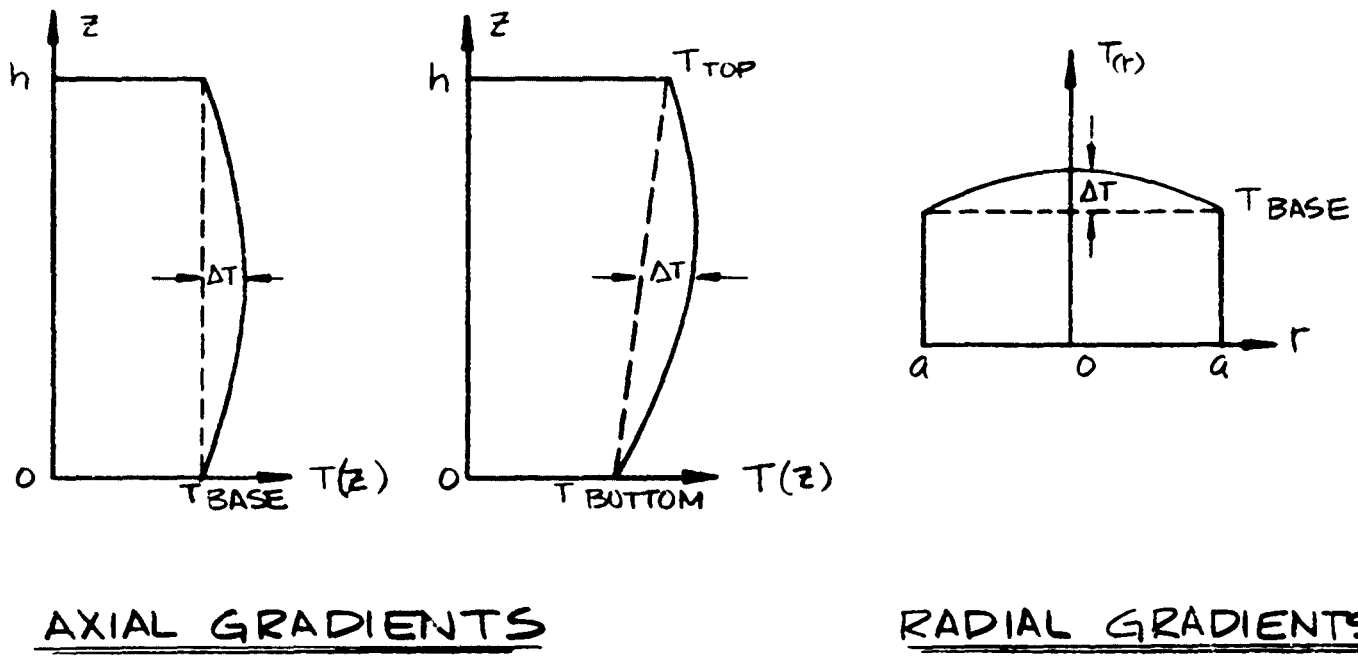

A-5273

FIGURE 16 HYPOTHETICAL NONLINEAR TEMPERATURE GRADIENTS

The stress distributions produced by nonlinear temperature distributions were calculated but not plotted. The finite element model is graphically illustrated in Figure 17. The results of these stress analyses are summarized for the maximum tensile values existing throughout the brick in Table 5. There are three principal stress components listed in Table 5. They are σ_r (radial stress), σ_θ (hoop stress) and σ_z (axial stress). The location within the brick where the maximum tensile values of these three stresses occur is shown in Figure 17 for radial and axial temperature distributions. All three stresses are listed for both locations. The direction of these three principal stresses is also shown in Figure 17 on a typical small element. The degree of nonlinear temperature distribution, ΔT, is listed in Table 5, where its meaning was fully explained earlier.

When examining the results for radial nonlinear temperature distributions, one notices that the maximum stresses occur on the outside surface of the brick, midway between the top and bottom. Here, a biaxial stress field exists where $\sigma_z^{max} \approx \sigma_\theta^{max}$. Since the elastic modulus E, coefficient of linear thermal expansion α and the ΔT are known, then the principal stresses may be expressed by

$$\boxed{\sigma_i = \beta_i * \frac{E \ \alpha \ \Delta T}{(1 - \nu)}} \qquad i = r, \theta, z$$

where β_i is a numerical factor depending upon the radial temperature distribution. Using the results of Table 5, we find for the principal stresses σ_r, σ_θ, σ_z for the temperatures T = 2000, 3000°F the following β-factors:

TABLE 6

ΔT (RADIAL) β-FACTORS

		Center of Ends			Midway Along Outside		
Length	Temp	β_r^E	β_z^E	β_θ^E	β_r^S	β_z^S	β_θ^S
6"	2000	.1287	-.0172	.1287	-.0265	.4943	.5186
	3000	.1211	-.0162	.1211	-.0251	.4680	.4913

To compare these numerical results for a 6-inch brick with a closed form analytical solution, we select a solution for an infinite long cylinder having

TABLE 5

STRESSES ASSOCIATED WITH
NONLINEAR RADIAL AND AXIAL TEMPERATURE GRADIENTS

Type of ΔT	Brick Length	ΔT	T_{Base} or T_{bottom}/T_{top}	Center of Ends			Midway Along Outside		
				σ_r	σ_z	σ_θ	σ_r	σ_z	σ_θ
RADIAL	6"	20	2000	306.9	-41.0	306.9	-62.9	1172.3	1229.0
		40	2000	610.3	-81.7	610.3	-125.8	2343.5	2458.5
		60	2000	910.0	-22.1	910.0	-188.7	3513.4	3688.7
		20	3000	196.1	-26.2	196.1	-40.3	751.3	788.0
		40	3000	387.9	-51.8	387.9	-80.6	1499.1	1574.1
		60	3000	575.4	-77.0	575.4	-120.7	2243.3	2358.3
AXIAL	6"	20	2000	162.3	-7.2	162.3	-7.5	211.7	62.7
		40	2000	323.4	-14.4	323.4	-14.9	421.6	124.9
		60	2000	483.3	-21.5	483.3	-22.2	629.5	186.6
		0	2000/2100	20.9	.2	18.5	0	-2.3	-.8
		20	2000/2100	178.5	-5.9	177.4	-7.3	207.1	61.4
		40	2000/2100	335.0	-11.9	335.2	-14.7	414.7	122.9
		60	2000/2100	490.3	-17.9	491.8	-21.9	620.3	183.8
		20	3000	104.1	-4.6	104.1	-4.8	135.2	40.1
		40	3000	207.3	-9.2	207.3	-9.4	267.6	79.4
		60	3000	309.6	-13.7	309.6	-14.0	397.3	118.0
		0	3000/3100	13.7	.1	12.4	0	-.8	-.3
		20	3000/3100	115.2	-3.8	114.5	-4.7	130.9	38.7
		40	3000/3100	215.6	-7.7	215.8	-9.2	259.8	77.0
		60	3000/3100	315.1	-11.5	316.0	-13.7	385.9	114.5
	4"	20	2000	356.9	-15.2	356.9	-16.2	447.2	114.7
		40	2000	711.7	-30.3	711.7	-32.2	890.6	228.5
		60	2000	1064.4	-45.4	1064.4	-48.1	1330.2	341.3
	2"	20	2000	1035.6	-33.9	1035.6	-49.3	816.4	20.7
		40	2000	2068.1	-67.9	2068.1	-98.1	1627.4	41.6
		60	2000	3097.4	-101.8	3097.4	-146.5	2432.5	62.6

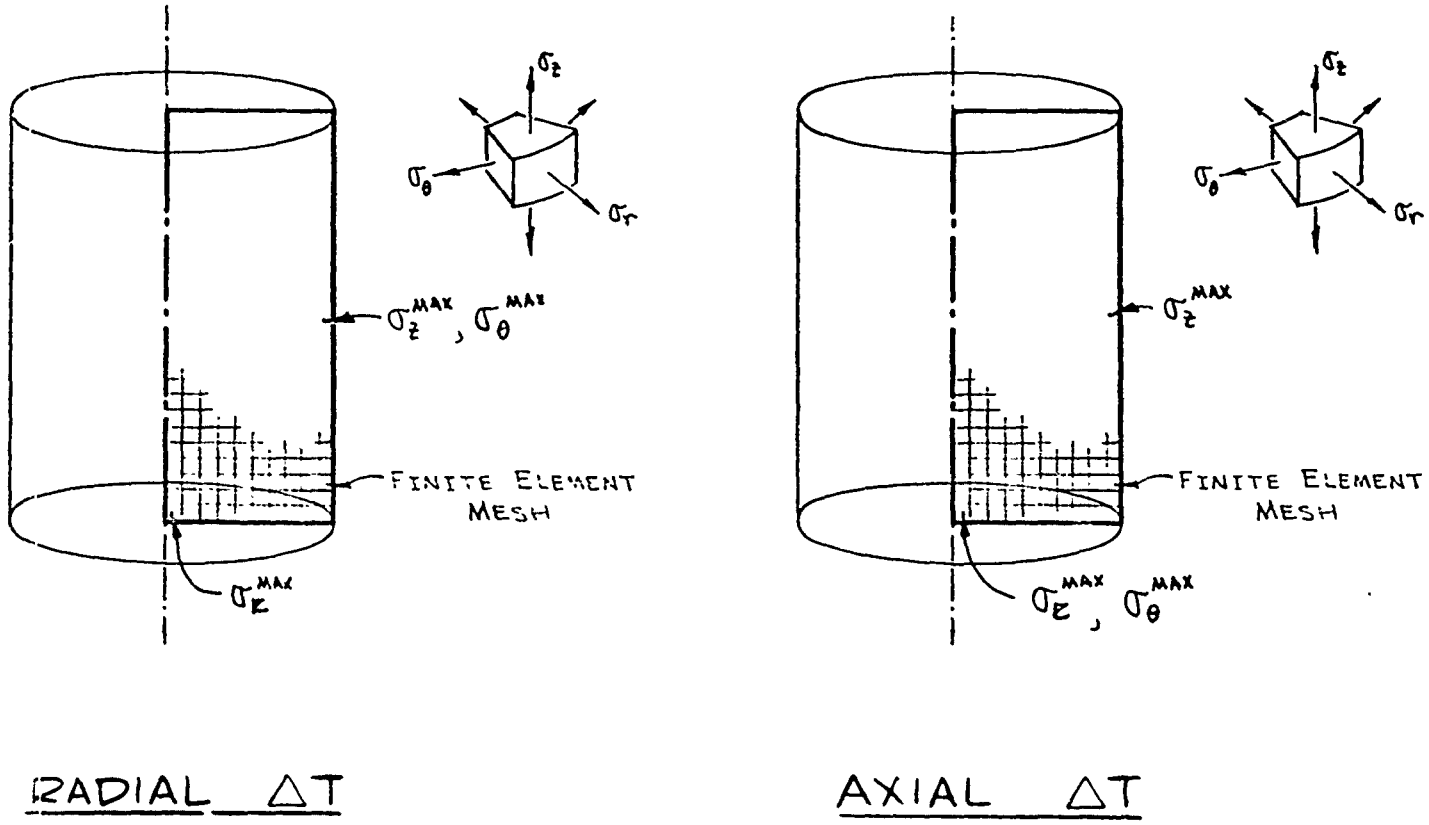

A-5274

FIGURE 17 LOCATIONS OF MAXIMUM TENSILE STRESS IN EQUIVALENT CYLINDER BRICK MODEL

a radial temperature distribution. Jsing this together with the previously defined temperature distribution, T(r), we find that at r = a, the maximum stresses are in the form presented above with the numerical factors β being

$$\beta_r = 0.0$$

$$\beta_\theta = 0.5$$

$$\beta_z = 2\nu = 0.6 \quad (\nu = 0.3)$$

These analytical results are very close to the β_i^S numerical results except that since only a 6-inch brick was used, the numerical β_z^S is slightly low. This comparison was made midway along the outside location where σ_θ and σ_z are maximum (the superscript S on the β - factors indicates this location).

When examining the axial nonlinear temperature distributions, the following table of β-factors result.

TABLE 7

ΔT (AXIAL) β-FACTORS

		Center of Ends			Midway Along Outside		
Length	Temp	β_r^E	β_z^E	β_θ^E	β_r^S	β_z^S	β_θ^S
6"	2000	.0682	-.0030	.0682	-.0031	.0889	.0264
	2000/2100	.0727	-.0025	.0726	-.0031	.0886	.0263
	3000	.0647	-.0029	.0647	-.0029	.0835	.0248
	3000/3100	.0702	-.0025	.0702	-.0030	.0833	.0247
4"	2000	.1501	-.0064	.1501	-.0068	.1878	0.482
2"	2000	.4362	-.0143	.4362	-.0207	.3432	.0088

No simple analytical solution was found in the literature for nonlinear axial temperature distributions in finite length cylinders, and consequently no comparison is made. One interesting fact resulting from this set of stress analyses is illustrated in Figure 18. Here, the β-factors for both the radial and axial nonlinear temperature distributions are shown plotted versus the length of the "equivalent cylinder" brick. As the length of the brick decrease, the axial β-factors (and therefore the stresses) increase, going to infinity as the length goes to zero. This is as expected, since the ΔT was held constant (in the actual stress analyses) as the length was shortened. This in effect

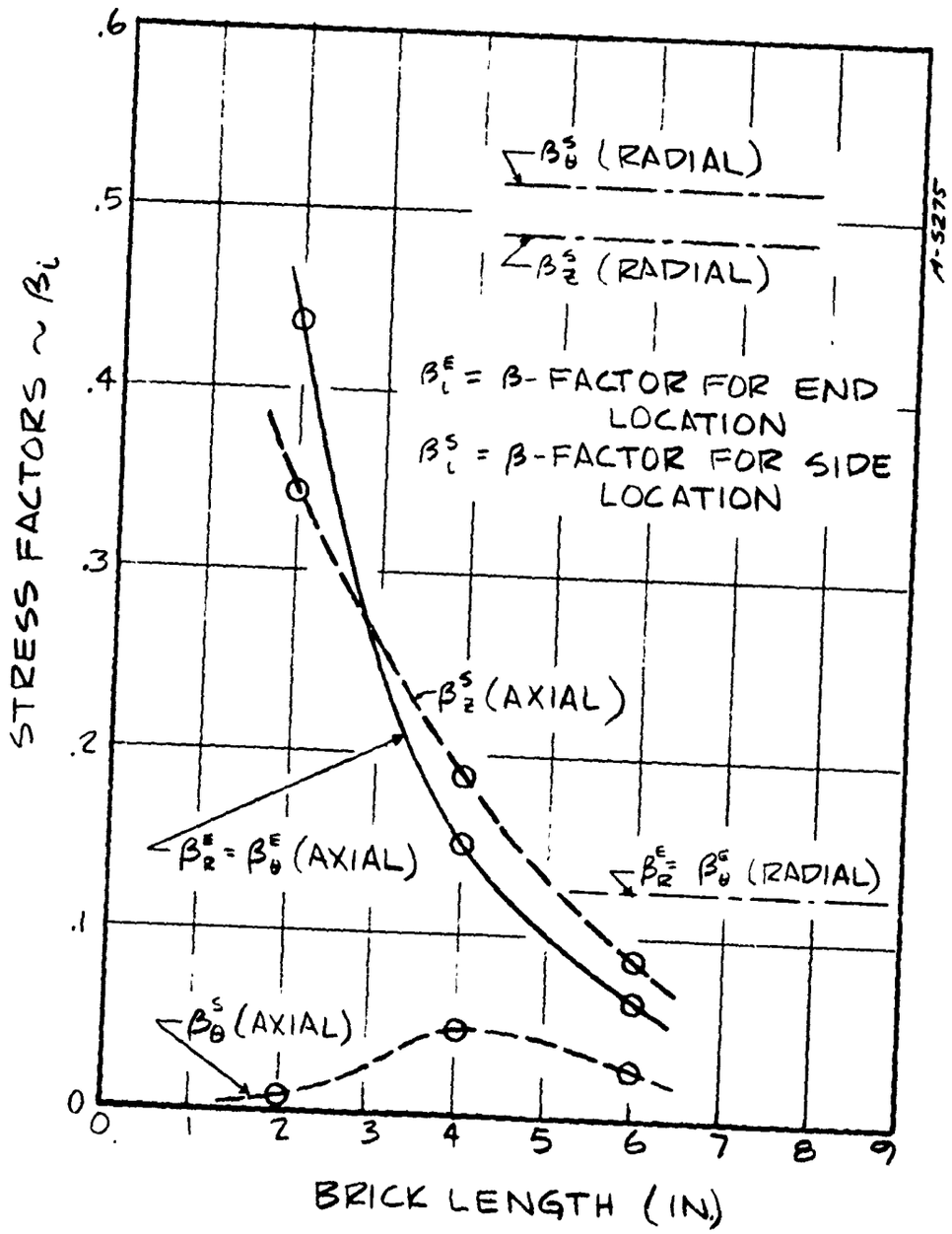

FIGURE 18 STRESS β-FACTORS VERSUS LENGTH OF BRICKS

concentrates the nonlinearity into a short length, becoming more pronounced as the length becomes smaller and smaller A similar effect would also be expected in the radial β-factors if the radius was decreased while holding the ΔT constant.

These results indicate that nonlinear temperature distributions within the bricks can produce significant tensile stresses. These stresses are considered in relation to other stresses and brick strength in Section 3.3.4

3.3.3 Point Contact Loading Stress Analysis

Another type of loading condition which could give rise to stresses in the bricks is non-thermal in nature. This is concentrated loading conditions which could exist due to the bricks transmitting loads from one to another at regions of small area instead of over whole load transfer areas. One such example is the dead weight loading of bricks stacked on top of one another. If the ends of the bricks are not perfectly flat, then this dead weight loading will be transferred at points rather than across the whole end surface area. This is shown graphically in Figure 19 where one end of a brick in a column is bowed, thereby causing the dead weight of all the bricks in the column to be transferred through the small contact area which here is the outer perimeter of the brick.

Again, the equivalent cylinder model described above was used to investigate this loading condition. The model and boundary conditions were the same as that shown in Figure 15 with the exception that the axial constraint at the center line was replaced by a roller condition on the outside bottom circumference which allowed radial movement but no axial movement. The dead weight loading of twelve feet of bricks (normal pressure of 28.9 psi) was applied as a normal pressure along the top surface of the equivalent cylinder model of the brick. Force equilibrium then produced a concentrated line load along the outside bottom circumference where the axial roller boundary condition was imposed, thereby simulating this point contact load transfer condition.

The equivalent cylinder model described here was analyzed for this mechanical line loading condition. The finite element model, boundary conditions (for line-contact loading) and loading conditions are shown in Figure 20a. The load was considered as the dead weight of a twelve foot column of bricks acting uniformly over the top of the six inch brick model. The reacting load was considered a line-contact load existing (axially) on the outside perimeter as shown by the support condition in Figure 20a. The temperature of the brick was shown by the support condition in Figure 20a. The temperature of the brick was assumed uniform at T = 3000°F. The stress results are shown by isostress contour plots in Figures 20b through 20f. In addition, areas of tensile and compressive loading conditions are indicated on these figures.

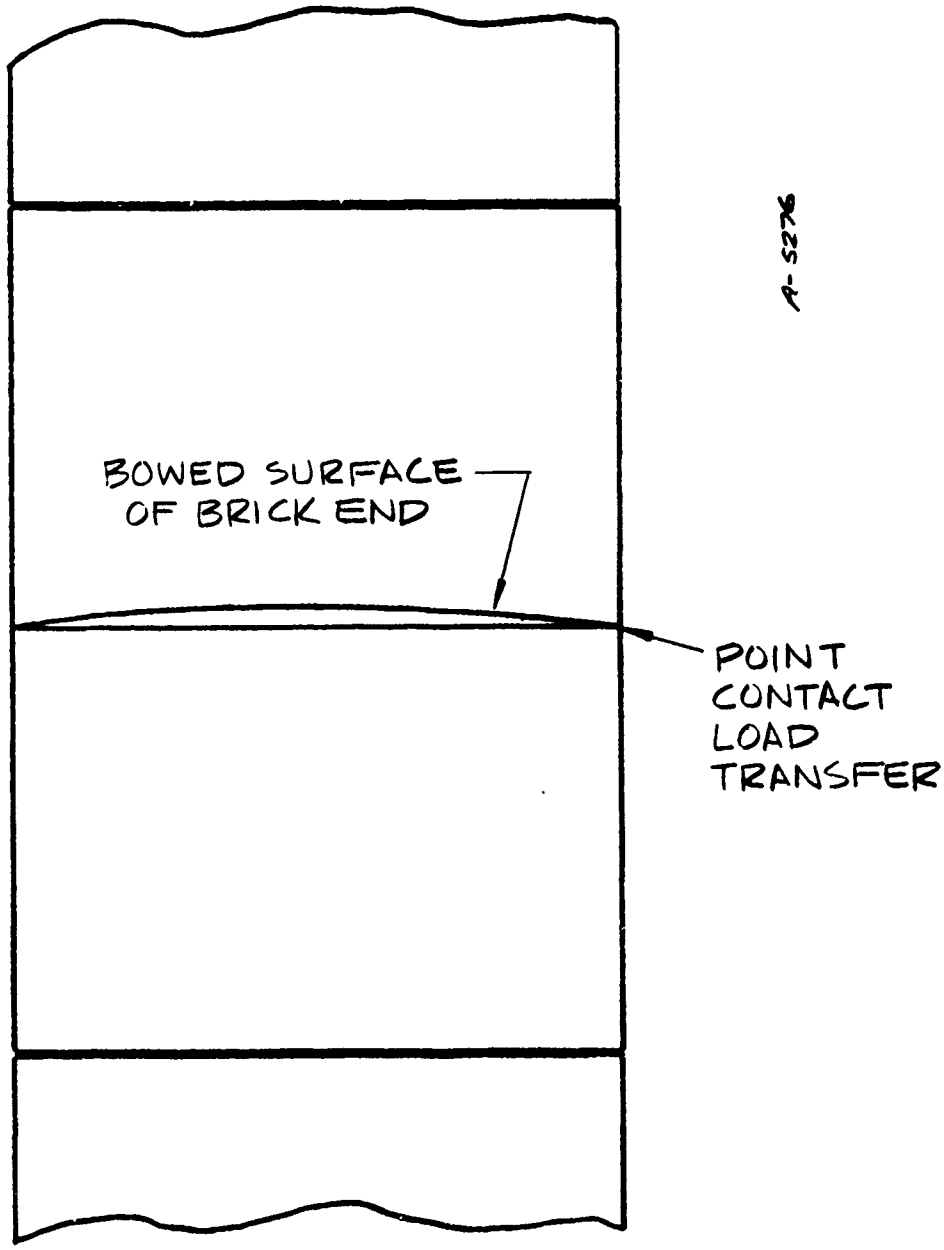

FIGURE 19 ILLUSTRATION OF COLUMN OF BRICKS WITH POINT CONTACT LOAD

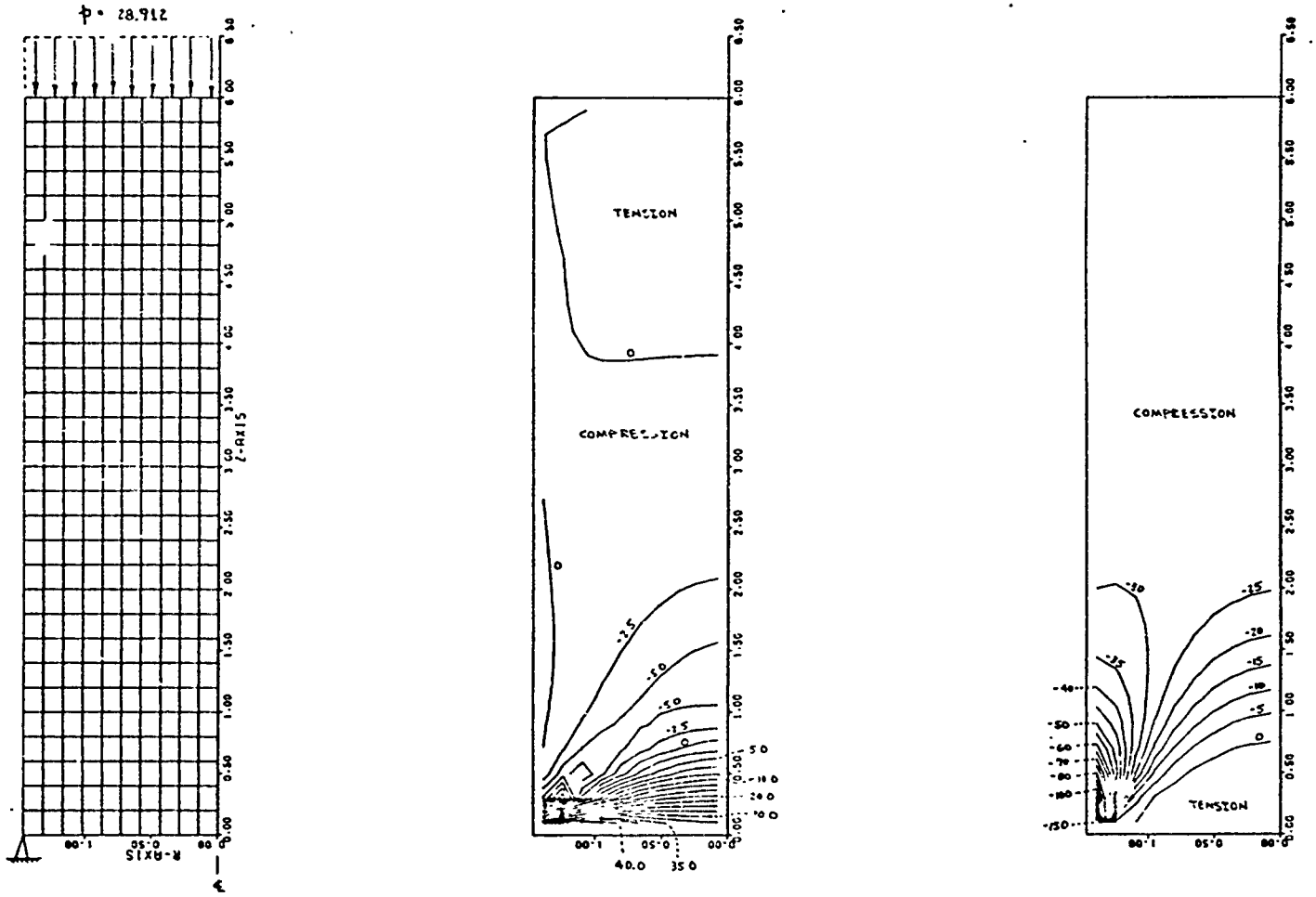

A) FINITE ELEMENT MODEL

B) STRESS, σ_R

C) STRESS, σ_Z

A-5277

FIGURE 20 RESULTS OF BRICK POINT CONTACT STRESS ANALYSIS

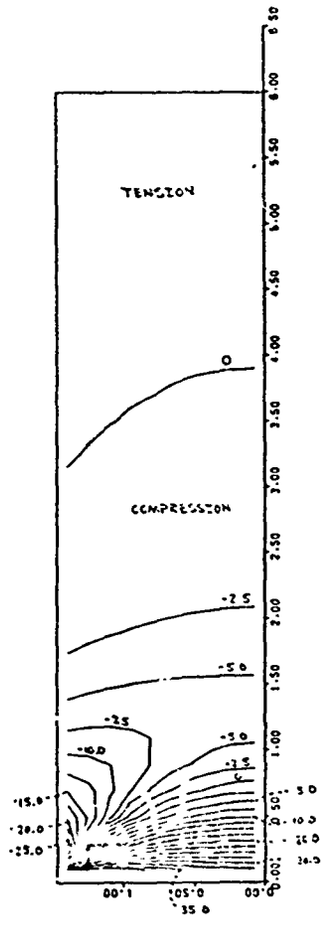

D) STRESS, σ_θ

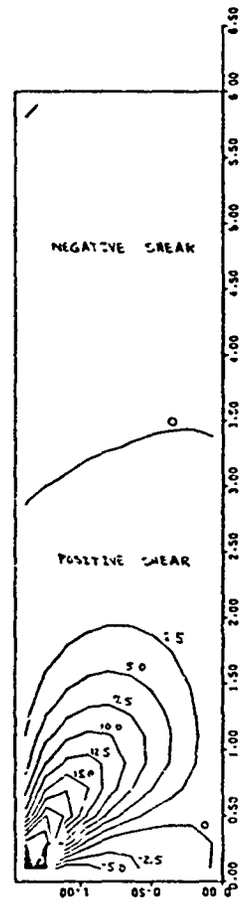

E) STRESS, τ_{RZ}

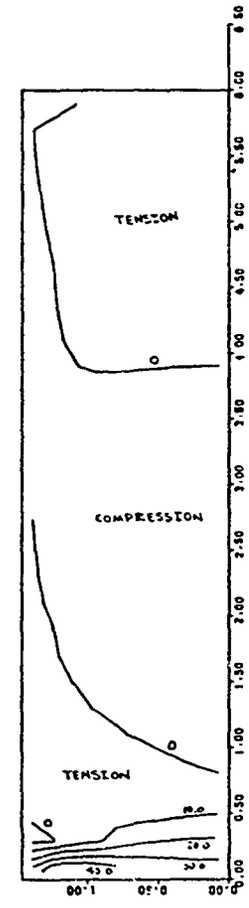

F) STRESS, σ_{MAX}

A-5278

FIGURE 20 (CONCLUDED)

These stress results indicate that for this type of loading condition, maximum tensile stresses on the order of 40 - 50 psi are developed near the area of the line-contact load. This may be seen in the radial stress σ_r plot (Figure 20b), hoop stress σ_θ plot (Figure 20d) and maximum stress plot (Figure 20f). The maximum axial stress σ_z (Figure 20c) developed occurs near the center line of the brick and is approximately 2 - 3 psi. In contrast, the maximum compressive σ_z is approximately 150 psi at the point of line-contact loading. The maximum shear stress τ_{max} developed is approximately 95 psi and also occurs at the point of contact loading.

In an overall sense, this line-contact loading condition does not produce any significant tensile stresses (only 40 - 50 psi) as compared to the in-plane thermal stresses or nonlinear temperature distribution thermal stresses. However, the stress patterns and magnitudes which it does produce can contribute to a critical condition in conjunction with the other modes of induced stresses within the bricks.

3.3.4 Combined Effect of Different Loadings

When examining the stresses produced by the three different sources of loading, none of these loading conditions produces sufficient high tensile stresses to cause fracture by itself. Since the material acts in an elastic-brittle manner, fracture is defined here as a tensile stress which equals or exceeds the yield (or ultimate) allowable stress shown in Figure 11a. When comparing predicted stresses to this ultimate stress, the combined effect of the various loadings discussed in previous sections should be considered. This can be done through superposition.

As an illustration of superposing two thermal stress loadings, consider the stresses produced by a nonlinear axial and radial temperature gradient. For the range of the ΔT's considered, the material properties may be considered effectively constant. Consequently, the principle of superposition may be used to combine a nonlinear radial temperature stress solution and a nonlinear axial temperature stress solution. This occurs since the governing equations in thermal elasticity theory are linear (when the material properties are constant). Now, the maximum axial stresses in the equivalent cylinder brick model shown in Figure 17 occurred on the outside surface midway along the brick for both a radial ΔT and an axial ΔT. For the radial ΔT loading, the maximum hoop stress also occurred at this location but not for the axial ΔT loading. The maximum hoop stress for the axial ΔT loading occurred at the top (or bottom) of the model at the axis of revolution of the model (Figure 17). However, tensile hoop stressed do exist at this midway, outside location and are given in Table 7 by

the β_θ^S - factor (as compared to the β_θ^E - factor). Interpolating from Table 7 for a temperature of T = 2872°F (the stress free reference temperature used in the in-plane solutions), we have for a six inch brick:

$$\beta_z^S = .0842$$

(Axial ΔT)

$$\beta_\theta^S = .0250$$

When comparing the β^S- factors in Table 7 for six inch bricks and four inch bricks, one notices that the four inch brick β^S- factors are approximately 2.15 times those for six inch bricks. Hence, assuming this generally holds true, the above β^S-factors for a four inch brick becomes:

$$\beta_z^S = 0.538$$

(Axial ΔT)

$$\beta_\theta^S = .1810$$

Interpolating from Table 6 for the radial ΔT β^S- factors at the temperature T = 2872°F yields:

$$\beta_z^S = .4900$$

(Radial ΔT)

$$\beta_\theta^S = .4760$$

Now, the total axial stress σ_z and hoop stress σ_θ at this outside, midway location due to both radial and axial ΔT's are given by:

$$\sigma_\theta = \frac{E\alpha}{(1-\nu)}\left[.1810\ \Delta T_{Axial} + .4760\ \Delta T_{Radial}\right]$$

$$\sigma_z = \frac{E\alpha}{(1-\nu)}\left[.0538\ \Delta T_{Axial} + .4900\ \Delta T_{Radial}\right]$$

Interpolating for the material properties E, α and ν from Figure 11 for a temperature of T = 2872°F yields:

$$E = 9.742\times10^6 \text{psi}$$

$$\alpha = 6.149\times10^{-6} \text{in/in°F}$$

$$\nu = 0.300$$

and therefore:

$$\frac{E\alpha}{(1-\nu)} = 85.88 \text{ psi/°F}$$

The formulas for the axial and hoop stresses now become:

$$\sigma_\theta = 4.604\ \Delta T_{Axial} + 40.74\ \Delta T_{Radial}$$

$$\sigma_z = 15.49\ \Delta T_{Axial} + 41.93\ \Delta T_{Radial}$$

These formulas represent the stresses induced in a four inch brick at T = 2872°F at the outside surface, midway in the axial direction of the brick, for a given ΔT_{Axial} and ΔT_{Radial}. For example, an axial ΔT = 148. °F and a radial ΔT = 75.°F would yield a hoop stress of σ_θ = 3737. psi and an axial stress of σ_z = 5438. psi.

Since the Zirconia is considered an elastic-brittle material, the Coulomb-Mohr failure criteria should be used to predict fracture conditions. In the present case where σ_θ and σ_z are both tensile (neglecting the radial component σ_R and the shear stress), this means that the maximum stress σ^* due to σ_θ and σ_z must reach the ultimate tensile stress condition σ_{Ult} to fracture, i.e.,

$$\sigma^* = \sigma_{Ult} \Rightarrow \text{Fracture.}$$

In a two dimensional stress plane (tensile quadrant), this fracture surface is represented by a circle as shown in Figure 21 (cf. Reference 18). For the two example tensile stresses σ_θ and σ_z given here, we have:

$$\sigma^* = \sqrt{\sigma_\theta^2 + \sigma_z^2} = 6598. \text{ psi}$$

The ultimate allowable stress at T = 2872°F is given by the uniaxial data presented in Figure 11a as σ_{Ult} = 8384. psi. Therefore, the maximum stress σ^* = 6598. psi produced by a ΔT_{Axial} = 148.°F and a ΔT_{Radial} = 75.°F would be 78.7% towards fracture.

This illustration of superposition only considered two sources of loading, namely a radial ΔT and an axial ΔT. To be complete, one should consider all sources of loading to determine maximum stress conditions. Therefore, the following sources should be considered:

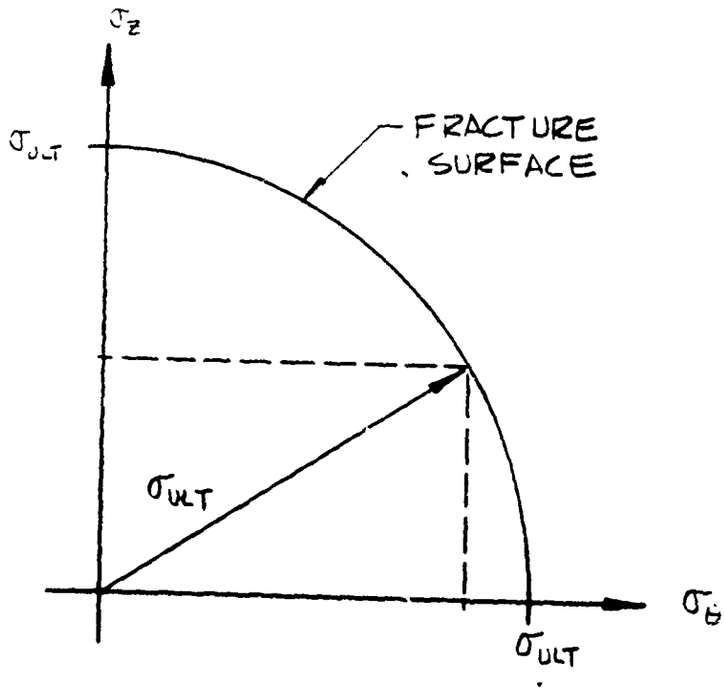

FIGURE 21 BIAXIAL FRACTURE SURFACE USED AS FAILURE CRITERIA FOR YSZ BRICKS

I. Body thermal stresses due to nonlinear axial temperature gradients.

II. Body thermal stresses due to nonlinear radial temperature gradients.

III. Web thermal stresses (in-plane solutions).

IV. Body stresses due to hydrostatic pressure of p = 3000 psi acting on the whole bed.

V. Local stresses due to point or line contact loading conditions.

VI. Other sources of stresses such as local hot spots, residual stresses from fabrication, etc. which will be described subsequently.

The last two sources of stresses will be ignored for the present and only the first four will be considered.

For the example described above (i.e., due to sources I and II), the tensile thermal stresses due to III and the compressive stresses due to IV should also be considered. From the in-plane web thermal stress solutions described earlier, the most severe case of web thermal stresses due to blowdown was the plane strain ($\varepsilon_z = 0$) solution, i.e., Case III. From Table 4, the maximum axial and hoop stresses of Case III existed at the same location and were:

$$(\sigma_{max})_{hole} = 4346 \text{ psi}$$

$$(\sigma_z)_{hole} = 4229 \text{ psi}$$

where $(\sigma_{max})_{hole}$ was the maximum hoop stress existing at the hole surface and $(\sigma_z)_{hole}$ was the "normal" or axial stress from this in-plane solution. The $(\sigma_{max})_{hole}$ stresses exist in the plane and so would be additive to the σ_θ stresses of the equivalent cylinder solution. The $(\sigma_z)_{hole}$ stress is in the axial direction of the brick (normal to the plane) and therefore additive to the σ_z stress of the equivalent cylinder solution. The stresses due to IV are compressive, being the same in all directions, and therefore:

$$\sigma_\theta = -3000 \text{ psi}$$

$$\sigma_z = -3000 \text{ psi}$$

Now, when the four sources of stress, i.e., I, II, III and IV listed above are combined, the resultant tensile stresses become:

$$\sigma_\theta = 3737. + 4346. - 3000. = 5083. \text{ psi}$$

$$\sigma_z = 5438. + 4229. - 3000. = 6667. \text{ psi}$$

and the resultant maximum stress σ^* is:

$$\sigma^* = \sqrt{\sigma_\theta^2 + \sigma_z^2} = 8384. \text{ psi}$$

which is just the fracture stress σ_{Ult} for T = 2872.°F. Therefore, when considering the first four sources listed above, with a ΔT_{Axial} = 148.06 and a ΔT_{Radial} = 75.0, the resultant maximum tensile stress is just sufficient to fracture the brick on the outside surface, midway along the axial direction of the brick. It is also possible to have other combinations of ΔT_{Axial} and ΔT_{Radial} combining together with the stresses from sources III and IV to yield a maximum stress which equals the ultimate stress σ_{Ult} = 8384. psi for this temperature of T = 2872.°F

The formulas for the σ_θ and σ_z are given by

$$\sigma_\theta = 4.604\ \Delta T_{Axial} + 40.74\ \Delta T_{Radial} + 4346. - 3000.$$

$$\sigma_z = 15.49\ \Delta T_{Axial} + 41.93\ \Delta T_{Radial} + 4229. - 3000.$$

and the fracture condition is given by

$$\sigma^* = \sqrt{\sigma_\theta^2 + \sigma_z^2} = \sigma_{Ult} = 8384. \text{ psi.}$$

These three equations define an interaction curve between ΔT_{Axial} and ΔT_{Radial} which will yield a fracture condition. This interaction curve is shown plotted in Figure 22. The values of ΔT_{Axial} and ΔT_{Radial} used in the example given previously are shown by dashed lines in Figure 22.

The reason that the stresses due to source V were not included is that the contact line loading solution indicated that the maximum tensile stresses developed were only 40 - 50 psi, and were in the region near the end of the brick instead of near the middle. However, this does not mean that a point contact loading condition near the middle of the brick (axially speaking) would not contribute, but high compressive stresses in the direction of the point (or line) contact load accompany the relatively small tensile stresses developed and so this source of tensile stresses was neglected as a major contributor to a condition which would produce a fracture.

The stresses listed in source VI will be discussed in the next section.

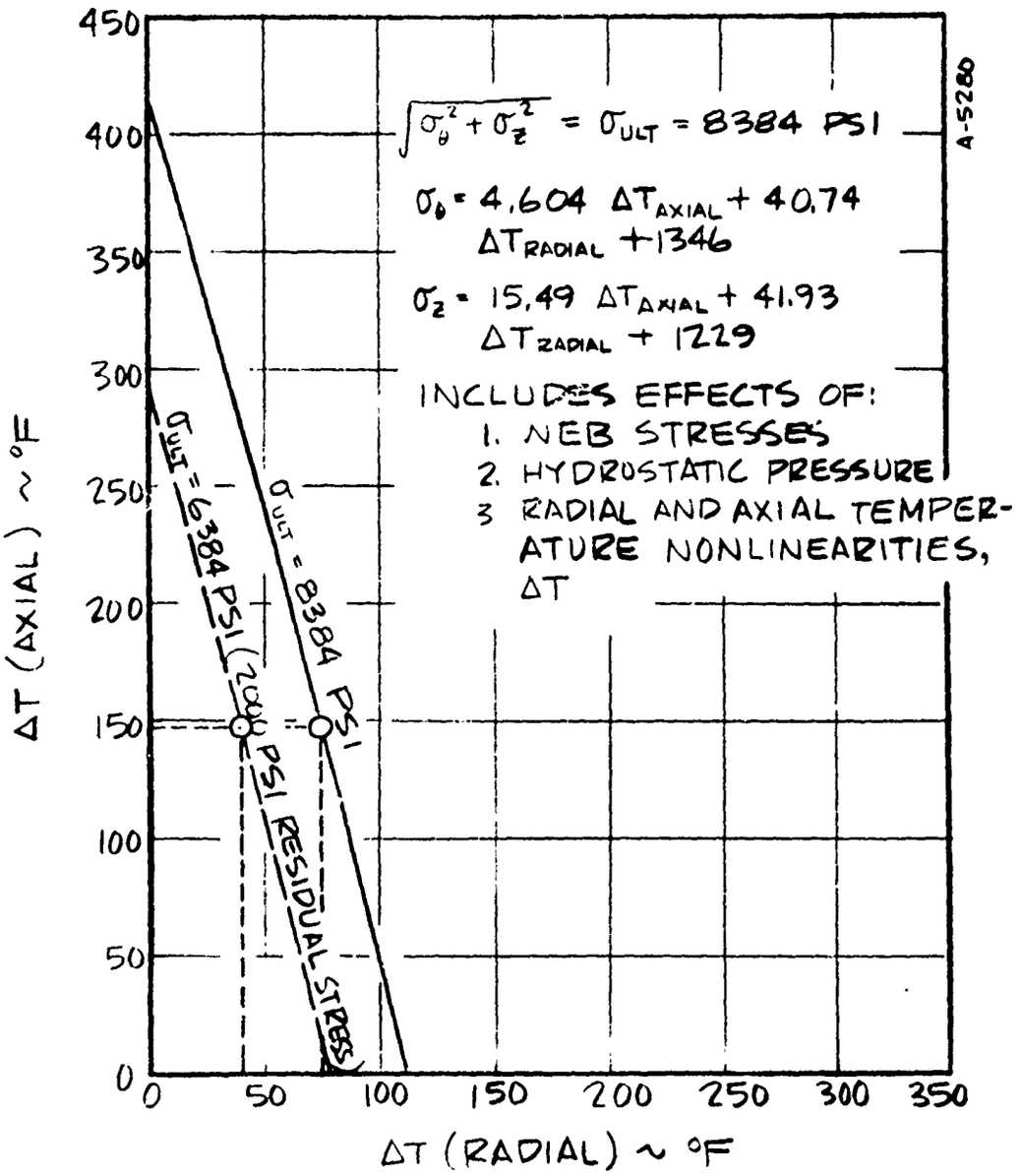

FIGURE 22 INTERACTION CURVE FOR FRACTURE STRESS CONDITION IN 4 IN YSZ BRICK AT T = 2872 °F

3.3.5 Other Stress-Affecting Phenomena

The analyses described in Sections 3.3.1 through 3.3.4 considered only deterministic phenomena which lent themselves to analytical investigation. Other stress-affecting phenomena exist within the bricks which cannot be treated analytically, at least in an economical manner. These other phenomena are stress conditions arising from (a) built in residual stresses, (b) local hot spots, (c) partial destabilization of the zirconia, (d) micro-cracks existing in bricks and other "real world" effects which are usually not considered in analytical predictions. Some of these phenomena are always present in structural components but are often not important since the materials are ductile, and allow local stress rising conditions to be relieved. However, in ceramic materials like yittria stabilized zirconia (YSZ), the material is elastic brittle, and does not possess any ductile behavior. Stress rising conditions will not be relieved, and will be the mechanisms which initiate fracture. In this section, some of these other stress rising phenomena are discussed in a qualitative fashion.

Residual stresses occur during the ceramic brick fabrication process. The powder is pressed (isostatically) into a green body and then fired. During cool-down, it is possible that a small amount (i.e., 1 percent or less) of YSZ is not fully stabilized and thus around 2000°F, the structure changes from cubic to monoclinic which is accompanied by a 7-10 percent volume change of the material. This creates high local stresses which remain as residual stresses when the brick eventually cools down to room temperature. Another source of residual stresses is due to the presence of glass in the grain boundaries of the YSZ solid solution. Again, during cool down, the viscous nature of this glass will allow stresses to redistribute internally and eventually to result in locked in residual stresses at room temperature. These residual stresses can be quite large and tend to accelerate the possibility of fracture occurring during operation of the bricks in the heater bed.

Locally severe thermal stresses would be associated with any localized but significant perturbations in the brick matrix temperature field. Such local hot spots (or cold spots) could arise from a variety of causes, most of which would be associated with design or fabrication imperfections. For example, local increases in the convective heat transfer coefficient due to hole misalignments at the brick interfaces (as considered as part of Appendix B) would result in a local cold spot during blowdown. Similarly, irregularities at the interface between the outer boundary of the brick matrix and the heater vessel interior insulation could give rise to stress affecting local temperature variations.

Partial destabilization of YSZ could possibly occur when it passes through the temperature range of 1900-2000°F. This causes an increase in the monoclinic structure (as compared to the stabilized cubic structure) which has an accompanying volume change (c.f., Ref. 3). As described above, this local volume change gives rise to quite large internal stresses which, like residual stresses, can be quite large.

Micro-cracks can exist in the bricks due to the fabrication process. As explained above, the mixture of yttria and zirconia may not be completely homogeneous. Consequently, during fabrication, local concentrations of unstabilized zirconia will experience a phase change, accompanied by the volume change, and therefore create local stresses which may be high enough to create local cracks in the material. This phenomenon is slightly different than the residual stress phenomenon since it occurs on a microscopic scale rather than a macroscopic scale (residual stresses). In addition, other phenomena also cause micro-cracks to occur in the fabricated bricks. The result of these micro-cracks is that they act as fracture triggering mechanisms, allowing macro-cracks to initiate and run through the material, thereby producing a fracture condition.

All of the above listed phenomena, plus others not listed here, have the general tendency to aggravate the stress conditions which will eventually lead to fracture of the bricks. Assuming for the moment that all of these other sources give rise to a tensile pre-stress of 2000 psi, then for the example of combined stresses shown in Figure 22, the ultimate stress needed for fracture would only be 6384 psi (as compared to 8384 psi) and the interaction curve would be lowered as shown by the long dashed line in Figure 22. Now, an axial $\Delta T = 150°F$ and a radial $\Delta T = 40°F$ would suffice to cause fracture, as indicated by the short dashed line in the figure. This example simply illustrates that these other stress affecting phenomena tend to give rise to stresses which can be quite large. When they are considered in conjunction with the sources analytically treated in this report, it is easily demonstrated that certain combinations of all these sources can lead to fracture conditions within the bricks.

SECTION 4

CONCLUSIONS

1. Relatively precise calculation of web stresses was performed. For the conditions considered, the maximum predicted tensile stress was about 4000 psi. Recent measurements indicate that the ultimate strength of yttria stabilized zirconia is about 8000 psi at this condition. It is concluded that, for these conditions, brick fracture is highly unlikely due to web stresses alone, particularly when the effect of the heater hydrostatic pressure is considered.

2. Brick normal stresses due to temperature distribution nonlinearities in the radial and axial directions were computed. The results were correlated in terms of the relation

$$\sigma_i = \beta_i \frac{E \alpha \Delta T}{(1 - \nu)} \quad i = r, \theta, Z$$

where the β_i factors were defined for a variety of conditions. The actual magnitudes of temperature nonlinearities across the bricks are unknown, so these results can only be interpreted in a parametric fashion. However, an approximate thermal analysis (Appendix B) indicates that radial temperature nonlinearities of the order 100°R are possible for bricks with misaligned holes. This results in maximum tensile stresses more than half the ultimate strength.

3. It is unlikely that point contact loading of the bricks will contribute significantly to brick stresses.

4. The principal of superposition was employed to assess the net effect on brick stresses of combined thermal and mechanical loading. Again, the magnitudes of brick net temperature distribution nonlinearities are the major unknown. An approximate interaction curve was constructed which considers combined loading and gives the fracture conditions in terms of required radial and axial temperature nonlinearities. Limitations on the use of this curve are discussed in Appendix C.

5. The brick stresses and fracture conditions will also be affected by phenomena which are not amenable to theoretical quantitative analysis. These include residual stresses, incomplete stabilization or destabilization, microcracks, and local hot spots.

6. Uncertainties relative to the magnitudes of brick temperature distribution nonlinearities and the factors listed in Item 5 above preclude quantitative specification of heater operation modifications or cored brick design revisions based on the results of this study.

REFERENCES

1. Hendrick, W. S., et al., "Storage Heater Design Study for the Hypersonic True Temperature Tunnel," AEDC TDR-64-48, July 1964.

2. Harney, Major D. J., "Performance Analysis of Large Ceramic Storage Heaters," AEDC TR-65-224, December 1965.

3. Hagford, D. E., DeCoursin, D. G., "Research on Storage Heaters for High Temperature Wind Tunnels - Final Report," AEDC TR-71-258, February 1972.

4. Moyer, C. B., Davis, J. N., "Program for Analysis of Null Point Calorimeter Data, Version 2 (PANDA 2) Description and Users Manual," Aerotherm Report UM-72-29, April 1972.

5. Kreith, F., Principles of Heat Transfer, Second Ed., Int. Texbook Co., July 1968, Chapter 8.

6. Schneider, P. J., Temperature Response Charts, John Wiley and Sons, Chart 36(c), 1963.

7. Jacob, M., Heat Transfer, Vol. II, John Wiley and Sons, 1957, Chapter 35.

8. Moyer, C. B., "Axi-Symmetric Transient Heating and Material Ablation Program (ASTHMA) Description and User's Manual," Aerotherm Corporation, Mountain View, California, Aerotherm Report No. 68-27, January, 1968.

9. Engelhe, W., Personal Communication, Southern Research Institute, Birmingham, Alabama, July 1971.

10. Southern Research Institute, "The Thermal Properties of an Yttria Stabilized Zirconia," Birmingham, Alabama, January 1972.

11. Fahrenbacher, Major L. R., Personal Communications, ARL, Wright Patterson Air Force Base, Ohio, July 1971.

12. Southern Research Institute, "Preliminary Mechanical Property Data, Yttria Stabilized Zirconica," Birmingham, Alabama, October 1971.

13. Weiler, F. C., "DOASIS Code User's Manual," Weiler Research, Inc. Report No. 1, 1971.

14. Zienkiewicz, O. C., The Finite Element Method in Engineering Science, McGraw Hill, London, 1971.

15. Przemieniecki, J. S., Theory of Matrix Structural Analysis, McGraw Hill, New York, 1968.

16. 16. Deleted

17. Fung, Y. C., Foundations of Solid Mechanics, Prentice-Hall, Inc. 1965, Chapter 14.

18. Babel, H., "Biaxial Fracture Strength of Brittle Materials," AFML-TR-66-51, Air Force Materials Laboratory, Wright Patterson Air Force Base, Ohio, May 1966.

APPENDIX A

IMPLICIT ONE-DIMENSIONAL FINITE DIFFERENCE CONDUCTION SOLUTION

by

C. B. Moyer

T. C. Derbidge

LIST OF SYMBOLS

A_i	nodal area, node i
a_i	constant in Eq. (A-6), defined by Eq. (A-7)
b_i	constant in Eq. (A-6), defined by Eq. (A-8)
b_i^*	value of b_i modified by recursion relation (A-15)
c_i	constant in Eq. (A-6), defined by Eq. (A-9)
C_p	specific heat
d_i	constant in Eq. (A-6), defined by Eq. (A-10)
d_i^*	value of d_i modified by recursion relation (A-15)
k	thermal conductivity
ℓ_i	nodal thickness, node i
NL	denotes last node
q_{cond}	heat conducted into body away from heated surface
r	radial distance from the center of the cylinder
T	temperature
T_a	initial temperature
T_o, T_w	surface temperature
u	thermal conductance defined by Eqs. (A-11), (A-12), (A-13)
α	constant in Eq. (A-18) defined by Eq. (A-19)
β	constant in Eq. (A-18) defined by Eq. (A-20)
$\Delta\theta$	finite difference time step
θ	time
ρ	density
τ	nodal time constant, Eqs. (A-23), (A-24)

LIST OF SYMBOLS (Concluded)

Subscripts

i	denotes node i

Superscripts

n	denotes at time step n

APPENDIX A

IMPLICIT ONE-DIMENSIONAL FINITE DIFFERENCE CONDUCTION SOLUTION

The solution of the transient heat conduction problem for a variable-property, one-dimensional circular cylinder is described.

The solution uses a simple implicit finite difference approach. The differential equation for $T(r,\theta)$ is

$$\frac{\partial}{\partial r}\left(kA\,\frac{\partial T}{\partial r}\right) = \rho C_p A\,\frac{\partial T}{\partial \theta} \tag{A-1}$$

with the boundary conditions

$$\left.\frac{\partial T}{\partial r}\right|_{r=r_o} = 0 \tag{A-2}$$

$$T\Big|_{r=r_i} = T_o(\theta) = T_w(\theta) \tag{A-3}$$

where $T_o(\theta)$ is to be determined from the system energy balance. The initial condition is

$$T(r,o) = T_a \tag{A-4}$$

where T_a is a constant.

In the difference approach, the cylinder is broken into a number of zones termed nodes, as shown in Figure A-1.

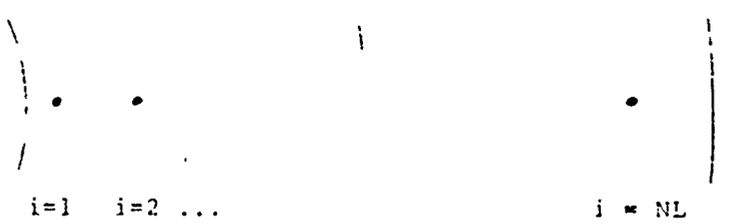

Figure A-1 Sketch of Nodal Grid

The temperature is defined at the center of each node and also at the heated surface. The difference analog of the differential equation (A-1) which results from taking a lumped parameter approach is, for each node except the first and last:

$$\frac{\left(T_i^{n+1} - T_i^n\right)}{\Delta\theta}\left(\rho C_{pi} A_i\right)\ell_i = \frac{T_{i-1}^{n+1} - T_i^{n+1}}{\dfrac{\ell_{i-1}}{2k_{i-1}A_{i-1}} + \dfrac{\ell_i}{2k_i A_i}} - \frac{T_i^{n+1} - T_{i+1}^{n+1}}{\dfrac{\ell_i}{2k_i A_i} + \dfrac{\ell_{i+1}}{2k_{i+1}A_{i+1}}} \tag{A-5}$$

Here T_i^n is the known (old)temperature of node i at time θ (time step n), and T_i^{n+1} is the unknown (new) temperature of node i at time $\theta + \Delta\theta$ (time step n + 1). For the last (i = NL) node, the last term in the right hand side is missing, since no heat flux leaves the insulated back wall. For the first node, the $\ell_{i-1}/2k_{i-1}A_{i-1}$ quantity is missing.

The solution procedure requires finding all the "new" nodal temperatures T_i^{n+1} at each time step. A new time step is selected, and the process repeated until the final time is reached. For solution purposes, Equation (A-5) is written as

$$a_i T_{i-1}^{n+1} + b_i T_i^{n+1} + c_i T_{i+1}^{n+1} = d_i \tag{A-6}$$

where

$$a_i = u_i \tag{A-7}$$

$$b_i = -u_i - u_{i+1} - \rho C_{pi}\ell_i A_i/\Delta\theta \qquad i = 2, \ldots NL \tag{A-8}$$

$$c_i = u_{i+1} \tag{A-9}$$

$$d_i = -T_i^n \rho C_{p_i} \ell_i A_i/\Delta\theta \qquad i = 2, \ldots NL \tag{A-10}$$

and

$$u_i = \frac{1}{\dfrac{\ell_{i-1}}{2k_{i-1}A_{i-1}} + \dfrac{\ell_i}{2k_i A_i}} \qquad i \neq 1,\ i \neq NL + 1 \tag{A-11}$$

$$u_1 = \frac{1}{\frac{1}{2k_1A_1}} \tag{A-12}$$

$$u_{NL+1} = 0 \tag{A-13}$$

The entire set of nodal equations (A-6) may be arranged as (dropping the superscript for temporary convenience).

$$\begin{aligned}
a_1T_0 + b_1T_1 + c_1T2 &= d_1 \\
a_2T_i + b_2T_2 + c_2T_3 &= d_2 \\
a_3T_2 + b_3T_3 + c_3T_4 &= d_3 \\
&\vdots \\
a_{NL-1}T_{NL-2} + b_{NL-1}T_{NL-1} + c_{NL-1}T_{NL} &= d_{NL-1} \\
a_{NL}T_{NL-1} + b_{NL}T_{NL} &= d_{NL}
\end{aligned} \tag{A-14}$$

Since the last (lowest) equation has only two unknowns, it may be used to eliminate one unknown in the next to last equation, which in turn may be similarly used. Thus all the c_i terms may be wiped out of equations (A-14) in the first step of the familiar Gauss reduction; this results in modified b_i and d_i values according to the following recur.ion relations:

$$\begin{aligned}
b_i^* &= b_i - c_i \frac{a_{i+1}}{b_{i+1}} \qquad i = NL-1, NL-2, \ldots, 1 \\
d_i^* &= {}_i - c_i \frac{d_{i+1}}{b_{i+1}}
\end{aligned} \tag{A-15}$$

After this pass, the first equation then is

$$a_1 T_o + b_1^* T_1 = d_1^* \tag{A-16}$$

From an energy balance on the surface node q_{cond} is determined as

$$q_{cond} = u_1 \left(T_o^{n+1} - T_1^{n+1} \right) \tag{A-17}$$

Combining Equations (A-16) and (A-17) and eliminating T_1^{n+1}

$$q_{cond} = \alpha + \beta T_o^{n+1} \tag{A-18}$$

where

$$\alpha = - \frac{d_1^* u_1}{b_1^*} \tag{A-19}$$

$$\beta = u_1 \left(1 + \frac{a_1}{b_1^*} \right) \tag{A-20}$$

Equation (A-18) is utilized in the system energy balance as described in Section 2.1.1.1 to solve for T_o^{n+1}. With T_o^{n+1} thus determined, Equation (A-16) determines T_1. This in turn may be substituted into the second node equation to determine T_2 and so on down through the entire set of equations

$$T_i = \frac{d_i^* - a_i T_{i-1}}{b_i^*} \qquad i = 2, 3 \ldots NL-1 \tag{A-21}$$

$$T_{NL} = \frac{d_{NL} - a_{NL} T_{NL-1}}{b_{NL}} \tag{A-22}$$

Since the TACH solution procedure is implicit, there are no stability limits on the choice of time step. However, many users still prefer to scale the time step used on the natural stability limit of the nodal system. Therefore the program computes the natural time constant for all nodes at each time step

$$\tau_j = \frac{\rho C_{p_j} \ell_j A_j}{u_j + u_{j+1}} \qquad j = \text{node index} \tag{A-23}$$

and then seeks the maximum time constant

$$\tau_{max} = \max\ [\tau_j] \tag{A-24}$$

The time step selected is then τ_{max} if τ_{max} does not exceed the user input maximum time step or fall below the input minimum time step.

The time step can of course not exceed the time remaining to the next output time.

APPENDIX B

EFFECTS OF HOLE MISALIGNMENTS IN WIND TUNNEL HEATER CORE BRICKS ON PRESSURE DROP AND HEAT TRANSFER

by

M. D. Jackson
C. A. Powars

LIST OF SYMBOLS

A_1	smallest area associated with sudden expansion or sudden contraction (ft^2)
A_2	largest area associated with sudden expansion or sudden contraction (ft^2)
f	friction factor
G	mass flux (lbm/ft^2sec)
h	heat transfer coefficient ($Btu/hr\text{-}ft^2\text{-}°F$)
K	nondimensional head loss coefficient
$\dot{m}$	mass flow per hole (lbm/sec hole)
r	radius (ft)
R	gas constant

<u>Subscripts</u>

avg	average
cont	contraction
exp	expansion
fd	fully developed
max	maximum
x	axial distance

SECTION B.1

INTRODUCTION

This appendix summarizes the results of a brief study directed toward estimating the effects on pressure drop and heat transfer of misalignments in the holes through ceramic bricks used in hypersonic wind tunnel storage heaters.

The bricks and conditions considered correspond to the APTU (Airbreathing Propulsion Test Unit) facility to be installed at AEDC. These conditions are summarized in Table B-1 below.

TABLE B-1

WIND TUNNEL HEATER CONDITIONS CONSIDERED

Nominal pressure = 3000 psi
Nominal flow rate = 1150 lbm/sec
Initial bed temperature distribution is sinusoidal with T_{bottom} = 1520°R and T_{top} = 4500°R
Hole diameter (D) = 0.20 inches
Hole center distance to diameter ratio (S/D) = 1.47
Heater core height = 24 ft
Yttria Stabilized Zirconia bricks in top 12 ft of heater
Alumina bricks in bottom 12 ft of heater
All bricks assumed to be 6 inches long.

This brief study was motivated by the fact that certain Zirconia bricks received by AEDC for use in a pilot heater had hole misalignments significantly greater than anticipated. Quantitative details relative to the hole misalignments are available from Reference B-1. Three cases were considered here:

1. 0% misalignment (i.e., no misalignment; the baseline case)
2. 14% misalignment* (corresponds to an approximate average misalignment)
3. 30% misalignment* (corresponds approximately to worst case misalignment considering keying tolerance and hole misalignments)

*Percent misalignments are defined on an area basis; blocked area/area originally open to flow.

The effects of the hole misalignments on fluid friction and pressure drop are discussed in Section B.2. Estimates of the heater core pressures differentials for a constant flow rate, and of the flow rates through the bricks for a constant heater core pressure drop, are given. The effects of the hole misalignments on heat transfer from the heater core to the fluid being heated are discussed in Section B.3. A quantitative calculation of the brick temperature distribution histories was beyond the scope of this study, although certain limiting cases are considered. Conclusions are drawn and recommendations are made in Section B.4.

SECTION B.2

EFFECTS ON PRESSURE DROP AND FLOW RATE

The effects of the brick hole misalignments on the heater pressure drop and flow rates are considered in the following subsections.

B.2.1 GOVERNING EQUATIONS

The pressure drop through aligned brick holes may be easily calculated from a mass and momentum balance. For a constant mass flow rate and a variable density fluid the momentum equation expresses a balance between acceleration, pressure force, and wall shear. The wall shear for turbulent flow in pipes may be defined in terms of a friction factor and substituted into the momentum equation. Also, using continuity and the equation of state for an ideal gas, one can express the momentum equation in terms of temperature, mass flux and pressure as follows:

$$\frac{dP}{dx} + \frac{G^2Rf}{4r}\left(\frac{T}{P}\right) + G^2R\,\frac{d}{dx}\left(\frac{T}{P}\right) = 0 \qquad \text{(B-1)}$$

where

G = mass flux
f = friction factor
r = radius
R = gas constant

Equation (B-1) is the governing equation, valid for one dimensional steady turbulent flow and can be solved for dP/dx if the temperature distribution is given.

Equation (B-1) may be simplified if the temperature gradient is much greater than the pressure gradient. This is the case for the conditions of interest here; it can be shown that

$$\frac{d}{dx}\left(\frac{T}{P}\right) \sim \frac{1}{P}\frac{dT}{dx}$$

to within 1% error. Hence Equation (B-1) reduces to

$$\frac{dP}{dx} + \frac{G^2Rf}{4r}\left(\frac{T}{P}\right) + \frac{G^2R}{P}\frac{dT}{dx} = 0 \qquad \text{(B-2)}$$

Misalignment of holes at brick interfaces will cause the flow to separate. Ideally the pressure loss can be calculated from a mass and momentum balance.

However, for flows involving separation it is convenient to express the pressure loss in terms of a nondimensional head loss (K) where K is defined as

$$K = \frac{\Delta P/\rho}{1/2\ V^2} \tag{B-3}$$

For turbulent flows in which separation occurs K is to a good approximation dependent only upon boundary geometry or the amount of separation caused by a particular boundary geometry. Thus K can be estimated from existing literature values for systems with similar geometry.

Equation (B-3) is valid for steady incompressible flow. Since the region of separation for the mass fluxes encountered in this problem is sufficiently small compared to nominal brick length, one can assume that Equation (B-3) is valid at the brick interface. Solving for ΔP and using the ideal gas equation of state, Equation (B-3) can be expressed as follows:

$$\Delta P = \frac{K}{2}\,\frac{G^2TR}{P} \tag{B-4}$$

The determination of K will be considered in Section B.2.2.

Since Equation (B-4) is applicable only at discrete sections, at which T, P are dependent on upstream conditions, it is necessary to rewrite Equation (B-2) as

$$\Delta P = -\frac{G^2R}{P_{avg}}\left(\frac{f}{4r}\,T_{avg} + \frac{\Delta T}{\Delta x}\right)\Delta x \tag{B-5}$$

The total pressure drop across the heater bed may be calculated by progressing downstream through a hole applying Equation (B-5) along the length of a brick and Equation (B-4) at the brick interface.

B.2.2 ESTIMATION OF HEAD LOSS AT BRICK INTERFACE

As mentioned in Section B.2.1, K is a convenient correlation which can be used to determine the pressure drop due to misalignment. Figure B-1 shows the functional relationship between K and area ratio for a sudden expansion and sudden contraction (note that for $0.5 \leq A_1/A_2 \leq 1.0$, $K_{exp} \sim K_{cont}$). For misaligned holes the resistance to flow is greater than a sudden expansion and less than a sudden contraction. Hence if an equivalent area ratio can be determined at brick interfaces and provided this area ratio is between 0.5-1.0 a reasonable estimate can be made of K.

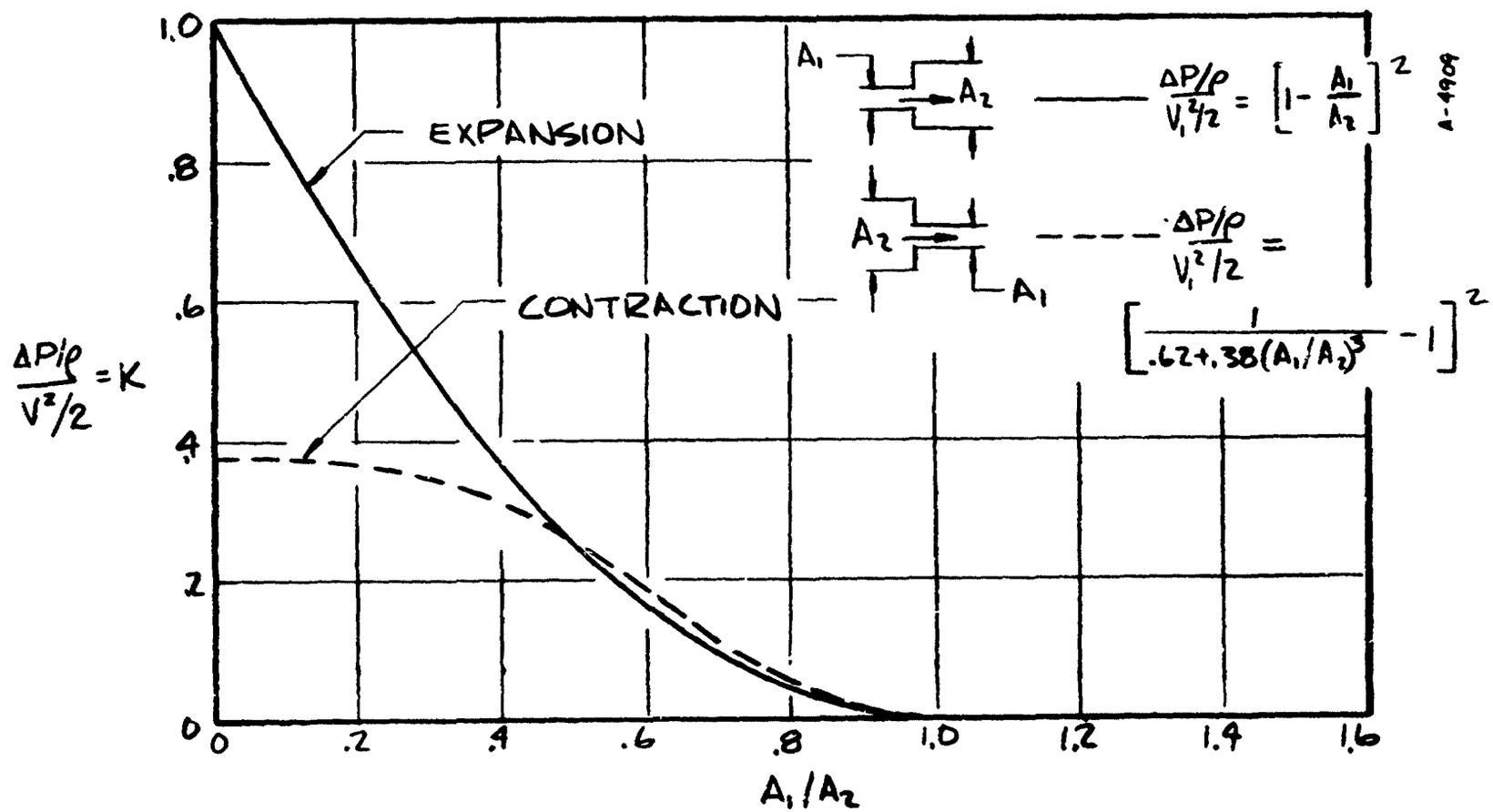

FIGURE B-1 DIMENSIONLESS HEAD LOSS (K) FOR TURBULENT FLOW THROUGH SUDDEN EXPANSIONS AND CONTRACTIONS

For turbulent flow K is a function only of system geometry, hence one can define the area ratio in terms of equivalent flow blockage for a sudden contraction or conversely in terms of equivalent flow expansion for a sudden expansion. As pointed out in the introduction the two cases of area misalignment of interest were 14% and 30%. Using the above formulation for area ratio one obtains K = .026 and K = .10 for 14% (A_1/A_2 = .86) and 30% (A_1/A_2 = .70) misalignment respectively. These values of the nondimensional head loss are the average of sudden expansion and sudden contraction at the given area ratio.

The head loss at the brick interfaces was also estimated by assuming that K is proportional to the volume of separation, and by applying a momentum balance while assuming all energy dissipation occurs in the region of expanding flow. These alternative approaches yielded values of K which were in essential agreement with the values given above.

B.2.3 CALCULATION OF BED PRESSURE DROP FOR 0%, 14%, and 30% HOLE MISALIGNMENT WITH CONSTANT FLOW RATE

Section B.2.1 briefly summarized the equations used to estimate the total bed pressure drop through the heater bricks. Using the values of K found in Section B.2.2 the total pressure drop can be computed by progressing through the heater bed using Equation (B-5) along a brick length and applying Equation (B-4) at a brick interface.

This calculation was carried out for a total heater flow rate of 1150 lbm/sec, surface roughness of 100 μ inches and for a temperature distribution corresponding to 10 seconds from the initial time. The results are shown in Tables B-2 and B-3 for 14% and 30% area offset. For zero percent misalignment, the pressure drop across the bed is 4.8 psi for these conditions. Hole misalignments of 14% and 30% increased the total pressure drop to 6.7 psi and 12.3 psi respectively. Note that at 30% misalignment the total pressure drop is still only 0.4% of the entrance pressure.

B.2.4 CALCULATION OF FLOW RATES FOR 0%, 14%, AND 30% HOLE MISALIGNMENTS WITH CONSTANT PRESSURE DROP

In Section B.2.3 the pressure drop across the heater was estimated assuming a constant heater flow rate (1150 lbm/sec) for hole misalignments of 0%, 14%, and 30%. In reality, the misalignment of the holes is not uniform and varies from near 0% at the brick center to higher values closer to the edge of the brick. Since the pressure drop across the bed must be the same for all holes, misaligned holes will have lower flow rates than aligned holes. This variation in flow rates is estimated in this section.

AXIAL LOCATION	FRICT+THERM PRESS DROP	OFF PRESS DROP	TOTAL PRESSURE
.50	.03812	.00771	2999.95419
1.00	.04355	.01018	2999.90048
1.50	.04738	.01193	2999.84122
2.00	.05090	.01353	2999.77682
2.50	.05473	.01527	2999.70685
3.00	.05856	.01702	2999.63129
3.50	.06272	.01891	2999.54968
4.00	.06591	.02036	2999.46344
4.50	.06943	.02196	2999.37207
5.00	.07295	.02357	2999.27557
5.50	.07646	.02517	2999.17398
6.00	.08142	.02742	2999.06519
6.50	.08493	.02902	2998.95123
7.00	.07475	.02924	2998.84726
7.50	.07827	.03084	2998.73819
8.00	.08146	.03230	2998.62445
8.50	.08466	.03376	2998.50604
9.00	.08722	.03492	2998.38391
9.50	.09042	.03638	2998.25714
10.00	.09362	.03783	2998.12573
10.50	.09618	.03900	2997.99060
11.00	.09664	.04017	2997.85382
11.50	.09984	.04162	2997.71240
12.00	.10208	.04264	2997.56769
12.50	.10433	.04367	2997.41974
13.00	.10689	.04483	2997.26804
13.50	.10913	.04585	2997.11310
14.00	.11137	.04687	2996.95490
14.50	.11362	.04790	2996.79340
15.00	.11586	.04892	2996.62866
15.50	.11779	.04979	2996.46112
16.00	.12035	.05096	2996.28986
16.50	.12196	.05169	2996.11624
17.00	.12420	.05272	2995.93936
17.50	.12645	.05374	2995.75922
18.00	.12596	.05461	2995.57867
18.50	.12789	.05549	2995.39632
19.00	.12982	.05637	2995.20917
19.50	.13174	.05725	2995.02023
20.00	.13335	.05798	2994.82895
20.50	.13560	.05900	2994.63437
21.00	.13510	.05944	2994.43986
21.50	.13639	.06003	2994.24347
22.00	.13768	.06062	2994.04520
22.50	.13897	.06120	2993.84506
23.00	.14058	.06194	2993.64258
23.50	.14155	6238	2993.43869
24.00	.14220	.06000	2993.29651

TOTAL FRICTION= 4.8210 PSI TOTAL OFFSET= 1.8840 PSI

TABLE B-2

AXIAL PRESSURE DROP ACROSS HEATER BED, 14% MISALIGNMENT

AXIAL LOCATION	FRICT+THERM PRESS DROP	OFF PRESS DROP	TOTAL PRESSURE
.50	.03812	.03083	2999.93106
1.00	.04355	.04072	2999.84680
1.50	.04738	.04770	2999.75174
2.00	.05090	.05411	2999.64679
2.50	.05473	.06109	2999.53101
3.00	.05857	.06807	2999.40439
3.50	.06272	.07564	2999.26605
4.00	.06592	.08146	2999.11868
4.50	.06944	.08787	2998.96140
5.00	.07296	.09427	2998.79419
5.50	.07647	.10068	2998.61707
6.00	.08143	.10971	2998.42596
6.50	.08495	.11612	2998.22495
7.00	.07477	.11700	2998.03323
7.50	.07829	.12341	2997.83157
8.00	.08149	.12924	2997.62088
8.50	.08469	.13507	2997.40115
9.00	.08725	.13974	2997.17419
9.50	.09046	.14557	2996.93817
10.00	.09366	.15141	2996.69312
10.50	.09623	.15608	2996.44083
11.00	.09869	.16075	2996.18341
11.50	.09990	.16659	2995.91696
12.00	.10214	.17068	2995.64417
12.50	.10439	.17477	2995.36505
13.00	.10596	.17945	2995.07667
13.50	.10921	.18355	2994.78595
14.00	.11146	.18764	2994.48688
14.50	.11371	.19174	2994.18143
15.00	.11596	.19586	2993.86966
15.50	.11790	.19936	2993.55243
16.00	.12047	.20405	2993.22794
16.50	.12208	.20698	2992.89690
17.00	.12434	.21109	2992.56351
17.50	.12659	.21519	2992.22174
18.00	.12611	.21872	2991.87695
18.50	.12805	.22224	2991.52670
19.00	.12998	.22577	2991.17099
19.50	.13192	.22930	2990.80981
20.00	.13354	.23224	2990.44406
20.50	.13580	.23635	2990.07196
21.00	.13531	.23614	2989.69855
21.50	.13661	.24050	2989.32147
22.00	.13790	.24287	2988.94073
22.50	.13920	.24523	2988.55634
23.00	.14063	.24818	2988.16736
23.50	.14181	.24997	2987.77563
24.00	.14247	.00000	2987.63318

TOTAL FRICTION= 4.8253 PSI TOTAL OFFSET= 7.5430 PSI

TABLE B-3

AXIAL PRESSURE DROP ACROSS HEATER BED, 30% MISALIGNMENT

To obtain a simple relation for calculating the mass flow rate per hole at a given pressure drop and degree of misalignment, it was assumed that the total pressure drop could be expressed in the functional form of Equation (B-4) This amounts to defining an effective net head loss for 0%, 14%, and 30% misalignment. Using Equation (B-3) the following ratio may be formed:

$$\dot{m}_{0\%,\ 14\%,\ 30\%} = (.0144)\sqrt{\frac{\Delta P_{across\ bed}}{\Delta P_{0\%,\ 14\%,\ 30\%}}} \qquad \text{(B-6)}$$

where $\dot{m}$ is the mass flow per hole and has units of lbm/sec. The ΔP's refer to those calculated in Section B.2.3 for total mass flow rate of 1150 lbm/sec.

From Equation (B-6), the following mass flows rates per hole were computed:

- $\Delta P_{across\ bed} = 4.8$ psi

  $\dot{m}$ (0%) = .0144 lbm/sec-hole

  $\dot{m}$ (14%) = .0122 lbm/sec-hole

  $\dot{m}$ (30%) = .0086 lbm/sec-hole

- $\Delta P_{across\ bed} = 6.7$ psi

  $\dot{m}$ (0%) = .0170 lbm/sec-hole

  $\dot{m}$ (14%) = .0144 lbm/sec-hole

  $\dot{m}$ (30% = .0104 lbm/sec-hole

- $\Delta P_{across\ bed} = 12.8$ psi

  $\dot{m}$ (0%) = .0231 lbm/sec-hole

  $\dot{m}$ (14%) = .0199 lbm/sec-hole

  $\dot{m}$ (30%) = .0144 lbm/sec-hole

The above calculated mass flow rates will be used in Section B.3.2 in estimating the magnitude of the temperature gradient between holes.

SECTION B.3

EFFECTS ON HEAT TRANSFER

One of the primary reasons for accessing the thermal response of the heater core bricks is to predict the severity of brick thermal stresses. Hole misalignments in heater core bricks could augment thermal stresses via two mechanisms:

1. hole misalignment causes the flow to separate and reattach resulting in a substantial axial variation in the local heat transfer rates; and
2. hole misalignment increases the flow resistance, reducing the mass flow rate and hence the heat transfer such that significant radial temperature gradients might exist across bricks having variable hole misalignments.

The objective of this section is to evaluate the importance of the above mechanisms. Section B.3.1 discusses the effects of separation and Section B.3.2 will deal with temperature gradients between holes. The heat transfer physics associated with the above mechanisms are of sufficient complexity that only approximate estimates are made.

B.3.1 HEAT TRANSFER IN SEPARATED FLOWS

Separated flows cause a substantial axial variation in the local transfer coefficient, h_x, and hence in the local heating rates. Large axial variations in heating rates could cause material failure due to thermal stressing. The fluid mechanics of separated flows are highly complex and reasonable analytical methods for predicting the flow field do not exist. Therefore it is not possible to analytically predict h_x, and one must rely on heat transfer data.

Typically in separated flows the axial variation of h_x follows a bell shaped curve. That is at the point of separation h_x is at a minimum below that which exists at fully developed conditions and rises as one proceeds downstream toward the reattachment point. At the point of reattachment h_x reaches a maximum and then decays to a value consistent with fully developed flow.

The data of Zemanick and Dougall (Reference B-2) on the heat transfer rates downstream of an abrupt circular channel expansion represents the best data available as far as being geometrically similar to the problem of misaligned holes. From their data the ratio of the maximum local heat transfer coefficient to the local fully developed heat transfer coefficient can be estimated.

- 14% Area Blockage, $h_{max}/h_{fd} = 2.0$
- 30% Area Blockage, $h_{max}/h_{fd} = 3.2$

The maximum h_x occurs at the point of reattachment, which is dependent on system geometry. Zemanick and Dougall data indicate that for $A_1/A_2 = .70$ the point of reattachment is approximately 0.1 inches downstream of the sudden expansion. Hence h_x changes by a factor of 3 in 0.1 inches. This large variation could give rise to very high localized temperature gradients and thermal stresses.

Separation also has the effect of increasing the overall average heat transfer coefficient. While this overall increase in h is not calculated here, three approaches could be taken to estimate this increase:

- Integrating h_x over the length of heater bed, where h_x could be estimated from the data of Zemanick and Dougall.
- Estimating an equivalent friction factor due to misalignment (analysis similar to Section B.2 4) and using correlations which have been developed for heat transfer on roughened surfaces (see for example, Reference B-3).
- Utilizing a simple bench-scale apparatus (e.g., misaligned copper tubes fitted with thermocouples) to measure h experimentally

B.3.2 EFFECTS OF HOLE MISALIGNMENTS ON HEAT TRANSFER

As pointed out in Section B.2.4, a decrease in the mass flow rate due to misalignment could cause a substantial radial temperature gradient between holes having different mass flows. This problem is difficult to handle analytically due to the heat transfer coupling between holes. If one assumes that the holes are independent, i.e., no cross conduction, and that misalignment does not increase the overall heat transfer coefficient, then an upper bound on the temperature gradient between holes can be computed.

The TACH code (described in the main text) was utilized to predict the thermal response of holes with different mass flow rates due to misalignments.

In Section B.2.4 mass flow rates were calculated for 0%, 14%, and 30% hole misalignments at a given pressure drop across heater bed. These values of mass flow rates were then used in the thermal response code. Figures B-2 and B-3 illustrate the effect of different mass flow rates on the heater thermal response, subject to the assumptions discussed. As can be seen from these figures, the temperature difference initially increase with time.

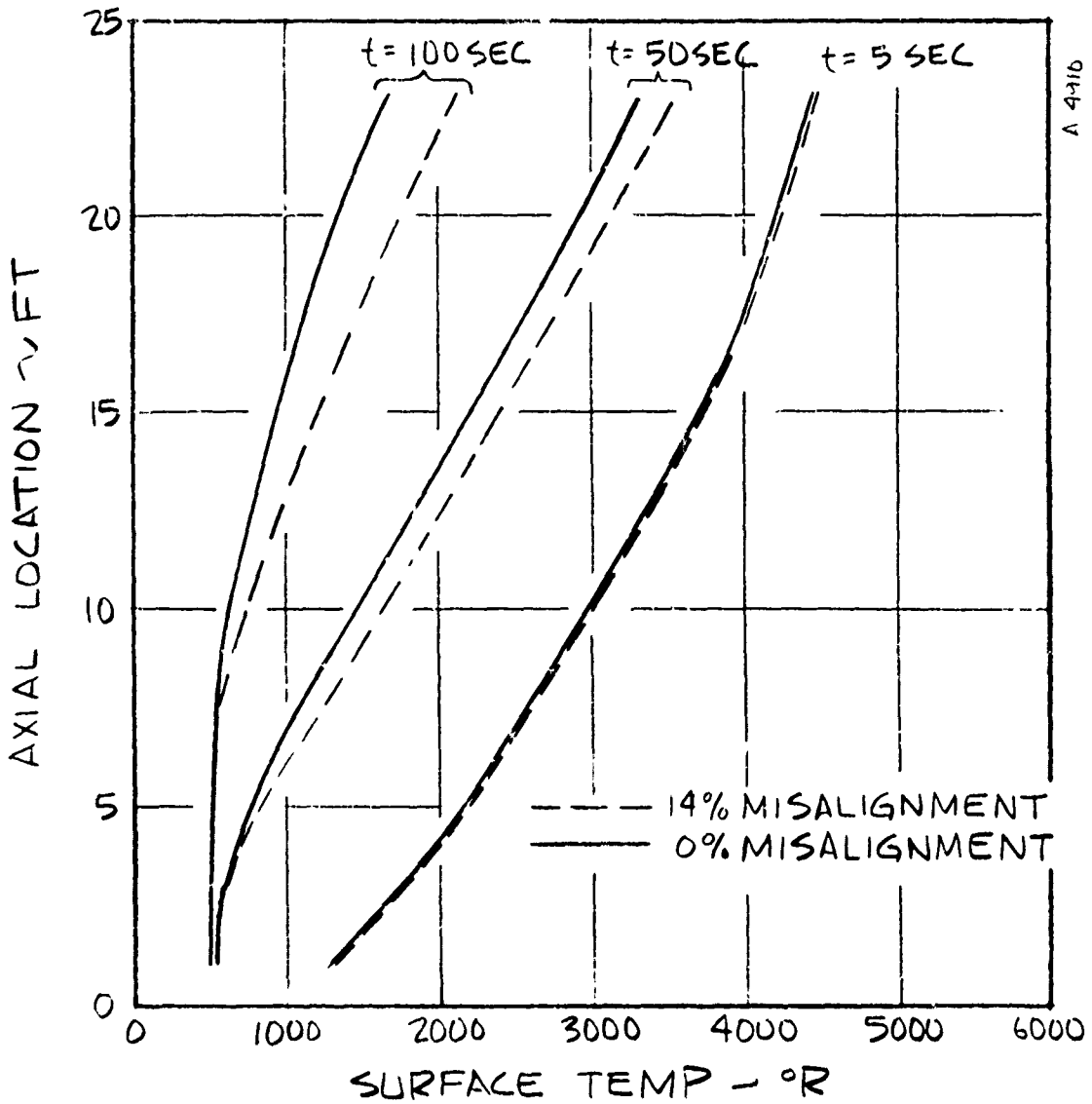

FIGURE B-2 COMPARISON OF BED THERMAL RESPONSE FOR 0% ($\dot{M}$ = .0144 LBM/SEC-HOLE) & 14% ($\dot{M}$ = .0122 LBM/SEC-HOLE) MISALIGNMENT — NEGLECTING CROSS-CONDUCTION

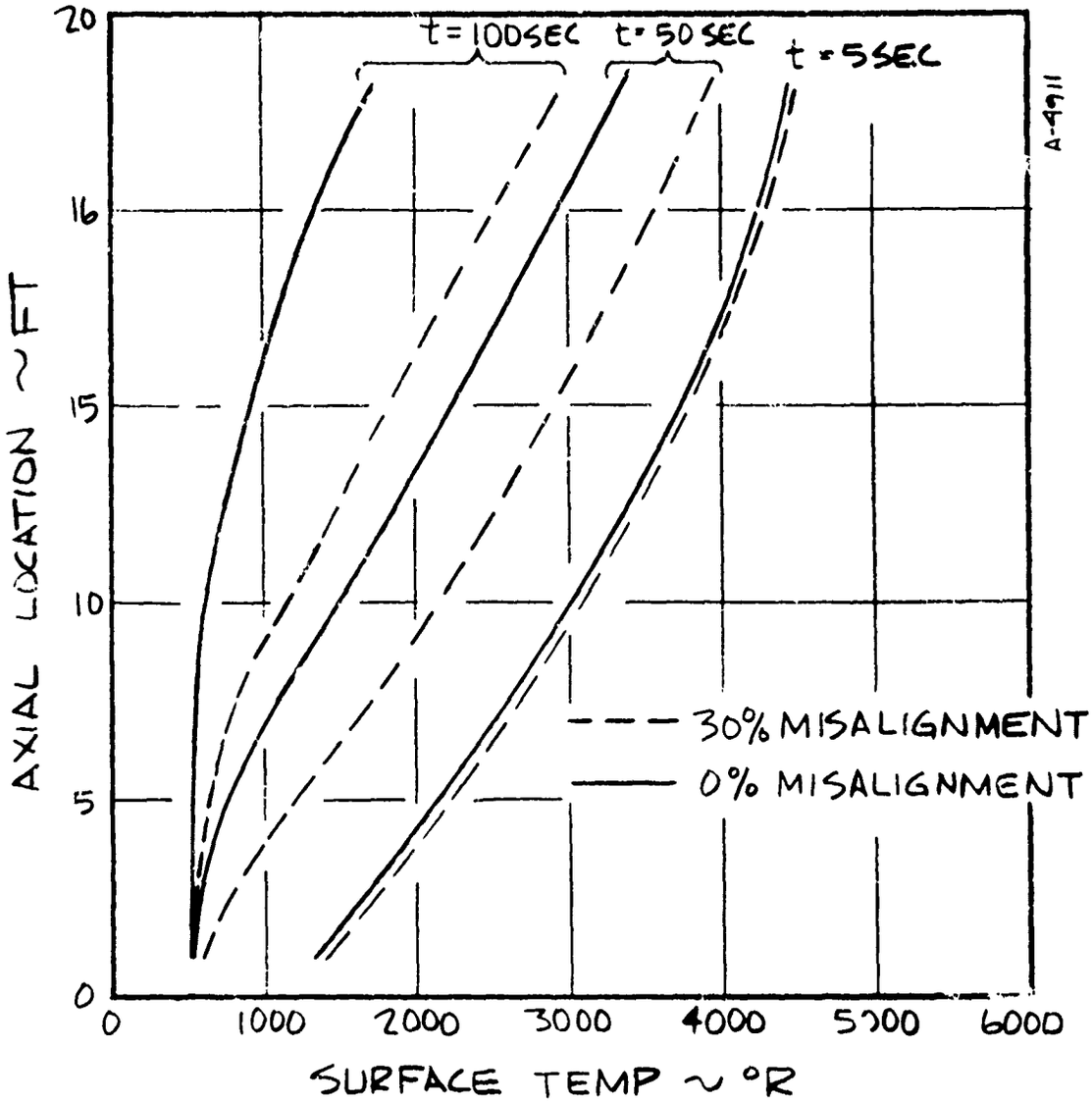

FIGURE 8-3 COMPARISON OF BED THERMAL RESPONSE FOR 0% ($\dot{M}$ = .0144 LBM/SEC-HOLE) & 30% ($\dot{M}$ = .0086 LBM/SEC-HOLE) MISALIGNMENT — NEGLECTING CROSS-CONDUCTION

The maximum temperature difference encountered at shut down time is of primary importance. Since the overall heat transfer coefficient for turbulent flow in pipes is proportional to the Reynolds number raised to the .' power, the largest temperature differences will occur at the lower mass flow rates or at the lowest pressure drop across heater bed. Figure B-4 illustrates the exit temperature difference for $\Delta P = 4.8$ psi. As can be seen, two cases are considered: ΔT based on 0% and 14% misalignment and ΔT based on 0% and 30% misalignment. Shut-down time was determined when the exit temperature for 0% misalignment dropped by 10%. For convenience the maximum temperature differences at shut down time are summarized below:

- ΔT (14% misalignment - 0% misalignment) = 60°R
- ΔT (30% misalignment - 0% misalignment) = 290°R

Using the above values for the maximum temperature differences at shut down, one can make a simple calculation to determine the magnitude of conduction across the holes. It is found from this calculation that conduction across holes is the same order of magnitude as convection across brick-air interface. Therefore it can be concluded that the estimated maximum temperature differences are overestimates, i.e., such a large temperature difference would not occur since the conduction heat transfer coupling would tend to dissipate this temperature difference. An analytical computation of this multiply coupled heat transfer problem would be relatively complex and was beyond the scope of the preliminary study.

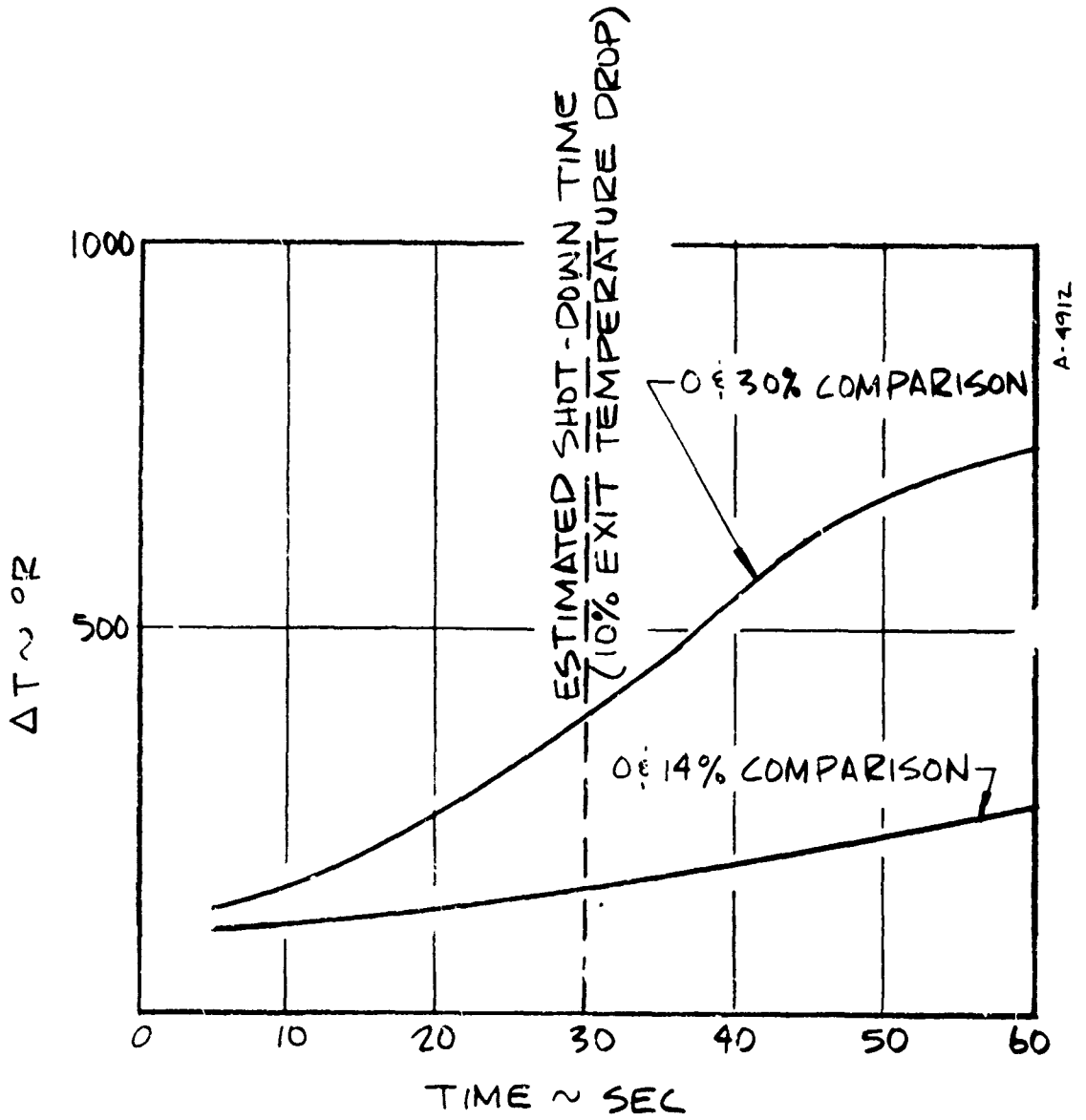

FIGURE B-4 ESTIMATED MAXIMUM TEMPERATURE DIFFERENCE BETWEEN 0 & 14% MISALIGNMENT AND 0 & 30% MISALIGNMENT FOR HEATER ΔP = 4.8 PSI — NEGLECTING CROSS-CONDUCTION

SECTION B.4

SUMMARY AND CONCLUSIONS

Pressure Drop and Flow Rate

- For an average misalignment of 14% the pressure drop across the heater bed will increase from 4.8 psi to about 6.7 psi.
- Pressure drop will be less than 1% of entrance pressure (3000 psi) for all cases of misalignment.
- For heater bed pressure drops of 4.8 psi, 14% and 30% misalignments will reduce the mass flow rates per hole by 15% and 38% respectively.

Heat Transfer

- Due to flow separation and reattachment, the local heat transfer coefficient (h_x) will vary by a factor of about 2 or 3 within 0.1 inches of the brick interfaces for misaligned holes.
- The influence of this variation in h_x on thermal stresses should be estimated analytically. If the thermal stress calculation shows that a variation in h_x is critical, the h_x variation could be defined experimentally using a simple bench scale apparatus.
- Heat transfer analyses indicated that an upper limit of the temperature gradient across a brick with variable hole misalignments is about 60°R for 0 to 14% misalignment and 300°R for 0 to 30% misalignment. These calculations neglected cross-conduction and heat transfer coefficient increase for misaligned holes. In view of these conservative assumptions, it is estimated that the actual temperature gradients across the bricks will be less than half this large.

REFERENCES

B-1. Fahrenbacher, Maj. L., personal communication, Air Force Aerospace Research Laboratory, Wright Patterson Air Force Base, Ohio, May 1972.

B-2. Zemanick, P. P., and Dougall, R. S., "Local Heat Transfer Downstream of Abrupt Circular Channel Expansion," Journal of Heat Transfer, Trans. ASME, Series C, Vol. 92, No. 1, February 1970, pp. 53-60.

B-3. Norris, R. H., "Some Simple Approximate Heat Transfer Correlations for Turbulent Flow in Ducts with Rough Surfaces," in "Augmentation of Convective Heat and Mass Transfer," Ed. by Bergles, A. E., and Webb, R. L., presented at ASME Winter Meeting, December 1970.

APPENDIX C

LIMITATIONS DUE TO COMBINED STRESS EFFECTS AND FRACTURE CRITERIA UNCERTAINTIES

by

F. C. Weiler

Preceding page blank

The equivalent cylinder model used to evaluate the hypothetical nonlinear temperature gradients within the bricks was only an approximation to the real brick's geometry. Since the real nonlinear gradients were not known explicitly, this 2-dimensional model was used for economic reasons. However, as shown by the in-plane analyses, the hexagonal geometry does produce stresses which deviate from equivalent cylinder geometries as demonstrated by the shear stress τ_{xy} (cf. text Figures 13e and 14d). In a cylindrical geometry, these shear stresses would be zero. Consequently, a more accurate 3-dimensional model of the hexagonal brick, like the one shown in Figure C-1 would yield more accurate results for the nonlinear temperature gradient loading cases. Since the stresses from this source of loading proved significant in contributing towards the total stresses which could produce fracture, a more accurate determination of the stress state within a hexagonal brick 3-dimensional model would be useful. However, the cost of running any 3-dimensional model is high and this analysis should not be undertaken without knowing explicitly the degree of nonlinear temperature gradients which could exist within the bricks. Once an accurate determination of these nonlinear gradients is made, then a 3-dimensional stress analysis utilizing a model similar to the one shown in Figure C-1 would yield results which are more accurate. These results could then be used in conjunction with the in-plane analyses (which are quite accurate) to produce a better interaction curve like the one shown in Figure 22. Since the interaction curve shown in Figure 22 was based upon the 2-dimensional equivalent cylinder model, it should only be used in a qualitative manner.

Another reason for only using this curve in a qualitative manner is that the fracture criterion used did not take into account the shear stresses which were present within the bricks. When examining the in-plane solutions, one notices that fairly significant shear stresses can develop (cf. text Figures 13e and 14d). In fact, these shear stresses were approximately 40 percent of the maximum tensile stresses within the brick. When postulating a fracture criterion for yttria stabilized zirconia, one immediately notices that the deformational behavior of YSZ and other ceramics falls into the class of materials which are elastic-brittle, similar to concrete and rocks. The literature abounds with different failure criteria for this class of materials but most of it centers around the well known Coulomb-Mohr failure criterion in one form or another. A typical failure surface of this type is shown in Figure C-2, where Mohr's theory, represented by the solid dark line, and Coulomb's theory, represented by the dashed line, are both illustrated. The Mohr theory assumes that the limiting shear stress is $\tau = f(\sigma)$, i.e., some function of the normal stress acting upon a small element of material. One such possible functional relationship would be

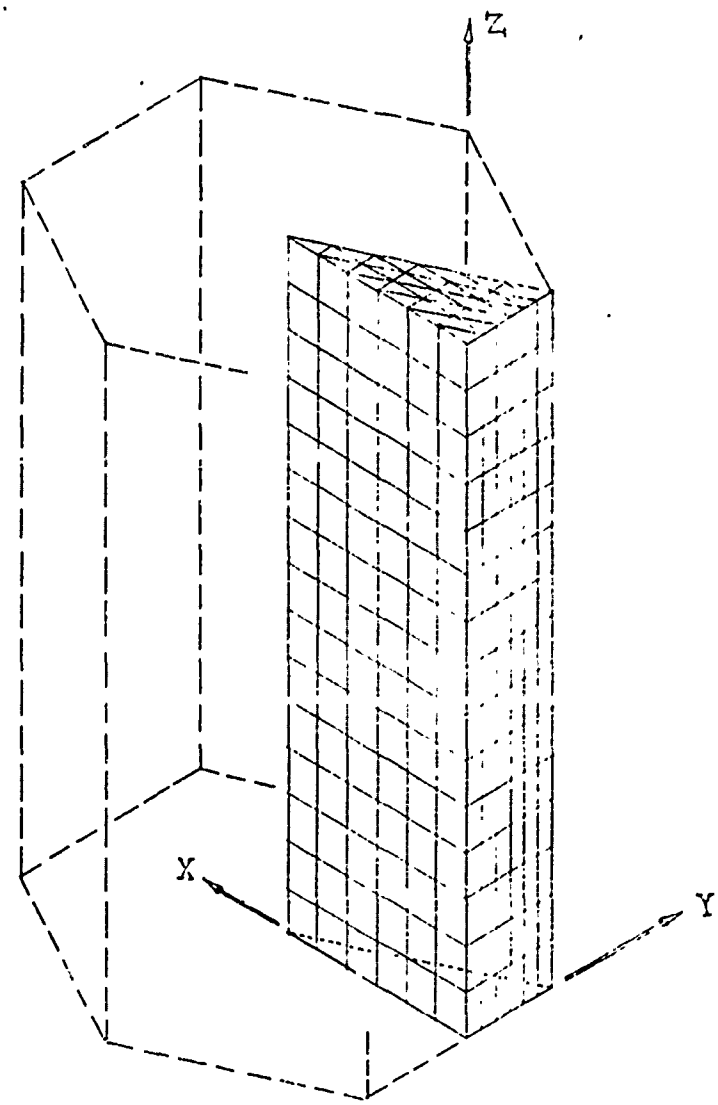

FIGURE C-1 3-DIMENSIONAL FINITE ELEMENT MODEL OF HEXAGONAL BRICK

A-5284

$$\tau^2 = 4\sigma_t(\sigma_t - \sigma_n)$$

where σ_t = uniaxial tensile strength, σ_n = normal compressive stress and τ = shear rupture stress.

In contrast, a typical Coulomb criterion would be

$$\tau = \tau_o + \mu\ \sigma_n$$

where τ_o = intrinsic shear resistance of the material and μ = coefficient of internal friction, and τ and σ_n are the same as above.

Without going into more detail (cf. Reference C-1 for further details), one can notice that the failure of elastic-brittle materials can depend upon more than just the uniaxial tensile strength of the material. In fact, even under compressive loading conditions, when high shear stresses are present, failure will occur as shown by the Coulomb-Mohr failure envelopes in Figure C-2. Such a condition exists as shown for the point contact loading analysis as shown in text Figures 20c and 20e. Although these stresses were not severe enough to cause failure, the type of stresses present were compresive normal stresses accompanied by shear stresses.

The main point to be made here is the following. In the normal stress "tensile" region (cf. Figure C-2), when shear stresses are present, the magnitude of the tensile stresses needed to cause fracture are less than the uniaxial tensile strength of the material. When the shear stresses are zero, then the tensile stresses must reach the uniaxial tensile strength in order to cause fracture. Since the shear stresses were neglected in the combined stress analysis, the interaction curve shown in text Figure 22 represents an unconservative estimate of conditions necessary to cause fracture, i.e., fracture could occur for values of combined stresses less than that indicated by this interaction curve. Therefore, as stated before this interaction curve should only be used in a qualitative manner, and not as a design curve.

Reference

C-1. Jaeger, J. C., "The Brittle Fracture of Rocks," 8th Symposium of Rock Mechanics, Minnesota, 1966 (Proceedings to be published by AIME).

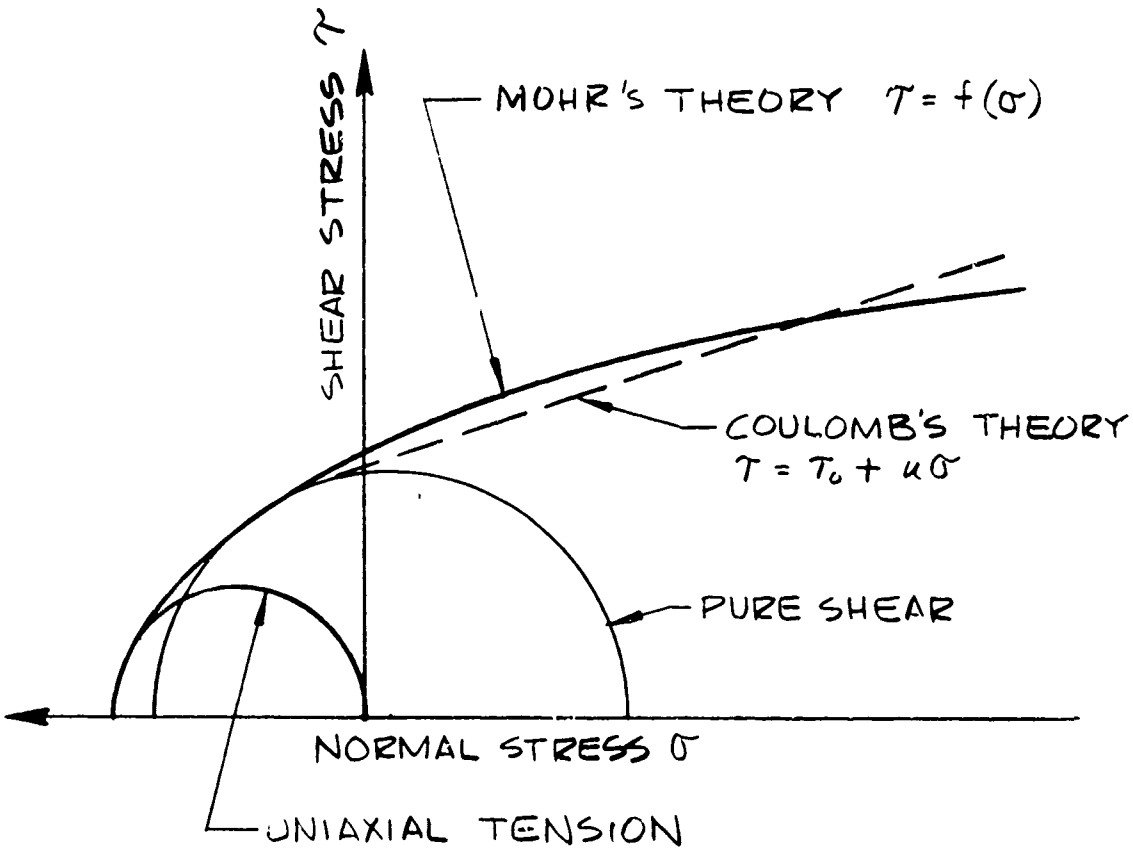

FIGURE C-2 COULOMB-MOHR FAILURE CRITERION FOR ELASTIC-BRITTLE MATERIALS

A-5285